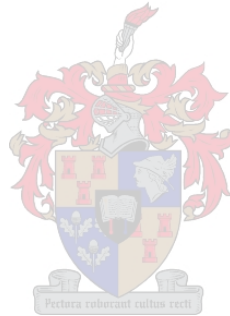


# Position Sensorless and Optimal Torque Control of Reluctance and Permanent Magnet Synchronous Machines

HUGO WERNER DE KOCK



*Dissertation approved for the degree  
Doctor of Philosophy in Electrical Engineering  
at the Stellenbosch University*

PROMOTER: Prof. M.J. Kamper, Stellenbosch University, South Africa  
CO-PROMOTER: Prof. R.M. Kennel, Wuppertal University, Germany  
(from 01.10.2008 at the Technische Universität München, Germany)

March 2009

## Declaration

*By submitting this thesis electronically, I declare that the entirety of the work contained therein is my own, original work, that I am the owner of the copyright thereof (unless to the extent explicitly otherwise stated) and that I have not previously in its entirety or in part submitted it for obtaining any qualification.*

DATE: 15 FEBRUARY 2009

# Abstract

**Keywords:** position sensorless control, torque control, synchronous machines

The work in this thesis deals with energy efficient torque control and rotor position estimation in the full speed range, for a family of synchronous machines that should be used more often in the near future. This family consists of the permanent magnet synchronous machine (PMSM), the reluctance synchronous machine (RSM), the interior-PMSM and the PM-assisted-RSM.

By designing and controlling these synchronous machines correctly, better performance and higher energy efficiency can be expected compared to the performance and efficiency of an industry standard induction machine. However, applications are limited to variable speed drives (VSD) in a certain power range, e.g. below 100kW. With the growing concern and necessity of a better utilization of energy, it is becoming standard to use electronically controlled power converters between the electricity grid and electrical machines. Therefore, there is a very large scope for the implementation of this synchronous machine technology.

For traction applications like electrical vehicles, the optimally controlled synchronous machine technology has a very strong position. Very compact and robust synchronous machines with a very high power density can be designed that may out-perform the induction machine by far. However, one major requirement for most applications is position sensorless control, i.e. rotor position estimation in the whole speed range.

To achieve energy efficient torque control, maximum torque per Ampere (MTPA) control should be implemented. It is possible to achieve MTPA control at low speed, but above the rated speed of the machine, field weakening needs to be performed. The question is how to implement MTPA and effective field weakening for any value of speed and DC bus voltage and for any machine within this family of synchronous machines. In this thesis a method is explained to achieve this goal using results from finite element (FE) analysis directly. The scheme may be implemented within a very short period of time.

The contribution of this thesis is a general understanding of the problems at hand, with an in-depth view into the mathematical representation of synchronous machines, a generic method of energy efficient torque control and a thorough study of rotor position and speed estimation methods.

# Opsomming

**Sleutelwoorde:** posisie sensorlose beheer, draaimoment beheer, sinchroonmasjiene

Hierdie studie handel oor energie-effektiewe draaimoment beheer en rotorposisie afskating in 'n wye spoedbereik vir 'n familie van sinchroonmasjiene (die permanente-magneet-sinchroonmasjien (PMSM), die reluktansie-sinchroonmasjien (RSM), die interne-PMSM en die PM-ondersteunde-RSM). Hierdie elektriese masjiene sal na alle waarskynlikheid in die nabye toekoms meer en meer vir 'n wye reeks van toepassings gebruik word.

Deur hierdie sinchroonmasjiene reg te ontwerp en te beheer, kan beter werkverrigting en 'n hoër benuttingsgraad verwag word, in vergelyking met die werkverrigting en benuttingsgraad van 'n standaard induksie(asinchroon)-masjien. Dit is egter slegs geldig vir aanpasbare spoed aandryfstelsels en binne 'n sekere drywingsvlak, bv. onder 100 kW. As gevolg van die groeiende druk en noodwendigheid om energie meer effektief te benut, is dit deesdae 'n standaard prosedure om elektronies-beheerde drywing-omsetters tussen die kragnetwerk en die elektriese masjiene te plaas. Dus word daar 'n groot mark geskep om hierdie sinchroonmasjien-tegnologie aan te wend.

In trekkrag aanwendinge soos elektriese voertuie, het die optimaal-beheerde sinchroonmasjien tegnologie reeds 'n vaste staanplek. Baie kompakte en robuste sinchroonmasjiene met baie hoë drywingsdigthede kan ontwerp word, wat 'n baie beter werkverrigting as die induksiemasjien het. Een groot vereiste is egter, dat posisie sensorlose beheer toegepas moet word, i.e. die rotor posisie moet in die hele spoed bereik afgeskat kan word.

Om energie-effektiewe draaimoment-beheer toe te pas moet maksimum-draaimoment-per-ampere (MDPA) beheer geïmplementeer word. Dit is moontlik om MDPA by lae spoed toe te pas, maar bo die basis-spoed moet veldverswakking toegepas word. Die vraag is hoe mens MDPA en effektiewe veldverswakking vir enige waarde van spoed en GS-bus spanning en vir enige lid in hierdie sinchroonmasjien-familie kan implementeer. In hierdie tesis word 'n metode voorgestel om hierdie doel te bereik. Die metode gebruik die resultate van 'n eindige elemente program direk en kan binne 'n kort periode geïmplementeer word.

Die bydrae van hierdie tesis is 'n omvattende begrip van die probleme voorhande, met 'n diep insig in die wiskundige voorstelling van sinchroonmasjiene, 'n generiese metode om energie-effektiewe draaimoment beheer toe te pas en 'n deeglike studie van rotor-posisie en -spoed afskating metodes.

# Zusammenfassung

**Schlüsselwörter:** geberlose Regelung, Drehmomentsteuerung, Synchronmaschinen

In dieser Arbeit geht es um die energieeffiziente Drehmomentsteuerung und Läuferpositionsschätzung für den gesamten Drehzahlbereich für eine Familie von Synchronmaschinen, die in naher Zukunft mehr und mehr eingesetzt wird. Diese Familie besteht aus der mittels Permanentmagneten (PM) erregten Synchronmaschine (PMSM), der Reluktanz-Synchronmaschine (RSM), der intern PMSM und der durch PM unterstützten RSM.

Durch einen geeigneten Entwurf und eine entsprechende Regelung dieser Synchronmaschinen, ist eine bessere Performance und höhere Effizienz im Vergleich zu einer Industriestandard Asynchronmaschine möglich. Dies gilt aber nur für drehzahlvariable Antriebe kleiner Leistung ( $< 100$  kW). Mit der heutzutage steigenden Notwendigkeit Energie besser zu nutzen, werden immer mehr elektronisch geregelte Leistungswandler zwischen dem Versorgungsnetz und der elektrischen Maschine eingesetzt. Daher wird es in Zukunft einen großen Markt für die oben erwähnten Synchronmaschinen geben.

Für Anwendungen in der Traktion (z.B. Elektroauto) haben optimal geregelte Synchronmaschinen einen hohen Stellenwert. In diesem Zusammenhang können sehr kompakte und robuste Synchronmaschine mit einer hohen Leistungsdichte entworfen werden, die vergleichbare Asynchronmaschinen leistungsmäßig übertreffen. Eine wichtige Anforderung ist jedoch der Einsatz einer geberlosen Regelung für diesen Maschinentyp. Das bedeutet, dass die Läuferposition über den gesamten Drehzahlbereich hinreichend genau abgeschätzt werden muss. Um eine energieeffiziente Drehmomentsteuerung zu erreichen, muss das Verfahren "Maximales Drehmoment pro Ampere" (MDPA) eingesetzt werden. Dies ist jedoch nur im Nenndrehzahlbereich möglich. Für Drehzahlen über dem Nennbetrieb muss der Feldschwächbetrieb verwendet werden. Daher stellt sich die Frage, wie eine MDPA Regelung und der Feldschwächbetrieb für beliebige Drehzahlen, Zwischenkreisspannungen und vor allem für jeden Typ der erwähnten Synchronmaschinen-Familie zu implementieren ist. Um dieses Ziel zu erreichen wird in dieser Dissertation eine Methode vorgeschlagen, in der direkt Resultate aus einem Finite Elemente Programme verwendet werden. Diese Methode hat den Vorteil, dass sie sehr schnell zu implementieren ist.

In dieser Dissertation wird ein allgemeines Verständnis für die vorhandene Problematik gegeben, wobei ein tiefer Einblick in die mathematische Beschreibung der Synchronmaschinen, eine allgemeine Methode für eine energieeffiziente Drehmomentsteuerung und eine ausführliche Untersuchung der geberlosen Regelung die einzelnen Teilaspekte bilden.

# Acknowledgements

The following people have made it possible for me to complete this work within a three year period of time. Thank you very much!

At the University of Stellenbosch in South Africa I would like to thank

- Prof. Maarten Kamper, my promoter, for his inspiring guidance.
- Mr. Arnold Rix who worked with me on the torque control algorithm.
- Dr. Roger Wang for his academic support.
- The International Office for financial support.
- The Bursary Office for financial support.
- The Division of Research Development for financial support.

At the University of Wuppertal in Germany I would like to thank

- Prof. Ralph Kennel, my co-promoter, for his support in many ways.
- Mrs. Ulrike Stock who organised so many things for me.
- Mrs. Andrea Bieck at the International Office for all her support.
- Dr. Oscar Ferreira and Mr. Dirk Paulus who worked with me on sensorless control.
- Dr. Pawel Sczupack for his help with the rapid prototyping system.
- Mr. Moog and Mr. Rostalski for their help with the practical aspects in the laboratory.
- Mr. Selleschy for his technical assistance.
- Dr. Nikolaus Oikonomo, Mr. Till Boller and Mr. Günter Schmitt for all their support.
- Dr. Rahul Kanchan and his wife Ashwini for their support and friendship.

I would like to thank

- Mr. Wolfgang Hammel at the company SEW Eurodrive in Germany,
- Mr. Stefan Zeh at the company Diehl-Ako in Germany and
- Prof. Tian-Hua Liu at the National Taiwan University of Science and Technology

for their support and inputs regarding position sensorless control.

I would like to thank the DAAD (German Academic Exchange Service) for the one year scholarship and four months German language course that they offered me. Also for the equipment that they have sponsored that was sent to the University of Stellenbosch to make further research possible.

I would also like to thank Kobus Meiring, Gerhard Swart and Jian Swiegers from the company Optimal Energy in South Africa for the interesting meetings we had regarding the electrical drive system for an electrical car.

Of course I would also like to thank God, my family and all my other friends for providing the much needed love and support.

# List of Publications

My research on electrical machine control started in 2005 when I did a Master's degree at the University of Stellenbosch in South Africa. Early 2006 the Master's thesis and a paper at a local conference (SAUPEC in Durban, South Africa) was published.

- H. de Kock, "Dynamic Control of the Permanent Magnet assisted Reluctance Synchronous Machine with Constant Current Angle," Master's thesis, University of Stellenbosch, 2006.
- H. de Kock and M. Kamper, "Energy Efficient Current Control of the Permanent Magnet assisted Reluctance Synchronous Machine," in Southern African Universities Power Engineering Conference (SAUPEC), 2006.

I started with the PhD degree in 2006. A paper about the work that I did for my Master's degree was published in an international journal early in 2007.

- H. de Kock and M. Kamper, "Dynamic Control of the Permanent Magnet-assisted Reluctance Synchronous Machine," *Electric Power Applications, IET*, vol. 1, no. 2, pp. 153-160, 2007.

In June 2006 I moved to the University of Wuppertal in Germany and started research on sensorless control. I moved back to Stellenbosch for six months in 2007 and then back to Wuppertal from June 2007. As part of a collaboration project, we published a paper at an international conference that was held in Bangkok, Thailand, towards the end of 2007.

- H. de Kock, M. Kamper, O. Ferreira, and R. Kennel, "Position Sensorless Control of the Reluctance Synchronous Machine considering High Frequency Inductances," in *Power Electronics and Drive Systems, 2007. PEDS'07*, 2007.

In 2008 I continued with the research on sensorless control in Wuppertal and we published two papers. One paper was at an international conference in Poznan in Poland. This paper has been submitted to and accepted by the IEEE Power Electronics Society (PELS) in November 2008 for publication in their international journal. The other paper is written in German and was published at a local German conference in Böblingen, near Stuttgart.

- H. de Kock, M. Kamper, and R. Kennel, "Anisotropy Comparison of Reluctance and PM Synchronous Machines for low speed Position Sensorless applications," in *13th International Conference on Power Electronics and Motion Control (EPE-PEMC)*, 2008.



- H. de Kock and R. Kennel, “Kompensation der Lastabhängigkeit von Industriellen Servoantrieben mit Geberloser Regelung,” in VDE/VDI-Fachtagung - Elektrischmechanische Antriebssysteme, 2008.

During the six months in 2007 that I was in Stellenbosch I did work on torque control with Mr. Arnold Rix for the machine that he and Prof. Kamper had designed and constructed. We published a paper at an international conference in Vilamoura, Portugal in September 2008. This paper is currently in the second review process for publication in the *Compel* journal.

- H. de Kock, A. Rix, and M. Kamper, “Optimal Torque Control of Interior Permanent Magnet Synchronous Machines in the Full Speed Range,” in Proceedings of the 2008 International Conference on Electrical Machines (ICEM), 2008.

Many results in this Ph.D thesis have not been published yet. It is expected that after the Ph.D thesis publication, additional conference and journal papers about the work presented here will follow.

# Contents

<b>Nomenclature</b>	<b>xiii</b>
<b>1 Introduction</b>	<b>1</b>
1.1 The next generation electrical machine drive . . . . .	1
1.2 Energy efficient and cost effective machine control . . . . .	3
1.3 Scope of the thesis . . . . .	3
1.4 Practical setup and simulation platforms . . . . .	4
1.5 Application 1: Electrical vehicle for urban use. . . . .	5
1.6 Application 2: Industry processes. . . . .	5
<b>2 Dynamic model of Synchronous Machines</b>	<b>7</b>
2.1 Space phasor theory . . . . .	7
2.2 Voltage and torque equations . . . . .	8
2.3 Summary of useful equations . . . . .	11
<b>3 Dynamic model of RSM</b>	<b>12</b>
3.1 Fundamental frequency RSM model using FE . . . . .	12
3.1.1 Geometric finite element model . . . . .	13
3.1.2 $dq$ model in Cartesian coordinates . . . . .	13
3.1.3 $dq$ model in polar coordinates . . . . .	15
3.1.4 Rated conditions . . . . .	18
3.1.5 $dq$ model in cylindrical coordinates . . . . .	18
3.2 Simulation methods . . . . .	19
3.2.1 Simulation with Matlab Simulink . . . . .	20
3.2.2 Simulation with Rapid Prototyping System: ANSI C . . . . .	22
3.3 Flux linkages: simulation vs. practical . . . . .	23
3.4 High frequency $dq$ model . . . . .	24
3.4.1 Practical measurements for HF parameters . . . . .	25
3.4.2 Simulation results for HF parameters . . . . .	26
<b>4 Field Orientated Control</b>	<b>30</b>
4.1 Field Orientated Control vs. Direct Torque Control . . . . .	30
4.2 Cascaded control structure . . . . .	31

<b>5</b>	<b>Voltage vector control</b>	<b>33</b>
5.1	Pulse width modulation . . . . .	33
<b>6</b>	<b>Current vector control</b>	<b>36</b>
6.1	PI current vector controller for RSM . . . . .	36
6.2	Zero-position . . . . .	37
6.3	Simulated and practical results . . . . .	38
<b>7</b>	<b>Torque control</b>	<b>43</b>
7.1	Optimal indirect torque control . . . . .	43
7.2	Optimal current vector reference . . . . .	45
7.3	Simulated and practical results . . . . .	48
7.4	Summary: torque control . . . . .	48
<b>8</b>	<b>Speed control</b>	<b>52</b>
8.1	Dynamic tests . . . . .	52
<b>9</b>	<b>Position sensorless control</b>	<b>54</b>
9.1	Fundamental model based position estimation . . . . .	55
9.1.1	Simulation and practical tests . . . . .	58
9.2	Position estimation using additional HF signals . . . . .	60
9.2.1	Anisotropy model . . . . .	62
9.2.2	Rotating HF voltage vector in the stationary reference frame . . . . .	62
9.2.3	Alternating HF voltage vector in the estimated anisotropy reference frame . . . . .	64
9.2.4	Simulation and practical tests . . . . .	67
9.2.5	HF machine model including mutual inductance . . . . .	74
9.3	Hybrid estimation structure . . . . .	76
9.4	Summary for sensorless control . . . . .	77
<b>10</b>	<b>Conclusions</b>	<b>81</b>
<b>11</b>	<b>Recommendations</b>	<b>86</b>
<b>A</b>	<b>Trigonometric identities</b>	<b>101</b>
<b>B</b>	<b>File Attachments</b>	<b>102</b>
B.1	RSM simulation in Matlab Simulink . . . . .	102
B.2	Four quadrant lookup tables generation. . . . .	103
B.3	Torque control lookup tables generation. . . . .	103
B.4	RSM control and simulation code for RPS. . . . .	103

# List of Figures

1.1	Practical test bench. . . . .	6
3.1	RSM model in FE. . . . .	14
3.2	FE results: current to flux linkage mapping. . . . .	14
3.3	Flux linkage and torque ripple for rated conditions. . . . .	15
3.4	FE results: fundamental model in Cartesian coordinates. . . . .	16
3.5	FE results: fundamental model in polar coordinates. . . . .	17
3.6	Vector diagram of rated conditions. . . . .	18
3.7	FE results: fundamental model in cylindrical coordinates (variation with $\theta_r$ ). . . . .	19
3.8	Simulink: $ABC$ model. . . . .	20
3.9	Simulink: $\alpha\beta$ model. . . . .	20
3.10	Simulink: $dq$ model. . . . .	21
3.11	Simulink: Electrical model, $dq$ model expanded. . . . .	21
3.12	Simulink: Inverse 2D LUTs with 2D interpolation. . . . .	22
3.13	Simulink: Indirect torque control. . . . .	22
3.14	Fundamental model: simulation vs. practical results at rated speed. . . . .	27
3.15	Calculated HF inductances from measured data. . . . .	28
3.16	Calculated HF inductances from simulated data. . . . .	29
4.1	Cascaded control structure. . . . .	32
5.1	Voltage vector control using PWM. . . . .	34
5.2	Dead-time measurement. . . . .	35
5.3	Sinusoidal vs. modified PWM references. . . . .	35
6.1	Current vector control block diagram. . . . .	37
6.2	Aligning the measured- and actual electrical rotor position. . . . .	38
6.3	$d$ -axis current control: simulation and practical results. . . . .	40
6.4	$q$ -axis current control: simulation and practical results. . . . .	41
6.5	MTPA-axis current control: simulation and practical results. . . . .	42
7.1	Torque control block diagram. . . . .	45
7.2	Three examples for torque control table creation. . . . .	46
7.3	Torque control lookup table creation. . . . .	46

7.4	Torque control: lookup tables. . . . .	47
7.5	Expected torque and flux linkage magnitudes. . . . .	47
7.6	Program for LUTs creation flow diagram. . . . .	50
7.7	Torque control dynamic test - simulation and practical results. . . . .	51
7.8	Torque vs Speed - simulation and practical results. . . . .	51
8.1	Speed control: no load dynamic tests. . . . .	53
9.1	Position estimated based on fundamental model . . . . .	58
9.2	Flux linkage estimation based on back-EMF. . . . .	59
9.3	Measured vs. estimated cos and sin . . . . .	60
9.4	Measured vs. estimated rotor position . . . . .	60
9.5	Fundamental model: simulation vs. practical using observer structure . . . . .	61
9.6	Position estimated based on rotating HF . . . . .	65
9.7	Position estimated based on alternating HF . . . . .	67
9.8	Rotating HF observer: speed dependence test. . . . .	69
9.9	Rotating HF observer: load dependence test. . . . .	70
9.10	Alternating HF observer: speed dependence test. . . . .	71
9.11	Alternating HF observer: load dependence test. . . . .	72
9.12	Alternating HF observer: detected position . . . . .	73
9.13	Alternating HF observer: estimated position error under load . . . . .	79
9.14	Sensorless control - load test . . . . .	80
9.15	Dynamic estimator test. . . . .	80

# List of Tables

- 2.1 Useful equations for synchronous machines . . . . . 11
- 3.1 RSM rated values and related information . . . . . 19

# Nomenclature

## Acronyms

---

$\alpha\beta$	two axes stationary reference frame
ABC	three phase stationary reference frame
ANSI-C	American National Standards Institute C programming language
BPF	band pass filter
$dq$	direct quadrature - synchronously rotating reference frame
DSP	digital signal processor
DTC	direct torque control
EMF	electro motive force
FE	finite element
FOC	field orientated control
FW	field weakening
HF	high frequency (generally speaking about the range 500 - 2000 Hz)
IGBT	insulated gate bi-polar transistor
IPMSM	interior PMSM
ISR	interrupt service routine
LPF	low pass filter
LUT	look-up table
MMF	magneto motive force
MOSFET	metal-oxide semi-conductor field effect transistor
MTPA	maximum torque per Ampere
PI	proportional integral
PLL	phase locked loop
PWM	pulse width modulation
PMARSM	PM assisted RSM
PMSM	Permanent Magnet Synchronous Machine
RPS	rapid prototyping system
RSM	Reluctance Synchronous Machine
RTAI	real-time applications interface of the Linux operating system
VSI	voltage source inverter
VSD	variable speed drive
SVPWM	space vector PWM

## Variables

---

symbol	description
$i_a$	instantaneous value of the phase A current
$i_b$	instantaneous value of the phase B current
$i_c$	instantaneous value of the phase C current
$i_0$	zero sequence current
$\vec{i}_s = i_s \angle \phi_s$	current space vector in the stationary reference frame
$\vec{i}_s = i_\alpha + j i_\beta$	$\alpha\beta$ current components in the stationary reference frame
$\vec{i}_r = i_r \angle \phi_r$	current space vector in the synchronously rotating reference frame
$\vec{i}_r = i_d + j i_q$	$dq$ current components in the synchronously rotating reference frame
$\vec{u}_s = u_s \angle \alpha_s$	voltage space vector in the stationary reference frame
$\vec{u}_s = u_\alpha + j u_\beta$	$\alpha\beta$ voltage components in the stationary reference frame
$\vec{u}_r = u_r \angle \alpha_r$	voltage space vector in the synchronously rotating reference frame
$\vec{u}_r = u_d + j u_q$	$dq$ voltage components in the synchronously rotating reference frame
$\vec{\psi}_s = \psi_s \angle \delta_s$	flux linkage space vector in the stationary reference frame
$\vec{\psi}_s = \psi_\alpha + j \psi_\beta$	$\alpha\beta$ flux linkage components in the stationary reference frame
$\vec{\psi}_r = \psi_r \angle \delta_r$	flux linkage space vector in the synchronously rotating reference frame
$\vec{\psi}_r = \psi_d + j \psi_q$	$dq$ flux linkage components in the synchronously rotating reference frame
$R_s$	stator winding resistance per phase
$\theta_r$	electrical rotor position
$\omega_r$	electrical rotor speed
$p$	number of pole pairs
$\theta_m$	mechanical rotor position
$\omega_m$	mechanical rotor speed
$T_m$	machine torque
$T_L$	load torque
$J_{eq}$	equivalent system inertia
$B_{eq}$	equivalent system friction
$L_t$	tangential (differential) inductance
$L_s$	secant inductance
$U_{dc}$	DC bus voltage
$\omega_{HF}$	rotational speed of high frequency space vectors
$\omega_r^*$	electrical rotor speed reference
$T_m^*$	torque reference
$\vec{i}_r^*$	current space vector reference in the $dq$ reference frame
$\hat{\omega}_r$	estimated rotor speed
$U_{max}$	maximum achievable voltage vector magnitude
$\vec{u}_r^*$	voltage space vector reference in the $dq$ reference frame
$\hat{\psi}_r^*$	flux linkage vector estimate in the $dq$ reference frame



symbol	description
$K_p$	proportional gain
$K_i$	integral gain
$ \psi_r _{MAX}$	maximum achievable flux linkage vector magnitude
$L_{dA}$	$d$ -axis inductance in the anisotropy reference frame
$L_{dA}$	$q$ -axis inductance in the anisotropy reference frame
$\theta_A$	anisotropy position
$\omega_A$	anisotropy speed
$U_{HF}$	high frequency voltage vector magnitude
$\vec{i}_{HF}$	high frequency current vector
$\vec{A}$	anisotropy vector
$\zeta$	phase shift due to digital delay
$\delta$	high frequency voltage injection direction
$\theta_{comp}$	compensation angle
$L_{dq} = M_t$	mutual tangential inductance
$\hat{T}_m$	estimated machine torque

## Operations

---

- $\times$  vector cross product
- $\cdot$  vector dot product
- $\otimes$  vector direct product (all components multiplied)

# Chapter 1

## Introduction

The focus on high efficiency and cost effective drives, for applications ranging from washing machines to electrical cars, has led to the adoption of certain types of synchronous machines, with control algorithms that maximize energy efficiency and avoid the use of expensive sensors. In this chapter a family of machines, which are likely to be used more often in the future are introduced. For good performance, the machine control and design strategies are equally important. This chapter starts by introducing the next generation electrical drive, and then lists the control system criteria. As any work is limited to a certain period of time, the scope of this thesis is given and the intended applications are highlighted.

The rest of the thesis is structured in chapters as follows: the basic electrical machine model which is applicable to the family of synchronous machines, is given and is then followed by an in depth analysis of a Reluctance Synchronous Machine (RSM) that is used as an example in this thesis. In the rest of the thesis the focus is on machine control and the chapters start with the explanation of field orientated control, after which the various parts of the control system are explained, i.e. voltage vector control, current vector control, torque control and speed control. An in depth study of position sensorless control, i.e. rotor position and speed estimation, is then presented. Finally conclusions are drawn and recommendations for future research and industrial implementation are made.

### 1.1 The next generation electrical machine drive

The word “drive” is used here to indicate that the system in question is the classical variable speed drive (VSD), where an electrical machine is fed by a voltage source inverter (VSI). For direct on-line grid-connected machines, an induction (asynchronous) machine is typically used. However, there have also been investigations on a Permanent Magnet (PM) motor with an induction rotor cage [1, 2, 3], for direct grid connection. A variable speed drive with very good efficiency may be obtained by using a power converter between the electrical grid and the electrical machine. Traditionally this machine is also an induction machine, but there is a shift towards other kinds of electrical machines that promise even better efficiency.

The Permanent Magnet Synchronous Machine (PMSM) is widely accepted in industry,

due to its high efficiency, high power density, high torque-to-inertia ratio, wide speed operation range and because it is practically maintenance free. Moreover, the kind of PMSM that exhibits magnetic anisotropy characteristics is advantageous, since it can be used for position sensorless control at zero speed [4]. The Interior Permanent Magnet Synchronous Machine (IPMSM) is known for its saliency characteristics and has been used as a position sensorless drive [5, 6, 7, 8, 9, 10, 11, 12]. The use of concentrated stator windings (instead of distributed stator windings) represents another cost-saving effort, although this has some implications for the fundamental control, as well as sensorless control [13]. It is clear that the structure of the rotor also has a large influence on its suitability for position sensorless control [14, 15].

It has been shown that the Reluctance Synchronous Machine (RSM) is a viable alternative for induction machines for some applications [16]. However, the machine must be controlled position sensorless so that it can compete with the industry standard induction machine [17, 18, 19, 20, 21, 22, 23, 24, 25, 26, 27, 28, 29, 30, 31, 32]. The RSM has a limited flux-weakening speed range, and it has been shown that the inclusion of weak permanent magnets in the rotor flux barriers improves the flux-weakening performance [33, 34]. The Permanent Magnet assisted Reluctance Synchronous Machine (PMARSM) has also been used as a position sensorless drive [35, 36].

This family of machines, namely PMSM, IPMSM, RSM and PMARSM, is likely to replace the industry standard induction machine (for a specific power range, e.g. less than 100 kW) in the future, since there is a strong need for more energy efficient machines. In short, the induction machine has a rotor with an aluminium cage (this takes a lot of energy to manufacture) and there are conductive power losses ( $i^2 \cdot R$ ) on the rotor. The RSM has a rotor that is manufactured by only stacking a number of steel laminations, i.e. there are no permanent magnets, no aluminium cage and no conductive power losses on the rotor. The synchronous machines that have permanent magnets in their rotors are more expensive and energy costly to manufacture compared to the RSM, but they have no conductive losses on the rotor due to the lack of any rotor windings.

In a recent survey [37], it has been shown that in the United States of America 57% of all electricity is used for electrical motors that are used in a large variety of applications and processes, e.g. fans and pumps. It is therefore definitely justified to acquire new technology concerning electrical machines and machine control that will result in an increase in energy efficiency. Research about this topic has been going on since the 1990's, but a major part of the industry's requirements are still being satisfied by the induction machine. It could be that the slow acquisition of this new technology on the industry's part is not due to the lack of expertise in machine design, but rather due to the lack of expertise in reliable and cost effective machine control. This thesis is focused on the control of the next generation electrical machine drive.

## 1.2 Energy efficient and cost effective machine control

With a range of possible cost effective machine designs that may be offered, consider now the control system requirements, which depend strongly on the application, but in general could be listed as follows:

1. Energy efficient torque control in the entire speed range
2. Position sensorless control (no encoder or resolver)
3. A good dynamic response
4. Robust and machine model independent
5. Low audible noise

Several works concerning these topics have been presented and the viewpoints vary widely. Two main schools of thought have emerged to fulfil the control system requirements, namely direct torque control (DTC) [38, 39, 40, 7, 41, 42, 43, 44] and field orientated control (FOC) [45, 46, 47, 48, 49, 50, 51, 52], although it is not always possible to make such a clear distinction and sometimes a combination of methods or a different approach is used.

In this thesis, the FOC school of thought is followed and it is shown how energy efficient torque control in the entire speed range, without the need of a position sensor and with good dynamic response can be achieved. The methods are however machine model dependent and although some thought was given to low audible noise, this criterion is not always satisfied. Some attention is also paid to ease of implementation, since this will increase the acceptance of these ideas in the industry.

## 1.3 Scope of the thesis

The concepts and ideas presented in this thesis are applicable for the family of synchronous machines introduced, namely PMSM, IPMSM, RSM and PMARSM. The thesis is the fusion of work that started with a PMARSM [53, 54, 34], then continued with a RSM [32, 55] and also included work with an IPMSM [56] and a PMSM [55, 57]. Throughout this thesis a RSM is taken as example, but care is taken to keep the theory as generic as possible. This thesis focuses on optimal torque control (energy efficient) and position sensorless control (robust, reliable and cost effective) in the entire speed range.

As mentioned, the stator winding type has an influence on the machine control and position estimation [13]. The torque control algorithm presented in this thesis using a RSM as example, is based on work that was performed on an IPMSM [56]. This IPMSM has concentrated stator windings, also referred to as fractional slot or non-overlapping windings [58]. The winding type has therefore had no serious impact on the torque control algorithm and so the algorithm can be regarded as generic. The influence of the stator winding type on

the rotor position estimation has not been addressed directly in this work, since most of the sensorless tests were performed on machines with the classical distributed windings. This is however a new and exciting topic and research publications about it are sure to follow in the future.

## 1.4 Practical setup and simulation platforms

A central aspect for verifying and testing the developed ideas is the availability of a trustworthy simulation platform and a practical setup. The RSM used as an example in this thesis was designed and constructed at the University of Stellenbosch in South Africa. A standard induction machine on 2 kW power level was purchased and the rotor was replaced by an optimally designed reluctance rotor. The rotor design was done using Finite Element (FE) software, which is non-commercial software known as the “Cambridge package”. It was developed by the University of Cambridge (United Kingdom) and optimization algorithms were added to it by the University of Stellenbosch (South Africa) in the 1990’s.

Using this FE program, an accurate electrical machine model of the RSM can be obtained and is then used inside a simulation model. At first the Matlab Simulink platform was used to perform control system simulations. Of course the work has to be tested practically also, and in many cases the control system has to be re-implemented in ANSI C code, for example. The RSM was sent to the University of Wuppertal in Germany as part of a collaboration project on position sensorless control. The University of Wuppertal has developed a Rapid Prototyping System (RPS) for laboratory environments [59]. During the course of this work, the RPS was programmed so that simulation could also be done. Therefore, the RPS was used as a “hardware in the loop system”, whereby the control system is implemented, simulation is performed and the results are verified practically, without having to implement or debug anything more than once.

Most of the work concerning the machine control of the RSM was performed in the laboratory at the University of Wuppertal. However, a substantial part of the work in general was performed at the University of Stellenbosch. A system diagram of the practical setup is shown in Fig. 1.1(a). In the diagram the block M1 refers to the RSM, and M2 is the load machine (a commercial PMSM from the company SEW Eurodrive AG was used). The torque sensor shown was unfortunately not available in the actual setup. A picture of the RPS is shown in Fig. 1.1(b) and a picture of the machines and inverters is shown in Fig. 1.1(c).

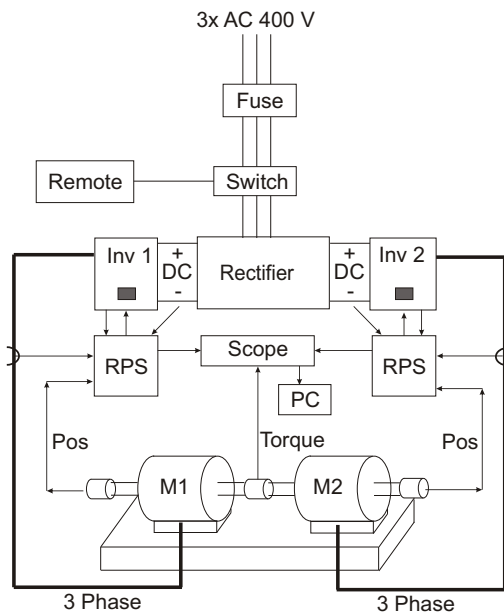
## 1.5 Application 1: Electrical vehicle for urban use.

The work on torque control in this thesis is based on research that was started for an interior permanent magnet synchronous machine (IPMSM) for an electrical vehicle application. The project was started in 2005 by a South African company named “Optimal Energy” ([www.optimalenergy.co.za](http://www.optimalenergy.co.za)) that sought the expertise of the Electrical Machines group at the University of Stellenbosch. The first prototype IPMSM was designed and optimized in FE software and constructed for testing [58]. It is an in-wheel motor, also called a hub-motor, and it is characterized by its high performance and compact design. By using concentrated stator windings (also known as fractional slot, or non-overlapping windings), the machine has a large field weakening range, which is necessary for this application.

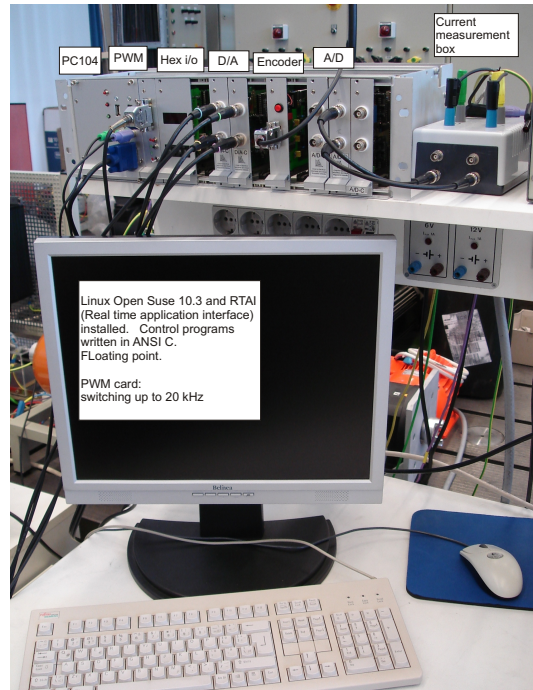
In 2006 work started on the design of a torque control algorithm that works from zero to maximum speed and for large variance in DC bus voltage; that is energy efficient and easy to implement. The developed algorithm was implemented and tested on a practical test bench with good results, which were published at an international conference in 2008 [56]. This project continues and a second version of the hub-motor has been designed and constructed; the optimal torque control technique has been implemented for it as well (results have not been published yet). A prototype electrical car for urban use, named “Joule”, was demonstrated by Optimal Energy at the 2008 Paris motor show [60]. It is almost certain that the hub-motor technology with optimal torque control will be incorporated into the Joule.

## 1.6 Application 2: Industry processes.

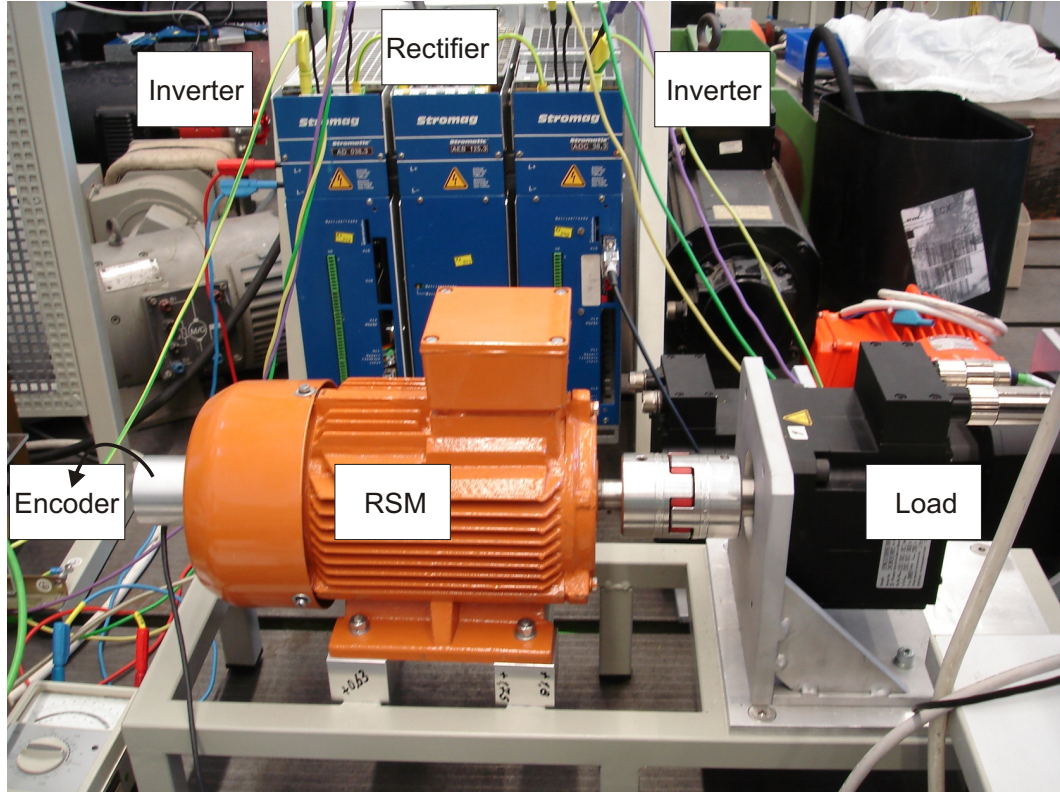
A very large portion of electrical machines are used in general industrial applications like fans and pumps [37]. Stand-alone and direct grid-connected induction machines usually satisfy the industry’s needs for these applications. However, as it becomes more and more apparent that energy must be saved globally and the cost of energy rises, people are considering ways in which to achieve better utilization of energy for these applications. One idea is to insert a power converter between the grid and the standard induction machine, so that it is transformed into a variable speed drive (VSD) that can be controlled to be very efficient. However, if the induction machine is replaced by a RSM, a PMSM, a PMARSM or a IPMSM depending on the application, and the optimal torque control and rotor position estimation algorithms are in place, there could be an even greater increase in energy efficiency and a reduction in cost. In South Africa, for example, the mining and petro-chemical industries have a very large potential to save electricity in this way.



(a) Diagram of the laboratory setup.



(b) Rapid Prototyping System (RPS).



(c) RSM, load machine and inverters.

Figure 1.1: Practical test bench.

# Chapter 2

## Dynamic model of Synchronous Machines

In this chapter the space phasor theory as applied to synchronous machines will be described briefly and the important equations that describe the synchronous machine mathematically will be given.

### 2.1 Space phasor theory

In the modelling of alternating current (AC) machines, and specifically regarding vector-controlled machines, it is very common to use space phasor theory [61,62]. The word “phasor” refers in general mathematics to the amplitude and phase angle of a sine wave; it can be represented mathematically by a complex number (Cartesian) or equivalently using Euler’s notation (polar). In AC machines, we are concerned with the spatial distribution of the magneto motive force (MMF) inside the machine. In the ideal case, this spatial distribution is perfectly sinusoidal with respect to the angle around the periphery: this provides us with the possibility of using phasor theory. However, since we are talking about a spatial sinusoidal distribution and not a time sinusoidal distribution, we use the term “space phasor”. It is very common to use the term “space vector” equivalently, where vector in this sense is also just a complex number. Also, in the texts that follow, the short terms “vector” or “phasor” will mean “space phasor”.

In a smooth-air-gap AC machine with three-phase distributed stator windings (neglecting the end-winding and the effects of slotting and iron-losses) a balanced set of three-phase currents will cause a MMF that has a near perfect sinusoidal distribution around the air-gap. Furthermore, the types of AC machines considered here do not have any windings on the rotor, i.e. the reluctance synchronous machine (RSM), the permanent magnet assisted reluctance synchronous machine (PMARSM), the permanent magnet synchronous machine (PMSM) and the interior permanent magnet synchronous machine (IPMSM) are considered.

The space phasor  $\vec{i}_s$  (with its polar and Cartesian forms given in (2.1)) represents the spatial distribution of the currents in the three-phase stator windings around the air-gap as



in (2.2). In (2.2)  $i_a = i_a(t)$  is the instantaneous value of the current in phase A, and the same applies to  $i_b$  and  $i_c$ . This transformation from three-phase to quadrature-phase components has the non-power invariant form, due to the choice of the constant  $\frac{2}{3}$ . This has the useful consequence that if a balanced set of three-phase currents applies (which is usually the case), then the modulus  $i_s$  gives the peak value of the three-phase currents. [In the power invariant form, the constant should be  $\sqrt{\frac{2}{3}}$ ].

The space phasor  $\vec{i}_s$  does not contain the zero-sequence current: an additional definition is needed, as in (2.3). If a balanced set of three-phase currents applies, then  $i_{s0} = 0$ . The constant  $\frac{1}{3}$  complies with the non-power invariant form. [In the power invariant form, the constant should be  $\sqrt{\frac{1}{3}}$ ].

From equations (2.1) through (2.3), the forward and reverse transformations from the stationary  $ABC$  reference frame to the stationary  $\alpha\beta 0$  reference frame is given in matrix form in (2.4) and (2.5). The transformations are given for current here, but apply in general to other variables like voltage and flux linkage. Generally, the zero sequence component is not calculated, since it is assumed to be zero. Therefore in the following texts, we will speak of the stationary  $\alpha\beta$  reference frame.

$$\vec{i}_s = i_s \angle \phi_s = i_\alpha + j i_\beta \quad (2.1)$$

$$= \frac{2}{3} \left( i_a + i_b e^{j \frac{2\pi}{3}} + i_c e^{j \frac{4\pi}{3}} \right) \quad (2.2)$$

$$i_{s0} = \frac{1}{3} (i_a + i_b + i_c) \quad (2.3)$$

$$\begin{bmatrix} i_\alpha \\ i_\beta \\ i_0 \end{bmatrix} = \frac{2}{3} \begin{bmatrix} 1 & -\frac{1}{2} & -\frac{1}{2} \\ 0 & \frac{\sqrt{3}}{2} & -\frac{\sqrt{3}}{2} \\ \frac{1}{2} & \frac{1}{2} & \frac{1}{2} \end{bmatrix} \begin{bmatrix} i_a \\ i_b \\ i_c \end{bmatrix} \quad (2.4)$$

$$\begin{bmatrix} i_a \\ i_b \\ i_c \end{bmatrix} = \begin{bmatrix} 1 & 0 & 1 \\ -\frac{1}{2} & \frac{\sqrt{3}}{2} & 1 \\ -\frac{1}{2} & -\frac{\sqrt{3}}{2} & 1 \end{bmatrix} \begin{bmatrix} i_\alpha \\ i_\beta \\ i_0 \end{bmatrix} \quad (2.5)$$

## 2.2 Voltage and torque equations

In the stationary  $\alpha\beta$  reference frame, the voltage equation in space phasor notation is given by (2.6). In this equation,  $R_s$  is the stator resistance per phase, and  $\vec{\psi}_s$  is the total air-gap flux linkage that includes the stator leakage flux linkage, but excludes the end-winding flux linkage.  $\vec{\psi}_s$  is a function of the magnetizing current  $\vec{i}_s$  and has in theory a perfect sinusoidal distribution around the air-gap. Therefore, in this stationary reference frame, all space vectors are rotating at the electrical speed  $\omega_r$ , i.e. real and imaginary components ( $\alpha$  and  $\beta$  components) are co-sinusoidal and sinusoidal functions of  $\theta_r$  respectively.

$$\vec{u}_s = R_s \vec{i}_s + \frac{d\vec{\psi}_s}{dt} \quad (2.6)$$

Consider implementing a current vector controller to control  $\vec{i}_s$ . Since the  $\vec{i}_s$  vector is rotating at speed  $\omega_r$ , the current vector controller needs to have a bandwidth that is greater than the maximum  $\omega_r$ , and there will be a problem with phase shift. To overcome this problem, a transformation to a reference frame (called the  $dq$  reference frame) positioned at  $\theta_r$  (i.e. fixed to the rotor) is introduced.

Fictitious quadrature stator coils that rotate synchronously with the rotor are introduced. The stator current vector in the synchronously rotating  $dq$  reference frame is given by (2.7), where the transformation from the stationary  $\alpha\beta$  reference frame is given by (2.8).

Some readers that are familiar with the vector notation as used for example in [61], may be confused at this point. In [61] the subscript r refers to the rotor quantities (rotor current, rotor flux linkage etc.) and the subscript s refers to the stator quantities. The work in [61] is with reference to the induction machine. It must be stressed here that for the family of synchronous machines considered in this work, there are no rotor windings and therefore also no rotor current or any losses on the rotor for that matter. There is only one stator voltage vector, one magnetizing current vector and one air-gap flux linkage vector. The subscript r in this work refers only the reference frame attached to the rotor, and the subscript s refers to the reference frame attached to the stator. Each vector represents only one quantity, but it may be viewed from any reference frame, which is indicated by the subscript.

As already mentioned, the space vectors do not include the zero-sequence component, so for a complete component description the transformations are given in matrix form in (2.10) and (2.11).

$$\vec{i}_r = i_r \angle \phi_r = i_d + j i_q \quad (2.7)$$

$$= \vec{i}_s e^{-j\theta_r} \quad (2.8)$$

$$\vec{i}_s = \vec{i}_r e^{j\theta_r} \quad (2.9)$$

$$i_s = i_r$$

$$\phi_s = \theta_r + \phi_r$$

$$\begin{bmatrix} i_d \\ i_q \\ i_0 \end{bmatrix} = \begin{bmatrix} \cos \theta_r & \sin \theta_r & 0 \\ -\sin \theta_r & \cos \theta_r & 0 \\ 0 & 0 & 1 \end{bmatrix} \begin{bmatrix} i_\alpha \\ i_\beta \\ i_0 \end{bmatrix} \quad (2.10)$$

$$\begin{bmatrix} i_\alpha \\ i_\beta \\ i_0 \end{bmatrix} = \begin{bmatrix} \cos \theta_r & -\sin \theta_r & 0 \\ \sin \theta_r & \cos \theta_r & 0 \\ 0 & 0 & 1 \end{bmatrix} \begin{bmatrix} i_d \\ i_q \\ i_0 \end{bmatrix} \quad (2.11)$$

The voltage equation in the synchronously rotating  $dq$  reference frame, and the transformation from the stationary  $\alpha\beta$  reference frame, are given in (2.12). In the  $dq$  reference frame, in the steady state, and if  $\vec{\psi}_s$  has a truly sinusoidal distribution in space, the vectors  $\vec{u}_r$ ,  $\vec{\psi}_r$  and  $\vec{i}_r$  have constant complex values. Furthermore,  $\vec{\psi}_r$  is now only a function of  $\vec{i}_r$ . It is much easier to design a vector controller for stationary vectors than for rotating vectors. For example a proportional integral (PI) controller might be used.

$$\begin{aligned}
 \vec{u}_r &= \vec{u}_s e^{-j\theta_r} & (2.12) \\
 &= \left[ R_s (\vec{i}_r e^{j\theta_r}) + \frac{d}{dt} (\vec{\psi}_r e^{j\theta_r}) \right] e^{-j\theta_r} \\
 &= R_s \vec{i}_r + \frac{d\vec{\psi}_r}{dt} + j \frac{d\theta_r}{dt} \vec{\psi}_r \\
 &= R_s \vec{i}_r + \frac{d\vec{\psi}_r}{dt} + j\omega_r \vec{\psi}_r
 \end{aligned}$$

The torque produced by the machine can be expressed mathematically by (2.13) in the stationary reference frame or (2.14) in the rotating reference frame, where  $p$  is the number of pole pairs. The torque is the dot (scalar) product of the current vector with the  $90^\circ$  rotated flux linkage vector. The factor  $\frac{3}{2}$  is due to the fact that the transformation used is non-power invariant (the factor must be used anytime that energy or power quantities are computed using transformed voltages and/or currents). The parameter  $p$  is the number of pole pairs, which is the ratio between electrical and mechanical speed.

$$T_m = \frac{3p}{2} \vec{i}_s \cdot j\vec{\psi}_s = \frac{3p}{2} (\psi_\alpha i_\beta - \psi_\beta i_\alpha) = \frac{3p}{2} \psi_s i_s \sin(\phi_s - \delta_s) \quad (2.13)$$

$$= \frac{3p}{2} \vec{i}_r \cdot j\vec{\psi}_r = \frac{3p}{2} (\psi_d i_q - \psi_q i_d) = \frac{3p}{2} \psi_r i_r \sin(\phi_r - \delta_r) \quad (2.14)$$

The standard equation used to model the mechanical subsystem is given by (2.15), where  $J_{eq}$  is the equivalent system inertia and  $B_{eq}$  is the equivalent system friction coefficient. Equation (2.16) states that the electrical speed  $\omega_r$  (in rad/sec) is related to the mechanical speed  $\omega_m$  by the number of pole pairs  $p$ .

$$T_m = T_L + J_{eq} \frac{d\omega_m}{dt} + B_{eq} \omega_m \quad (2.15)$$

$$\omega_r = p \cdot \omega_m \quad (2.16)$$

## 2.3 Summary of useful equations

**Table 2.1:** Useful equations for synchronous machines

Stator current vector		
$\vec{i}_r = i_r \angle \phi_r = i_d + j i_q$	$\vec{i}_r = \vec{i}_s e^{-j\theta_r}$	$i_r = i_s$
$\vec{i}_s = i_s \angle \phi_s = i_\alpha + j i_\beta$	$\vec{i}_s = \vec{i}_r e^{j\theta_r}$	$\phi_s = \phi_r + \theta_r$
Total (airgap and leakage) flux linkage vector		
$\vec{\psi}_r = \psi_r \angle \delta_r = \psi_d + j \psi_q$	$\vec{\psi}_r = \vec{\psi}_s e^{-j\theta_r}$	$\psi_r = \psi_s$
$\vec{\psi}_s = \psi_s \angle \delta_s = \psi_\alpha + j \psi_\beta$	$\vec{\psi}_s = \vec{\psi}_r e^{j\theta_r}$	$\delta_s = \delta_r + \theta_r$
Stator voltage vector		
$\vec{u}_r = u_r \angle \alpha_r = u_d + j u_q$	$\vec{u}_r = \vec{u}_s e^{-j\theta_r}$	$u_r = u_s$
$\vec{u}_s = u_s \angle \alpha_s = u_\alpha + j u_\beta$	$\vec{u}_s = \vec{u}_r e^{j\theta_r}$	$\alpha_s = \alpha_r + \theta_r$
$\vec{u}_r = R_s \vec{i}_r + \frac{d\vec{\psi}_r}{dt} + j\omega_r \vec{\psi}_r$	$\vec{u}_s = R_s \vec{i}_s + \frac{d\vec{\psi}_s}{dt}$	
Torque		
$T_m = \frac{3p}{2} \vec{i}_r \cdot j \vec{\psi}_r = \frac{3p}{2} \psi_r i_r \sin(\phi_r - \delta_r)$	$T_m = \frac{3p}{2} (\psi_d i_q - \psi_q i_d)$	
$T_m = \frac{3p}{2} \vec{i}_s \cdot j \vec{\psi}_s = \frac{3p}{2} \psi_s i_s \sin(\phi_s - \delta_s)$	$T_m = \frac{3p}{2} (\psi_\alpha i_\beta - \psi_\beta i_\alpha)$	
$T_m = T_L + J_{eq} \frac{d\omega_m}{dt} + B_{eq} \omega_m$	$\omega_r = p \cdot \omega_m$	

# Chapter 3

## Dynamic model of RSM

In chapter 2 the dynamic model of synchronous machines is given in general, in terms of space vectors for stator voltage, magnetizing current and total flux linkage (air-gap and leakage). The ideas described are applicable for a family of synchronous machines that do not have windings on the rotor, i.e. RSM, PMARSM, PMSM and IPMSM. This chapter further expands on that model taking a RSM as example. The RSM is modelled in a Finite Element (FE) program and results from this program are used to give an accurate description of the electrical parameters of the machine.

The chapter starts by introducing the FE program in section 3.1. The modelled RSM geometry is shown and discussed. The machine parameters are then shown in Cartesian, polar and cylindrical coordinates to provide deep insight into the machine. In section 3.2 it is shown how the machine with its control system can be simulated. In section 3.3 parameter identification methods are applied in order to obtain machine parameters. Simulation and practical results are shown that can be compared to the direct results from FE in section 3.1. Finally a high frequency model of the RSM is presented in section 3.4. Again simulation and practical results are shown, which may be compared to the results of sections 3.3 and 3.1.

This chapter provides the necessary insight to enable the design of an optimal torque control algorithm and a rotor position estimation algorithm for the entire speed range. The RSM is given as example, but the ideas are applicable for all synchronous machines without rotor windings.

### 3.1 Fundamental frequency RSM model using FE

The RSM given as example in this section comprises of a standard three-phase distributed winding induction machine stator and a custom designed two pole-pair rotor that was optimized for performance using a non-commercial FE software package, known as the Cambridge Package, which was developed as a collaboration project between the University of Stellenbosch and the University of Cambridge in the 1990's. The rotor is constructed using laser-cut steal laminations, i.e. it is transverse laminated. The geometric FE model is only a

quarter machine model, since symmetry applies. This model is first introduced, after which a detailed discussion with results from FE analysis follows.

### 3.1.1 Geometric finite element model

The geometric model for the FE program of a RSM is shown in Fig. 3.1. It is a quarter model, since the rotor has two pole-pairs. It is a cross-section of a quarter of the RSM, therefore a 2D model, and the results are calculated taking the rotor stack length into account. The rotor is not skewed.

In Fig. 3.1(a) the quarter RSM model with its mesh grid is shown. In the rotor geometry two flux barriers are clearly visible. The radial axis that is centred on these flux barriers are denoted as the  $q$ -axis. Electrically, the  $d$ -axis that is perpendicular to the  $q$ -axis. Since the machine has two pole-pairs, the  $q$ -axis and  $d$ -axis are separated mechanically by 45 degrees. Flux may flow freely in the  $d$ -axis, but is restricted in the  $q$ -axis. Simply speaking, this fact causes the  $d$ -axis inductance to be larger than the  $q$ -axis inductance. Now it is also clear why it is convenient to describe the machine in terms of the  $dq$ -axes.

A macro airgap element (not meshed) is used and the air-gap flux linkage vector and the torque are solved analytically (not numerically). This enables the solutions to be calculated more easily and also allows the rotor to move with reference to the stator. Fig. 3.1(b) shows a field plot, where the colours represent the average magnetic vector potential in a triangle. The flux lines are the equipotential lines, i.e. lines of constant vector potential.

The inputs to the FE program are the currents in the stator coils and the rotor position. More specifically, the magnetizing current space vector is given as input (assuming that the magnetizing current is equal to the terminal current), for a certain rotor position, and the air-gap flux linkage space vector is obtained as output. Using this method, an accurate electrical description of the machine can be obtained that takes into account saturation and cross-coupling between  $d$ -axis and  $q$ -axis.

Inside the FE program there is also an analytical method to calculate the stator resistance as a function of temperature, as well as other post-processing methods that use empirical formulas to calculate end-winding losses and core losses. However, these features are not considered in this chapter.

### 3.1.2 $dq$ model in Cartesian coordinates

For a single rotor position, the magnetizing current vector in the synchronously rotating  $dq$  reference frame, is given in its  $d$  and  $q$  components that span a large area of possible working points. For each of these points, the airgap flux linkage vector in the synchronously rotating reference frame in terms of its  $d$  and  $q$  components are calculated using the FE program. The result for the  $d$ -axis flux linkage is shown in Fig. 3.2(a), and the result for the  $q$ -axis flux linkage is shown in Fig. 3.2(b). Within these results, all saturation and cross-coupling phenomena are contained.

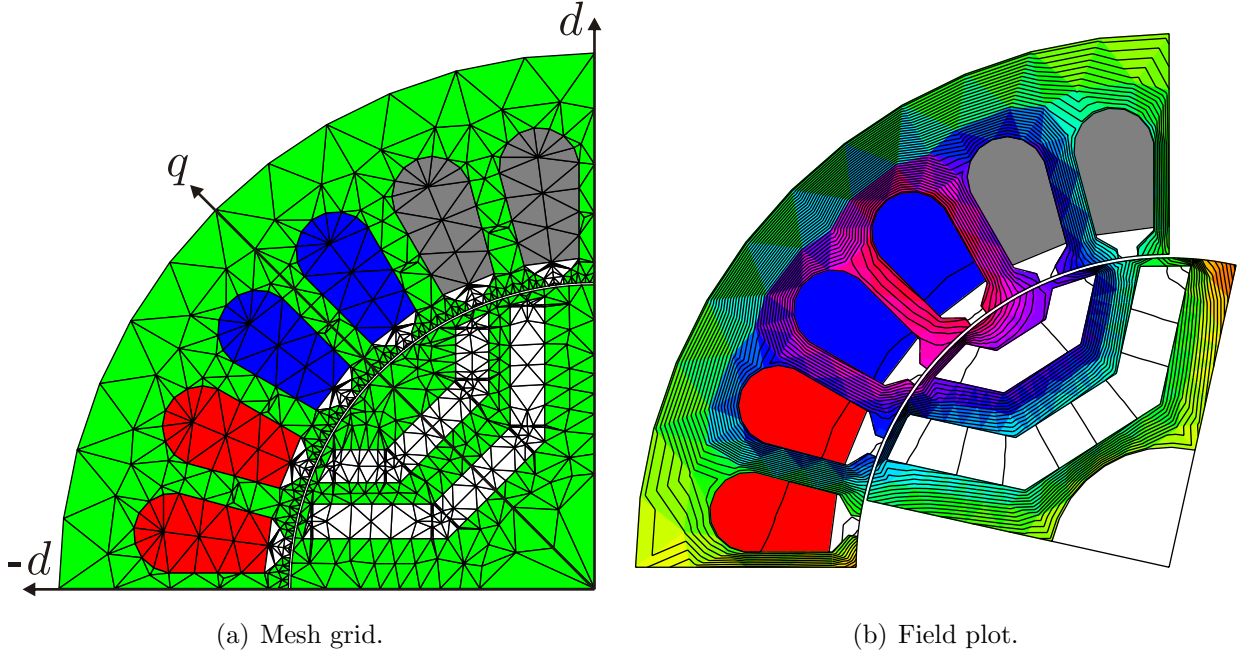


Figure 3.1: RSM model in FE.

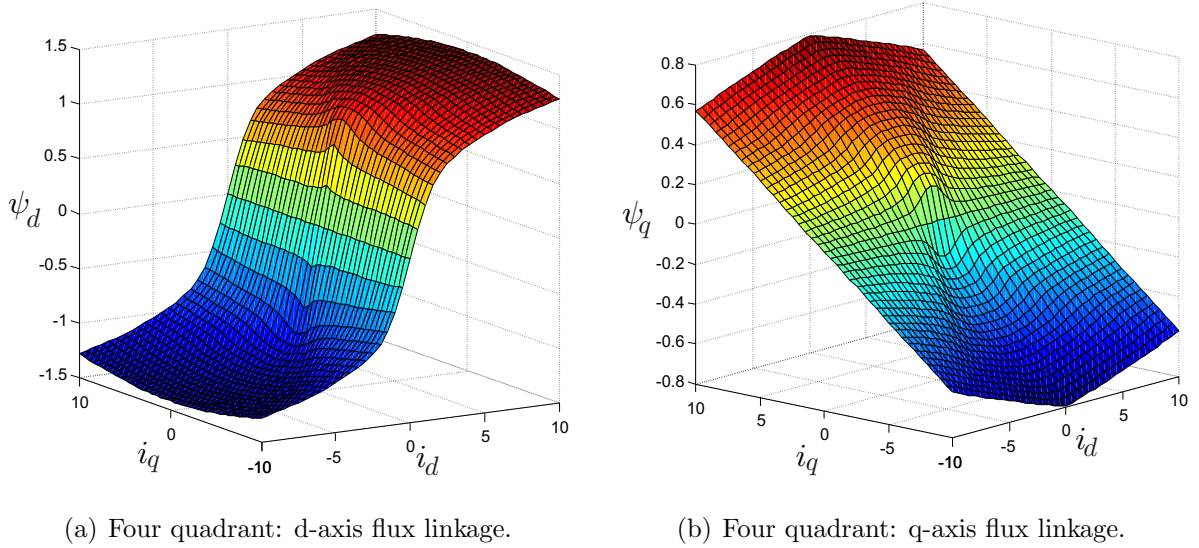


Figure 3.2: FE results: current to flux linkage mapping.

Even though the transformation to the synchronously rotating  $dq$  reference frame should theoretically remove dependencies on  $\theta_r$ , the flux linkages nevertheless remain functions of  $\theta_r$ , e.g. due to stator slot openings. Fig. 3.3 shows the ripple components of the torque,  $\psi_d$  and  $\psi_q$ , expressed in percentage. Also, even though the  $d$ -axis and  $q$ -axis are perpendicular to each other, cross coupling and cross saturation may not be ignored. Therefore  $\psi_d = \psi_d(i_d, i_q, \theta_r)$  and  $\psi_q = \psi_q(i_d, i_q, \theta_r)$ .

The relationship between  $\vec{\psi}_r$  and  $\vec{i}_r$  may be expressed in terms of inductances. Now, the tangential inductance  $L_t$  is defined as the partial derivative of flux linkage with respect to

current  $\frac{\partial \psi}{\partial i}$ , while secant inductance  $L_s$  is defined as flux linkage divided by current  $\frac{\psi}{i}$  [63]. The tangential inductance is useful as in equations (3.1) through (3.3). It is common that the secant inductances are used to write the torque equation as  $T_m = \frac{3p}{2} (L_{ds} - L_{qs}) i_d i_q$ , indicating that the source of the torque is the saliency  $L_{ds} > L_{qs}$ . Taking saturation into account  $L_{ds} \neq L_{dt}$  and  $L_{qs} \neq L_{qt}$ .

More FE results for the fundamental model are shown in Fig. 3.4, with reference to the inductances defined above. Flux linkages, tangential inductances and secant inductances are shown as functions of the modulus  $i_r$ , evaluated along three different axes, namely  $\phi_r = 89.9^\circ$ ,  $\phi_r = 0.1^\circ$  and  $\phi_r = 60^\circ$  (zero current avoided for secant inductance). Here, the differences between the secant and tangential inductances and also the non-linearity due to saturation are visible.

$$\begin{aligned} \frac{d\psi_d}{dt} &= \frac{\partial \psi_d}{\partial i_d} \cdot \frac{di_d}{dt} + \frac{\partial \psi_d}{\partial i_q} \cdot \frac{di_q}{dt} + \frac{\partial \psi_d}{\partial \theta_r} \cdot \frac{d\theta_r}{dt} \\ &= L_{dt} \cdot \frac{di_d}{dt} + M_{dt} \cdot \frac{di_q}{dt} + \frac{\partial \psi_d}{\partial \theta_r} \cdot \omega_r \end{aligned} \quad (3.1)$$

$$\begin{aligned} \frac{d\psi_q}{dt} &= \frac{\partial \psi_q}{\partial i_d} \cdot \frac{di_d}{dt} + \frac{\partial \psi_q}{\partial i_q} \cdot \frac{di_q}{dt} + \frac{\partial \psi_q}{\partial \theta_r} \cdot \frac{d\theta_r}{dt} \\ &= M_{qt} \cdot \frac{di_d}{dt} + L_{qt} \cdot \frac{di_q}{dt} + \frac{\partial \psi_q}{\partial \theta_r} \cdot \omega_r \end{aligned} \quad (3.2)$$

$$M_t = M_{qt} = M_{dt} \quad (3.3)$$

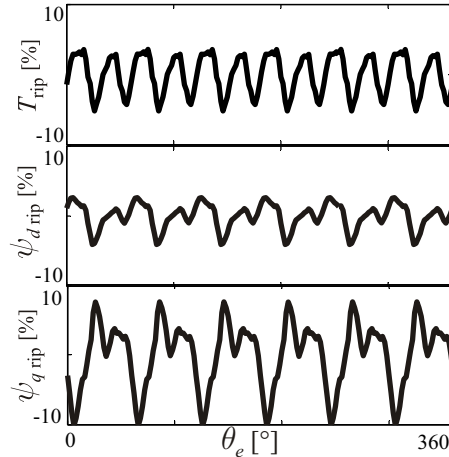


Figure 3.3: Flux linkage and torque ripple for rated conditions.

### 3.1.3 dq model in polar coordinates

The FE results shown in Fig. 3.5 describe the RSM in polar coordinates. For a single rotor position, the only remaining input to the FE program is  $\vec{i}_r$  and the electro-static solution gives  $\vec{\psi}_r$ .  $T_m$  is solved using equation (2.14), and  $\vec{u}_r$  is solved in the steady state using



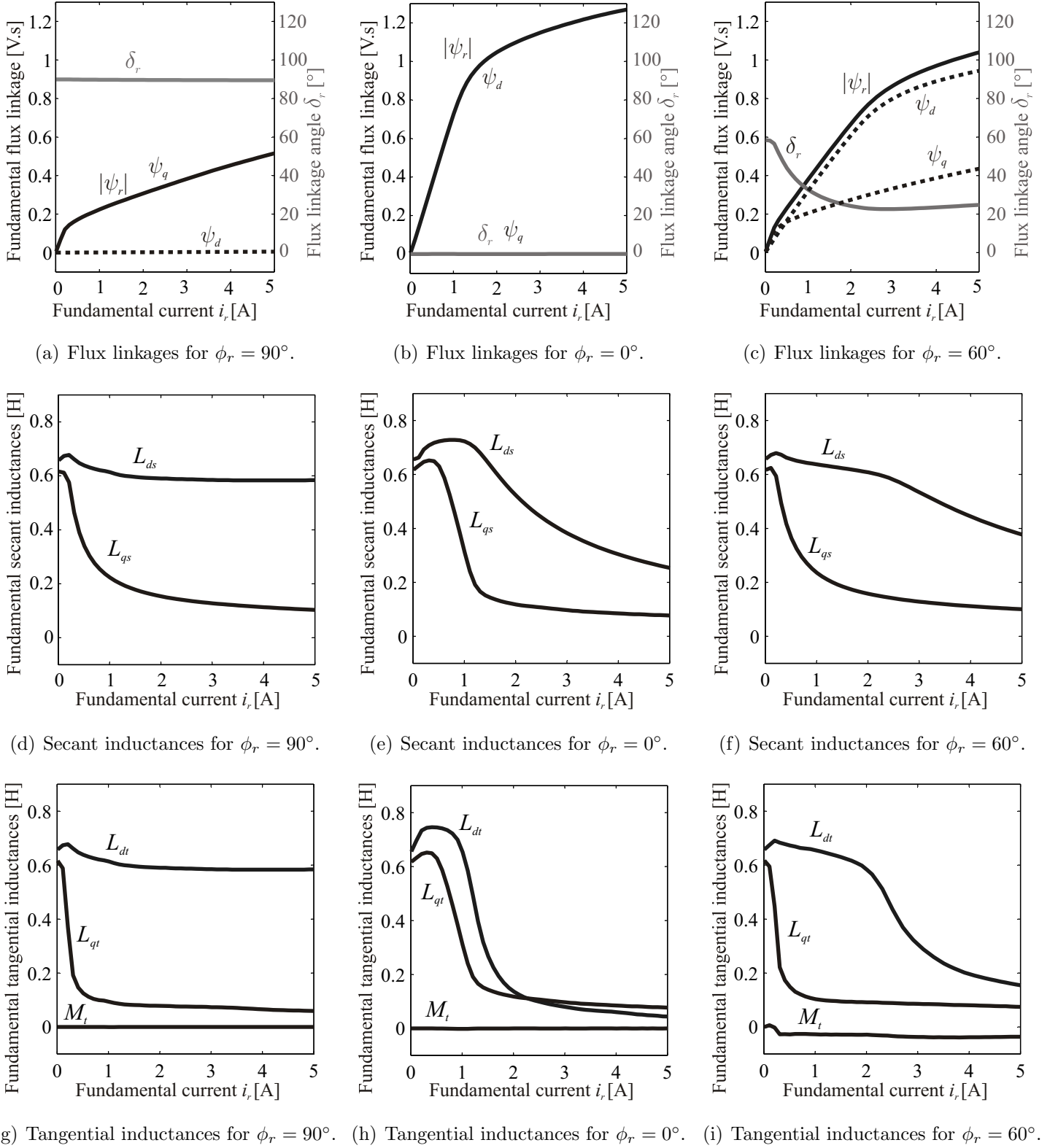


Figure 3.4: FE results: fundamental model in Cartesian coordinates.

(2.12) with  $\omega_r$  as an independent variable. Fig. 3.5(a) shows the input current  $\vec{i}_r$  to the FE program, the outer circle corresponding to the rated current. Fig. 3.5(b) shows the corresponding flux linkage  $\vec{\psi}_r$ , where it can be noted that saturation occurs in the  $d$ -axis

since the ellipses tend closer in this direction. Fig. 3.5(c) shows the torque magnitude  $|T_m|$  with current angle  $\phi_r$ . Filled circles indicate maximum torque per ampere (MTPA) with corresponding MPTA points shown on Figs. 3.5(a), 3.5(b) and 3.5(d). Fig. 3.5(d) shows the voltage evaluated for rated speed using equation (2.12). Considering the voltage limitation  $|\vec{u}_r| < \frac{U_{dc}}{2}$  for sinusoidal PWM, as indicated by the dotted circle, achievable operating conditions are indicated in Fig. 3.5 by solid lines and unachievable operating conditions by dotted lines.

This description of the machine enables one to locate the maximum torque per ampere points simply, and also illustrates the effect of voltage limitation on achievable operating conditions. It is necessary to have this insight before one can design an optimal torque control algorithm for the whole speed range. The example given here is for the RSM, but the ideas are equally applicable to any other synchronous machine that does not contain rotor windings, as shown in [56].

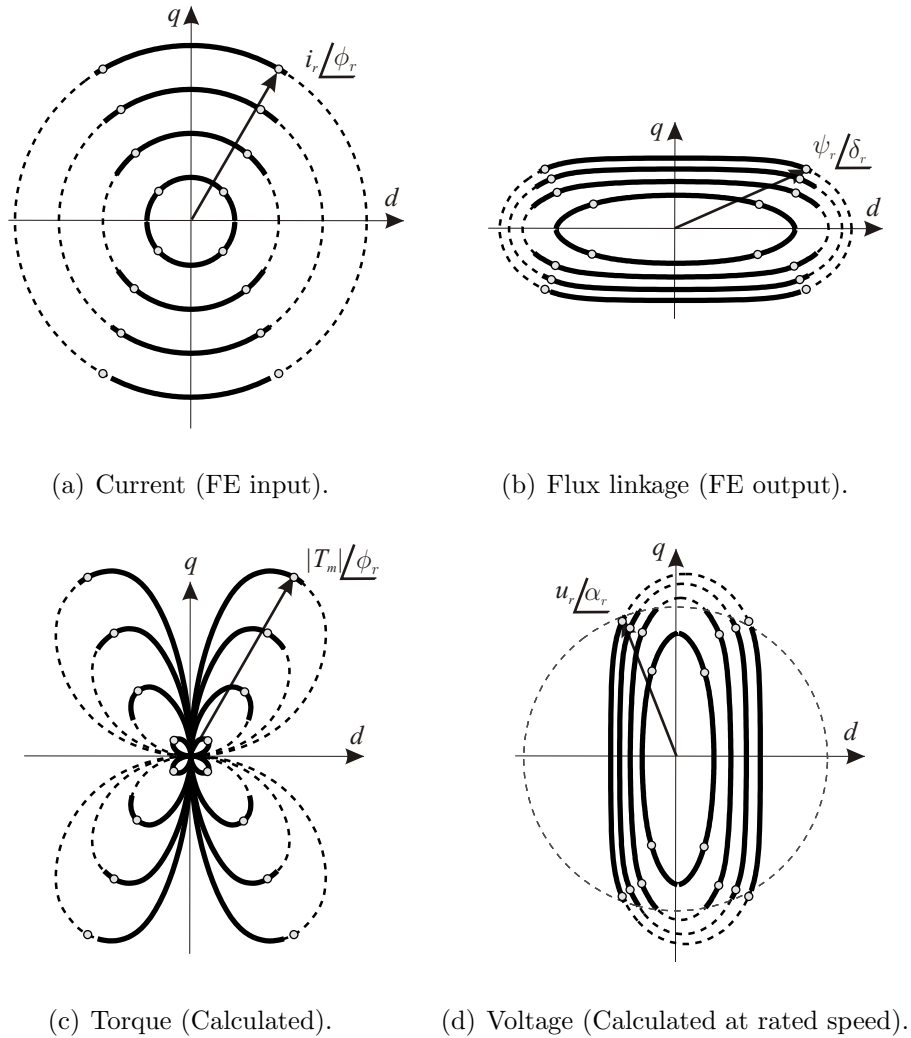


Figure 3.5: FE results: fundamental model in polar coordinates.

Focusing on the speed region below base speed, the curve for the MTPA points on the current plane (i.e. the optimal torque producing locus for the current vector) may be

approximated by a straight line, i.e. constant current angle current control may be used. Choosing a constant current angle corresponding to the MTPA point for the rated current ( $\phi_r = 60^\circ$ ), the loss in torque for non-rated conditions is small, as can be seen in Fig. 3.5(c). Therefore, the FE results of interest, with respect to the control algorithm below base speed, are only those relating to the current angle of  $\phi_r = 60^\circ$ .

### 3.1.4 Rated conditions

Using the results shown in Fig. 3.5, the rated conditions of the machine can be extracted, as shown in the vector diagram of Fig. 3.6. The rated conditions are dependent firstly on the amount of power loss that can be allowed (this machine is self-cooled, using only the rotation of the rotor), i.e. the rated current magnitude is given. Secondly the inverter's voltage limitation comes into play, that determines the rated current angle and consequently the rated flux linkage magnitude and angle, as well as the rated torque and speed. The rated conditions for this specific RSM are summarized in Table. 3.1.

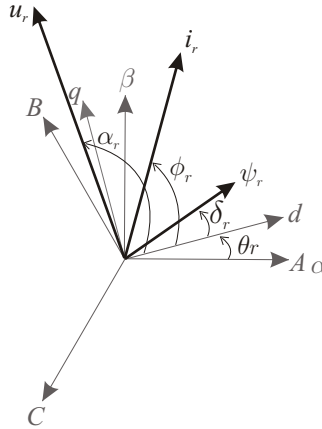


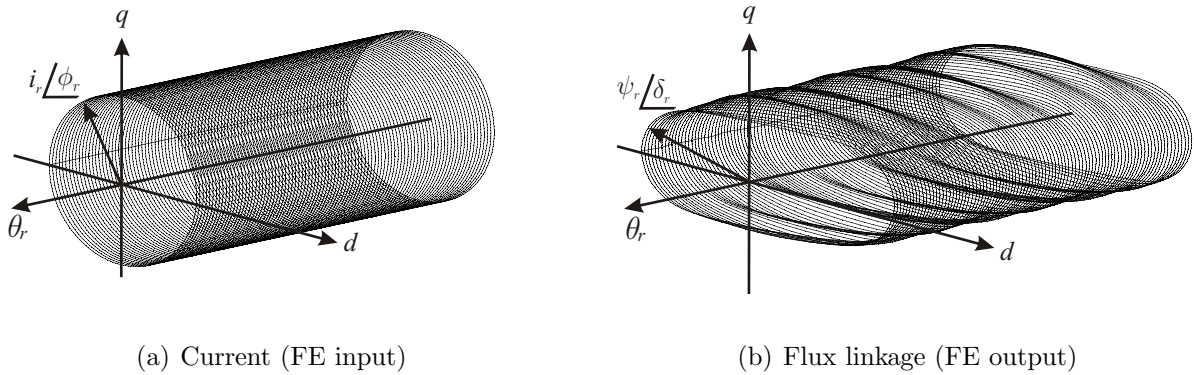
Figure 3.6: Vector diagram of rated conditions.

### 3.1.5 $dq$ model in cylindrical coordinates

Apart from the results shown in Fig. 3.3, all the other results that have been shown were for a single rotor position. Building on the model in the polar coordinates, it is possible to show the parameter variations with varying  $\theta_r$ . Fig. 3.7(a) shows the rated input current vector  $\vec{i}_r$  for a set of rotor positions from 0 to 90 degrees. The resulting flux linkage vector  $\vec{\psi}_r$  is shown in Fig. 3.7(b), where the flux linkage ripple with varying rotor position is clearly visible, especially in the  $q$ -axis. This result implies that there will be torque ripple, and that the flux linkage and subsequently all inductances are also rotor position dependent.

**Table 3.1:** *RSM rated values and related information*

Speed	1500 rpm	Frequency	50 Hz
Pole pairs	2	Power factor	0.63
Voltage	400 V rms l-l	$\alpha_r$	110 °
Current	3.5 A rms	$\phi_r$	60 °
Flux linkage	1 V.s	$\delta_r$	20 °
Reactive power	2425 V.A	Power	1528 W
Torque	10 N.m	DC bus needed	650 V
$R_s$	4.3 $\Omega$		

Figure 3.7: FE results: fundamental model in cylindrical coordinates (variation with  $\theta_r$ ).

## 3.2 Simulation methods

Simulation is a powerful tool: it can verify complicated mathematics and allows one to try out new ideas before executing them practically. The well known and globally recognized simulation tool Matlab Simulink was used at first to create a simulation for the RSM and its control system. Some rapid prototyping systems like D-Space allow one to simulate first on Simulink, and then use the same “code” for the practical experiments. Other systems, that use DSP or micro-processor for example, generally do not have this capability. That means that after the simulation in Simulink has been completed, the ideas have to be re-implemented in ANSI C-code for example. Consequently there will be a loss of time. This section first shows the Matlab Simulink model that was constructed and then discusses an alternative method of simulation that was also used in this work.

### 3.2.1 Simulation with Matlab Simulink

The RSM model with its control system is modelled in Matlab Simulink using standard building blocks (see section B.1 to download the simulation files). The whole system is divided into subsystems for visual and logical clarity. The RSM machine model is presented here starting with an  $ABC$  model, and each time zooms into deeper level until the voltage and torque equations are reached.

Fig. 3.8 shows the RSM's  $ABC$  model that consists of the three-phase voltage inputs as well as the torque load input, the transformation from  $ABC$  to  $\alpha\beta$  for the voltages, the RSM model in  $\alpha\beta$  that gives the output currents as well as the mechanical rotor position and speed as outputs, and finally the transformation from  $\alpha\beta$  to  $ABC$  for the currents. Now we zoom in on the  $\alpha\beta$  model, as shown in Fig. 3.9. This subsystem contains firstly the negative rotation transformation from  $\alpha\beta$  to  $dq$  for the voltages, then the machine model in  $dq$  and then current positive rotation transformation from  $dq$  to  $\alpha\beta$  for the output currents. The triangular block with "p" is the number of pole-pairs: it is needed to obtain the electrical position from the mechanical position, since the electrical position is used for the rotation transformations.

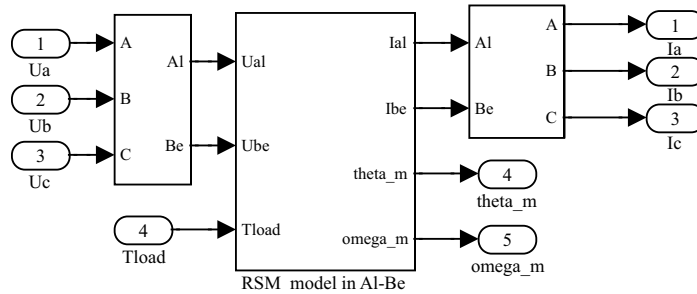


Figure 3.8: Simulink:  $ABC$  model.

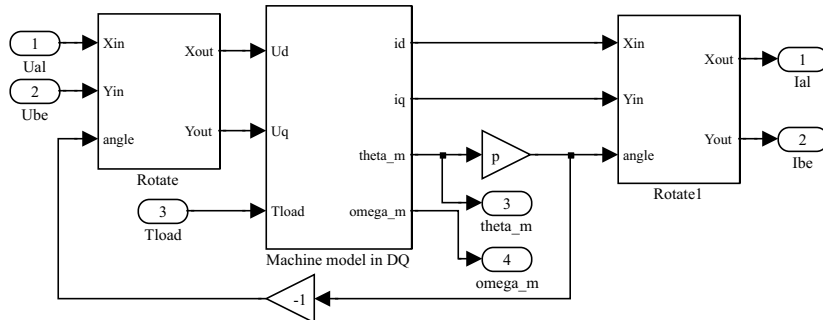


Figure 3.9: Simulink:  $\alpha\beta$  model.

Zooming in on the machine model in  $dq$ , as shown in Fig. 3.10, the subsystem contains firstly an Electrical Model, then an Equivalent Mechanical Model and then a block that converts the speed signal into a position signal (integration), but also takes into account an initial rotor position and converts the position signal into the typical saw-tooth waveform. Focusing on the Electrical Model, as shown in Fig. 3.11, the voltage and torque equations

come into play. The resistive voltage vector and speed voltage vector are first subtracted from the applied  $dq$  input voltage vector, after which only the derivative of the flux linkage vector should remain and can therefore be integrated to obtain the flux linkage vector. Then 2D lookup tables (the inverse LUTs of those obtained from FE analysis) are used to obtain the current vector, and also to calculate the torque, as shown in Fig. 3.12. (See section B.2 to download the Matlab files to create such lookup tables). Note that one should take care with the initial flux linkage vector value, especially if permanent magnets are involved, but for the RSM the initial flux linkage vector value is usually zero.

This method avoids the calculation of inductances completely. All saturation and cross-coupling effects (mutual inductance) are taken into account for any working condition by using 2D LUTs (with 2D interpolation) that are constructed using results from FE analysis. Note that the variation of the flux linkage vector with varying rotor position is not taken into account in the simulation. If this had to be included, 3D LUTs would for example have to be used.

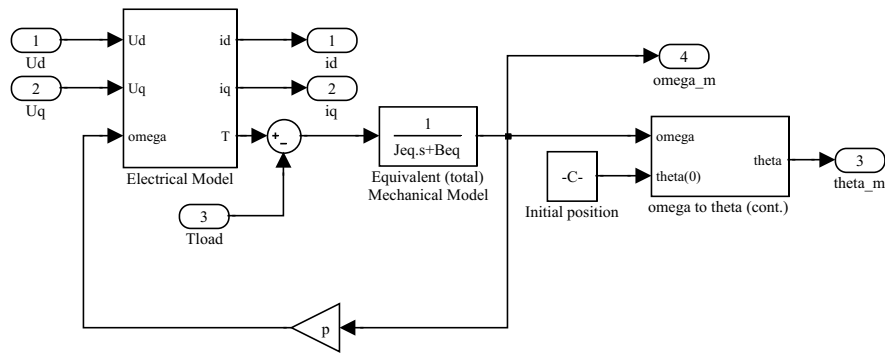


Figure 3.10: Simulink:  $dq$  model.

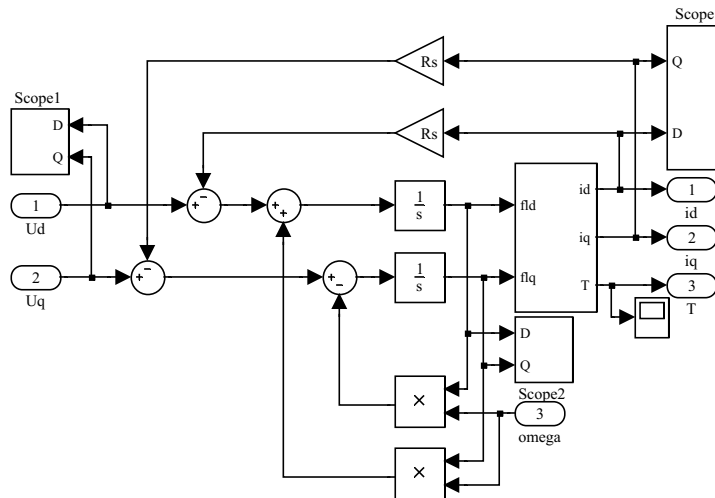


Figure 3.11: Simulink: Electrical model,  $dq$  model expanded.

Zooming out completely, this RSM model can be used with an inverter model, current vector control model, indirect torque controller, and analogue-to-digital and encoder models, as shown in Fig. 3.13, to simulate the entire control system. As previously mentioned, the

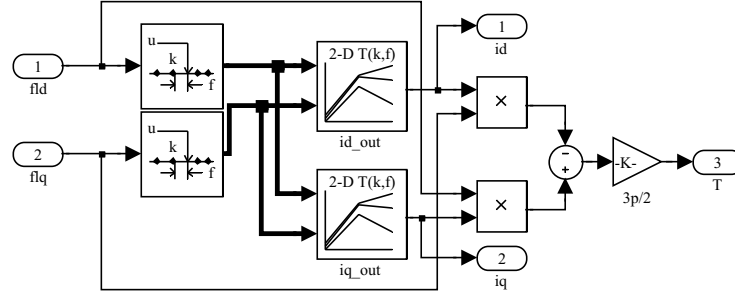


Figure 3.12: Simulink: Inverse 2D LUTs with 2D interpolation.

ideal is to perform the simulations and afterwards just modelled hardware with the actual hardware, so that no work should be repeated. Such systems with an interface between Matlab Simulink and hardware do exist, but are usually too expensive. The wonderful thing about such systems is that Matlab Simulink is a well-known tool, it has a graphical user interface and includes ready-to-use blocks for lookup tables, integration etc. An alternative is to program everything in ANSI C code.

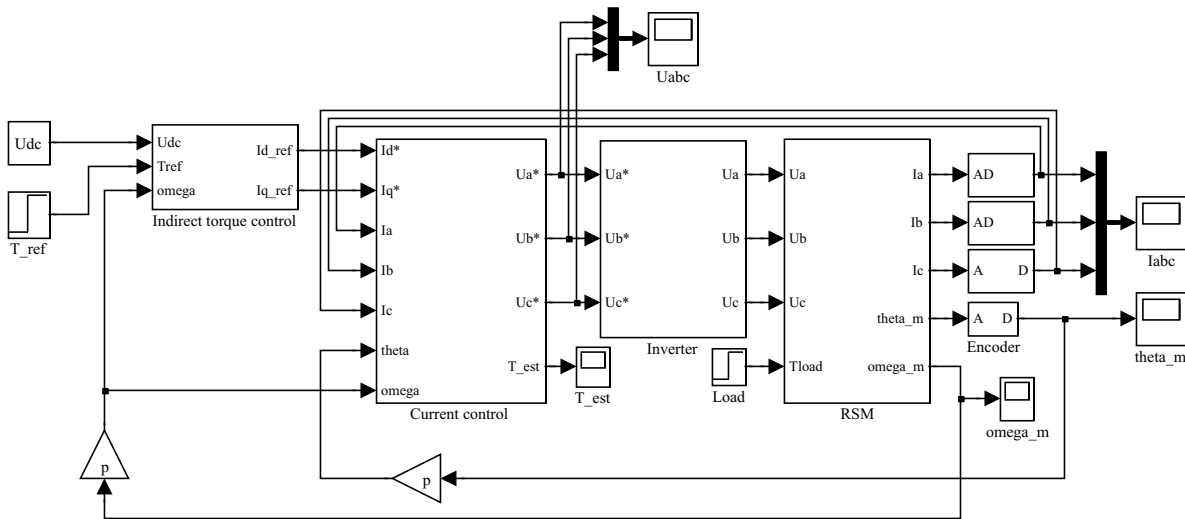


Figure 3.13: Simulink: Indirect torque control.

### 3.2.2 Simulation with Rapid Prototyping System: ANSI C

The University of Wuppertal in Germany developed a rapid prototyping system (RPS), previously known as the "Pentium System" that is described in the introduction of this dissertation. The RPS runs the Linux operating system and the real time applications interface (RTAI) to enable implementation of a real-time control system. All the code is written in ANSI C.

It is desirable to be able to perform simulations and afterwards confirm the results practically. This concept is known as "hardware in the loop systems", and the system with

Matlab Simulink and D-Space is an example thereof. However, the RPS developed at Wuppertal aims to be as cheap and effective as possible and therefore simulation capability is simply added to it in the form of additional C code. In fact, the blocks that are shown for Matlab Simulink here above were simply implemented in ANSI-C code and executed after the control system code had been executed (see section B.4 to download the ANSI-C code). The modular structure is maintained by using separate functions for each block and using pointers where necessary. A prerequisite for such a system is a powerful micro-controller and a lot of memory (a standard feature in modern PCs), as well as a moderate interrupt or sampling frequency (depending on the processing capabilities).

### 3.3 Flux linkages: simulation vs. practical

It is desirable to compare the flux linkage given by the FE program with a practically obtained flux linkage value, i.e. using the actual machine. Since flux linkage is not measured, it has to be estimated or calculated in some way from known and measurable quantities. A simple approach is to measure the stator resistance, control the speed of the load machine (mechanically coupled to the RSM) to have a fairly high and constant value e.g. 1000 rpm, control the current vector of the RSM at a specific working point (this is a steady state method), then use the  $dq$  voltage vector equation 2.12 to calculate the flux linkage vector, i.e. take the commanded voltage vector of the current vector controller (only PI should be used, no decoupling should be used), subtract the resistive voltage and divide by the electrical speed (keeping the imaginary operator in mind), as in equation (3.4).

$$\vec{\psi}_r \approx \frac{\vec{u}_r^* - R_s \vec{i}_r}{j\omega_r} \quad (3.4)$$

In Fig. 3.14 the simulation results (using the RPS) are shown on the left and the practical results are shown on the right. The current vector of the RSM is controlled in each case from zero to rated current (note that the time scale is 1 second, i.e. one experiment lasts 10 seconds and for each point the solution can be regarded as steady state) and for three different current angles namely 90, 0 and 60 degrees respectively. These results can be compared to the flux linkages that were obtained directly from FE analysis in Fig. 3.4. It is clear that the simulation results using the 2D LUTs match exactly the results that were obtained directly from FE analysis, thus validating the method and the simulation.

When comparing the simulation results with the practically obtained results, it is clear that the practically obtained flux linkage contains some kind of HF oscillation that is not present in the simulation: this is the variation with rotor position (remember that this experiment is performed at constant speed) that is not present in the simulation. When comparing Fig. 3.14(a) with Fig. 3.14(b) it is noted that the average value of  $\psi_d$  is not zero in the practical case as opposed to the simulated case. Also, when comparing Fig. 3.14(c) with Fig. 3.14(d) it is noted that the average value of  $\psi_q$  is zero, as in the simulation. By



changing the zero-position (this is the offset for the measured electrical rotor position so that the  $d$ -axis coincides with the  $\alpha$ -axis when the measured electrical rotor position is zero degrees) the average value of the  $\psi_d$  could be set to zero in Fig. 3.14(b), but then the average value of  $\psi_q$  is not zero in Fig. 3.14(d). The reason remains unclear.

One also notices that the shape of  $\psi_d$  in Fig. 3.14(c) compared to that in Fig. 3.14(d) is quite different: the bend of saturation is much clearer in the simulation. When comparing Fig. 3.14(e) with Fig. 3.14(f) it is also clear that the final value of  $\psi_d$  is quite different. It should be noted that there is no dead-time compensation and a constant value of stator resistance is used for the calculation, but these things should not have a big effect, since the experiment is performed at rated speed.

An alternative method is to estimate the flux linkage in the  $\alpha\beta$  reference frame, as shown in Chapter 9, and to transform it to the  $dq$  reference frame using the measured electrical rotor position, but the results are more or less the same. The reason for the difference between values obtained from FE and values obtained in the practical test is still under investigation. It could be that there are real differences between the actual and FE modelled machine.

### 3.4 High frequency $dq$ model

To arrive at a HF model, let us first start with the voltage equation (2.12). Now evaluate this equation for high frequency (HF) signals, i.e. for signals at a frequency that is bounded as in (3.5), where  $f_s$  is the sampling frequency and  $\omega_r$  is the maximum operating fundamental frequency [32]. Usually a high frequency between 400 Hz and 2000 Hz is used. At such a high frequency, the resistive term and the speed voltage term in 2.12 fall away, due to their small magnitudes compared to the magnitude of the derivative of the flux linkage term. We are therefore left with the terms described by (3.1) through (3.3), i.e. the HF model of the machine may be given by equations (3.6) and (3.7). Furthermore, at relatively low rotor speed, the HF model reduces to (3.8) and (3.9).

It has been found that the tangential inductances in the HF model are different to the tangential inductances in the fundamental model [32], and the HF model is therefore expressed as in (3.6) through (3.7), with the HF subscripts, to emphasize this idea. In [36], the authors emphasize that mutual inductance plays a role, however they do not make the distinction between HF model inductances and fundamental model inductances. The authors in [64] have also suggested that the HF behaviour cannot be predicted accurately using the standard fundamental model and that one should include core losses to improve the simulation results.

$$2\omega_r < \omega_{HF} < \frac{2\pi f_s - 2\omega_r}{2} \quad (3.5)$$

$$u_d(\omega_{HF}) \approx L_{dtHF} \frac{di_d}{dt} + M_{tHF} \frac{di_q}{dt} + \frac{\partial \psi_d}{\partial \theta_r} \cdot \omega_r \quad (3.6)$$

$$u_q(\omega_{HF}) \approx L_{qtHF} \frac{di_q}{dt} + M_{tHF} \frac{di_d}{dt} + \frac{\partial \psi_q}{\partial \theta_r} \cdot \omega_r \quad (3.7)$$

$$u_d(\omega_{HF})|_{\omega_r \approx 0} \approx L_{dtHF} \frac{di_d}{dt} + M_{tHF} \frac{di_q}{dt} \quad (3.8)$$

$$u_q(\omega_{HF})|_{\omega_r \approx 0} \approx L_{qtHF} \frac{di_q}{dt} + M_{tHF} \frac{di_d}{dt} \quad (3.9)$$

### 3.4.1 Practical measurements for HF parameters

The values for  $L_{dtHF}$ ,  $L_{qtHF}$  and  $M_{tHF}$  are dependent on the load operating condition of the RSM, and have been calculated in an experimental setup: using a RSM with a locked rotor, the fundamental current was controlled to specified values, an additional HF voltage command was added to the current controller output (indicated by the  $+ =$  sign in Fig. 3.15) and the measured HF currents were used to calculate  $L_{dtHF}$ ,  $L_{qtHF}$  and  $M_{tHF}$ . In Fig. 3.15 the amplitudes of the HF currents,  $|i_{dHF}|$  and  $|i_{qHF}|$ , are shown as functions of the fundamental current  $i_r$ . Three cases for fundamental current are evaluated: along the  $q$ -axis, along the  $d$ -axis and along the  $\phi = 60^\circ$  axis; the first two being only of theoretical interest and the last being of practical interest. Also note that pulsating HF voltages are applied, either in the  $d$ -axis or the  $q$ -axis.

Fig. 3.15(a) shows that increasing  $i_r$  with  $\phi = 90^\circ$  causes saturation in the  $q$ -axis, such that  $L_{qtHF}$  decreases and therefore  $|i_{qHF}|$  increases. There is a small amount of cross-coupling since there is a measurable  $|i_{dHF}|$ , however it is close to the ideal zero. Fig. 3.15(d) shows that increased saturation in the  $q$ -axis does not affect  $|i_{dHF}|$  much. There is a small amount of cross-coupling since there is measurable  $|i_{qHF}|$ , however it is close to the ideal zero.

Fig. 3.15(e) shows that increasing  $i_r$  with  $\phi = 0^\circ$  causes saturation in the  $d$ -axis, such that  $L_{dtHF}$  decreases and therefore  $|i_{dHF}|$  increases. There is a small amount of cross-coupling since there is measurable  $|i_{qHF}|$ , however it is close to the ideal zero. Fig. 3.15(b) shows that increased saturation in the  $d$ -axis affects  $|i_{qHF}|$ , i.e. cross-saturation causes a decrease in  $L_{qtHF}$  and therefore an increase in  $|i_{qHF}|$ . There is a small amount of cross-coupling since there is a measurable  $|i_{dHF}|$ , which increases as the saturation in the  $d$ -axis increases.

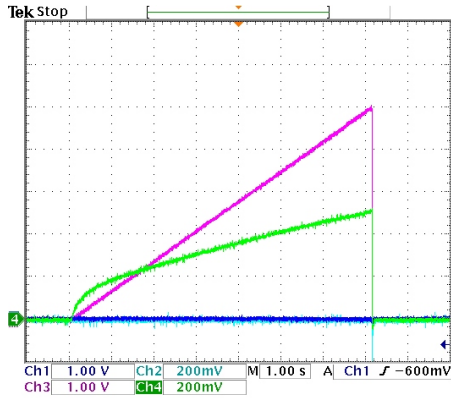
Although these results are interesting, they are not of much practical use, since the RSM will never be controlled along these axes. Fig. 3.15(c) shows that increasing  $i_r$  with  $\phi = 60^\circ$  causes saturation in the  $q$ -axis, such that  $L_{qtHF}$  decreases and therefore  $|i_{qHF}|$  increases. There is a small amount of cross-coupling since there is measurable  $|i_{dHF}|$ , however it is close to the ideal zero. Fig. 3.15(f) shows that increasing  $i_r$  with  $\phi = 60^\circ$  causes saturation in the  $d$ -axis, such that  $L_{dtHF}$  decreases and therefore  $|i_{dHF}|$  increases. There is a large amount of cross-coupling since there is comparable  $|i_{qHF}|$ . Here it is also noted that as  $i_r$  increases,  $L_{qtHF}$  decreases and therefore  $|i_{qHF}|$  increases.

Using the measured data of the HF currents, the effective HF inductances may be calculated with very little approximation. For example, as noted in Fig. 3.15(c), the effect of mutual inductance is minimal and therefore using the data represented by this figure with (3.7),  $|u_{qHF}| \approx L_{qtHF}\omega_{HF}|i_{qHF}|$ . Then, with  $L_{qtHF}$  known, the data represented by Fig. 3.15(f) may be used to find the mutual inductance with (3.7),  $0 \approx L_{qtHF}|i_{qHF}| + M_{tHF}|i_{dHF}|$ . Then finally, still using the data represented by Fig. 3.15(f), now with (3.6) and with  $L_{qtHF}$  and  $M_{tHF}$  known,  $L_{dtHF}$  may be calculated. These are the inductances that come into play for the sensorless position estimation using HF carrier injection. The significance of these results for rotor position estimation based on HF signal injection is explained in chapter 9.

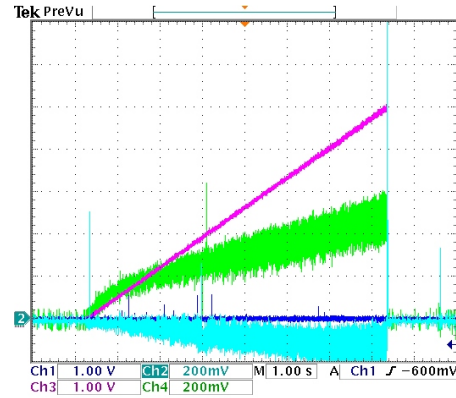
### 3.4.2 Simulation results for HF parameters

Using the Matlab Simulink model, the experiment explained above was repeated in simulation and the results are shown in Fig. 3.16. Comparing these results with the results in Figs. 3.15 and 3.4, it is clear that the simulation shows that the HF inductances are the same as the fundamental model inductances, however from the practical measurement, the HF inductances are different to the fundamental model inductances. This discrepancy remains unsolved, but the authors believe that the FE program is not able to describe the combined fundamental and HF behaviour of the machine accurately, since the flux paths of fundamental flux linkage and HF flux linkage are not the same. At least by doing the simulation, the method of inductance calculation was verified.

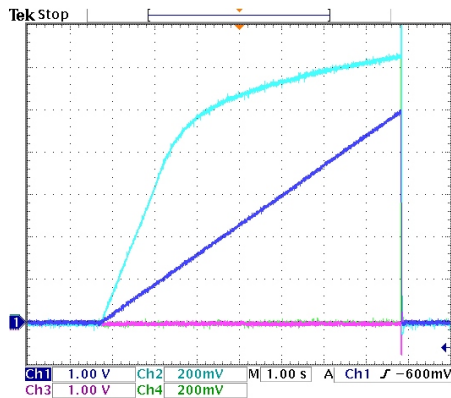
Ch1	$i_d$	1	A/div
Ch2	$\psi_d$	0.2	V.s/div
Ch3	$i_q$	1	A/div
Ch4	$\psi_q$	0.2	V.s/div
Time	$t$	1	s/div



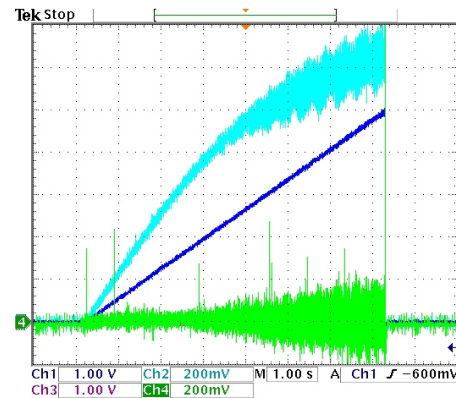
(a) Zero to rated current for  $\phi_r = 90^\circ$ , simulation.



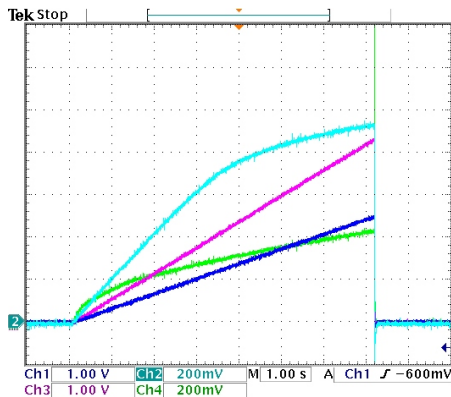
(b) Zero to rated current for  $\phi_r = 90^\circ$ , practical.



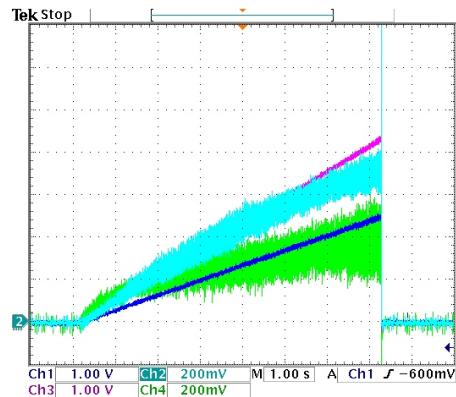
(c) Zero to rated current for  $\phi_r = 0^\circ$ , simulation.



(d) Zero to rated current for  $\phi_r = 0^\circ$ , practical.

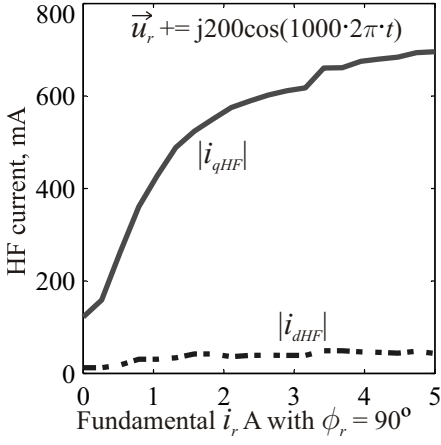


(e) Zero to rated current for  $\phi_r = 60^\circ$ , simulation.

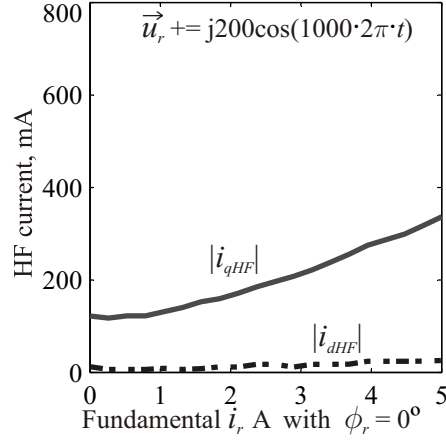


(f) Zero to rated current for  $\phi_r = 60^\circ$ , practical.

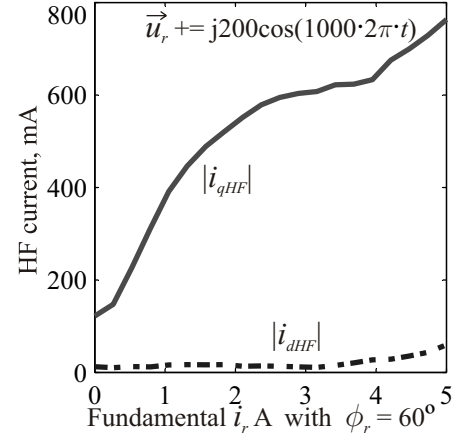
Figure 3.14: Fundamental model: simulation vs. practical results at rated speed.



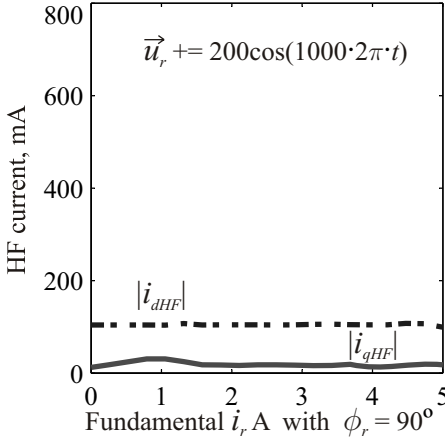
(a)  $u_{qHF}$  and  $i_q$



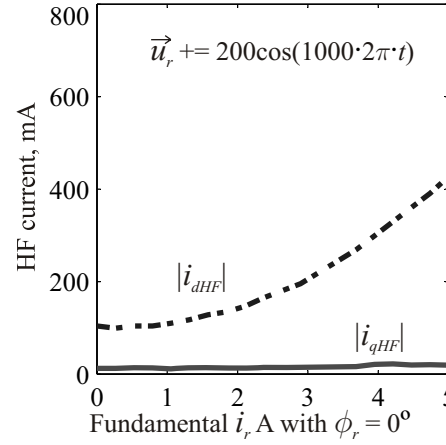
(b)  $u_{qHF}$  and  $i_d$



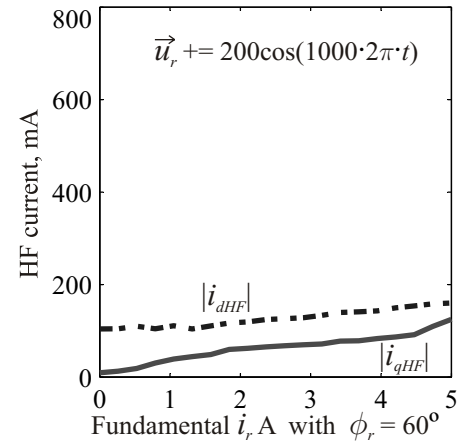
(c)  $u_{qHF}$  and  $i_r$  with  $\phi_r = 60^\circ$



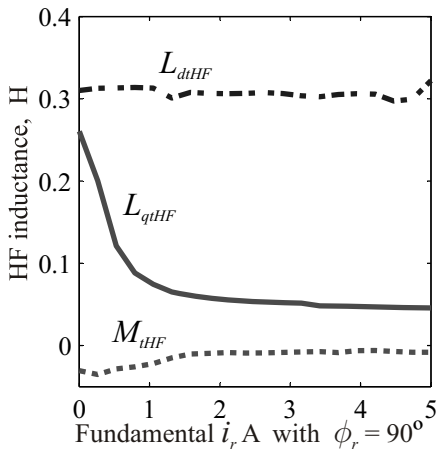
(d)  $u_{dHF}$  and  $i_q$



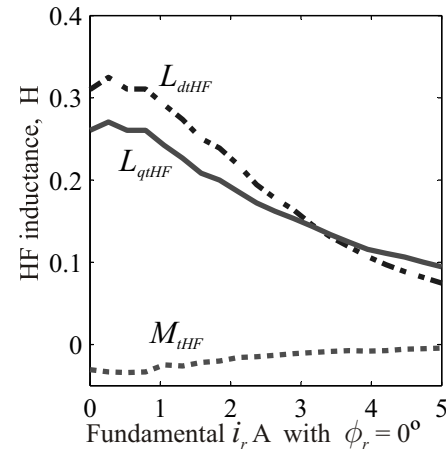
(e)  $u_{dHF}$  and  $i_d$



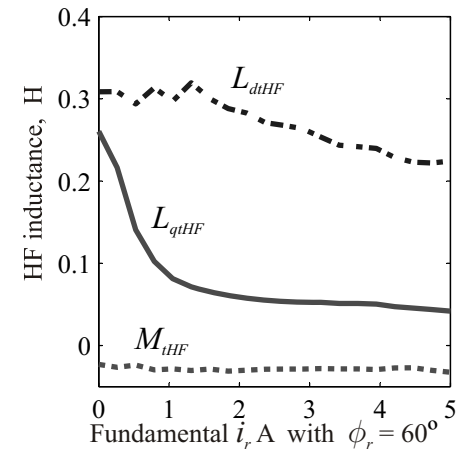
(f)  $u_{dHF}$  and  $i_r$  with  $\phi_r = 60^\circ$



(g) Effective HF inductances with  $i_q$

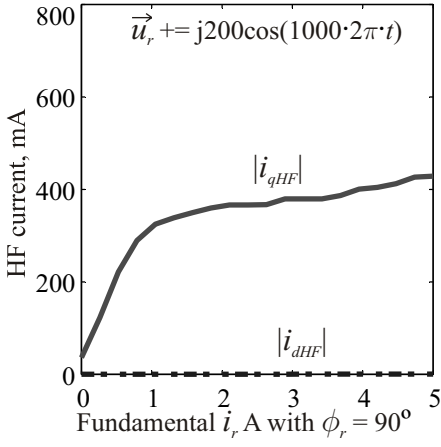


(h) Effective HF inductances with  $i_d$

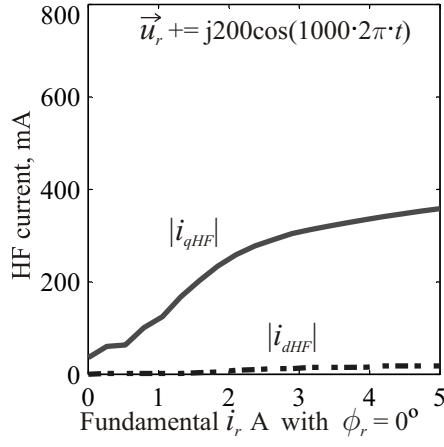


(i) Effective HF inductances with  $i_r$  and  $\phi_r = 60^\circ$

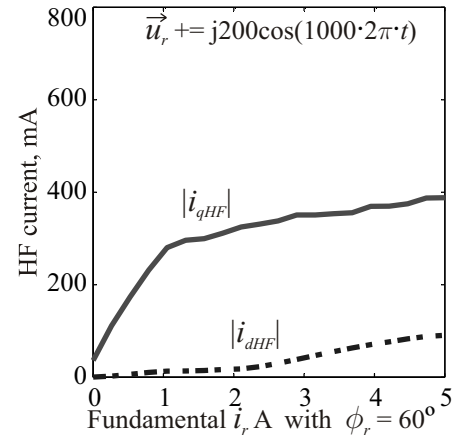
Figure 3.15: Calculated HF inductances from measured data.



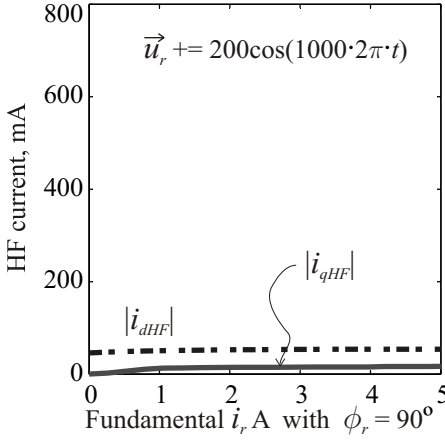
(a)  $u_{qHF}$  and  $i_q$



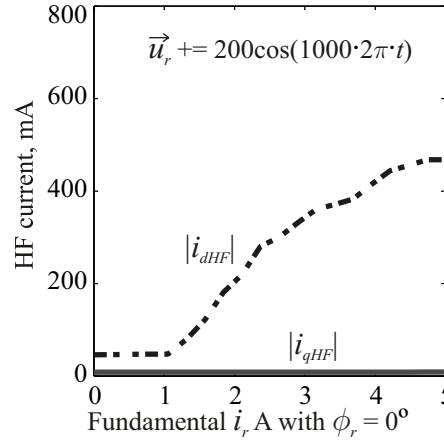
(b)  $u_{qHF}$  and  $i_d$



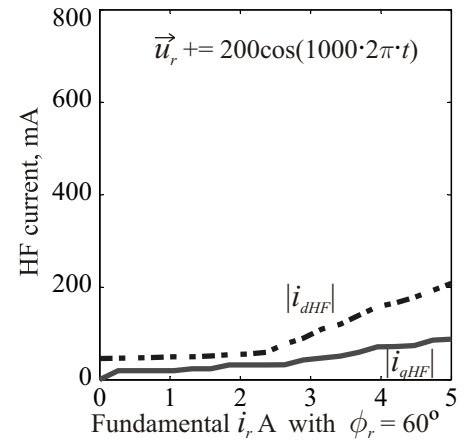
(c)  $u_{qHF}$  and  $i_r$  with  $\phi_r = 60^\circ$



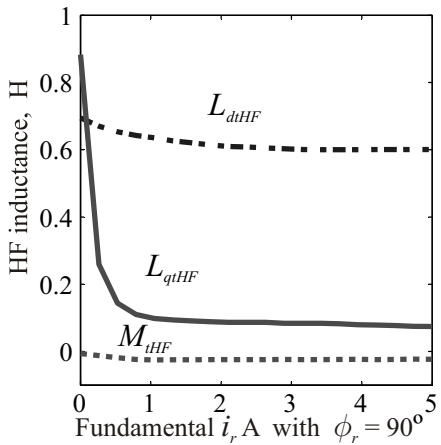
(d)  $u_{dHF}$  and  $i_q$



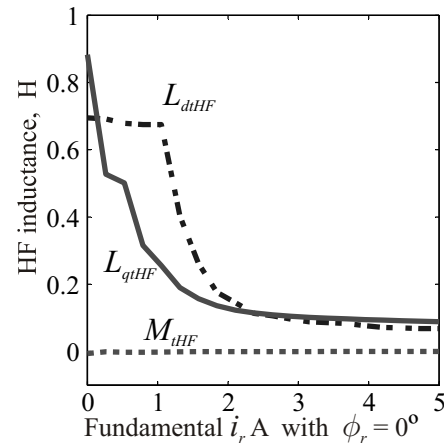
(e)  $u_{dHF}$  and  $i_d$



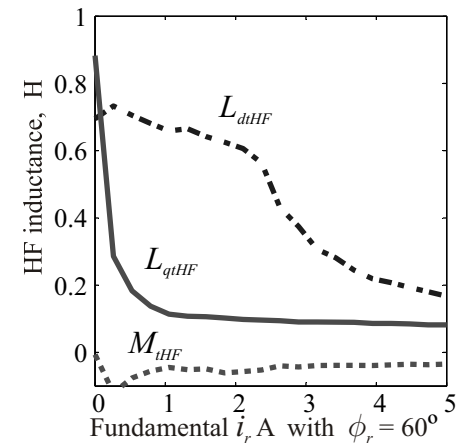
(f)  $u_{dHF}$  and  $i_r$  with  $\phi_r = 60^\circ$



(g) Effective HF inductances with  $i_q$



(h) Effective HF inductances with  $i_d$



(i) Effective HF inductances with  $i_r$  and  $\phi_r = 60^\circ$

Figure 3.16: Calculated HF inductances from simulated data.

# Chapter 4

## Field Orientated Control

In this chapter a quick overview for the chapters that follow is provided. Firstly a motivation on the choice of Field Oriented Control (FOC) over Direct Torque Control (DTC) is given. Then a cascaded control structure is discussed, to provide a reference structure for the chapters that follow.

### 4.1 Field Orientated Control vs. Direct Torque Control

Field Oriented Control (FOC) comprises of closed loop current vector control through open loop voltage vector control. The three-phase stator currents are measured, and can therefore be used for feedback, thereby closing the current control loop. The three-phase voltages are usually not measured in a standard drive system, since it is costly. The three-phase voltages are applied to the electrical machine using a voltage source inverter (VSI), i.e. the DC bus voltage is converted into three-phase AC line voltages using pulse width modulation (PWM). The switching times in one switching period (giving the pulse width) for the pair of transistors in an inverter leg are calculated by taking the voltage reference for that leg and also considering the DC bus voltage (this is usually measured) and the switching period length (this is usually a fixed amount of time).

Many advances on the way that current vector control and PWM should be done, have been made in the last 20 years [65, 66, 67, 68, 69, 70, 71, 72, 73, 74]. It is now possible to have very good dynamic current vector control and use the full capacity of the DC bus voltage. Current control is most often implemented in a reference frame that rotates synchronously with the rotor, i.e. the rotor position is needed. To obtain the rotor position it could either be measured (using an expensive and fragile sensor like an encoder or a resolver) or estimated (based on the fundamental frequency model, the high frequency model, or both at the same time). In the case of the rotor position being estimated, it is known as “position sensorless control”.

Direct torque control (DTC) is based on the estimation of the flux linkage vector and the torque using the measured three-phase currents and the estimated three-phase voltages

(based on switching times and the DC bus voltage), i.e. the estimation of the flux linkage vector and the torque is based on the fundamental frequency model of the machine. Comparing the estimated flux linkage magnitude and torque to the reference flux linkage magnitude and torque, a table is used to give the switching times for the inverter pairs in the three legs of a standard inverter. Theoretically DTC does not need the information of rotor position, however the estimation process based on the fundamental frequency model fails at zero speed and then the control scheme cannot work. Also, at startup the rotor position is needed in the estimation process.

Many advances on the way that the flux linkage and torque estimation should be done, and the way that issues at startup and zero speed should be dealt with, have been made in the last 20 years [38, 39, 40, 7, 41, 42, 43, 44]. The DTC method is popular, since it is known for a very fast torque response and promises to be “position sensorless”.

Many researchers have compared the two methods showing the positives and negatives of each scheme. In this thesis the field oriented control (FOC) structure is used and it is shown as part of a cascaded control structure in the next section.

## 4.2 Cascaded control structure

A very popular control structure is the cascaded type of structure shown in Fig. 4.1. The most inner core is the voltage vector control, which is open loop since the actual voltage is neither measured nor estimated and is not used for feedback. The voltage vector reference is given by a current vector controller, which is closed loop since the three-phase current is measured and used for feedback. The current vector control needs the rotor position and speed information if it is implemented in the synchronously rotating reference frame; therefore the rotor position must be measured or estimated, and the speed is always estimated either from the rotor position measurement or as part of the rotor position estimation.

The current vector reference in the synchronously rotating reference frame is given by the torque controller. The torque control is open loop, since the actual torque is neither measured nor estimated and is not used for feedback. In some control schemes the actual torque is estimated and could be used to try to reduce the torque ripple, but this is not the case in this thesis. The current vector reference command is given based only on the torque reference (command). In fact, it becomes more complicated when the torque needs to be controlled in the high speed or “flux weakening” region: the current vector reference must then be selected by taking the reference torque, the flux linkage magnitude, the DC bus voltage and the rotor speed into account. Since flux linkage is not measured, it must be estimated.

The torque command is given by a speed controller. In some applications like traction, the speed controller is usually human. E.g. the train driver wants to reach a certain speed and gives a high torque command until that speed has been reached more or less, and then reduces the torque command to a level that keeps his reference speed. In a way this is



closed loop speed control, since the human uses his eyes to sense the speed. In some other applications, e.g. a conveyer belt, the speed controller is digital and could be very advanced. In that case, the speed control is closed loop, since the speed is estimated from the measured or estimation rotor position. In some other applications, e.g. in manufacturing, it might also be necessary to have position control. A position control loop might be added around the speed control loop, or other methods like sliding-mode control might be used.

The scope of the work presented in this thesis is limited to the voltage vector, current vector, torque and speed control, as well as the rotor position, speed and flux linkage vector estimation. Position control is not considered in this work, although it is a very interesting topic. Fig. 4.1 shows the cascaded control structure, and the following chapters zoom in on the various parts. Here the block “ $H(s)$ ” is the transfer function of the speed controller, which could be a PI controller for example. The block “ $f$ ” is a function that is used to calculate the maximum flux linkage magnitude that can be sustained for the given DC bus voltage and rotor speed. The block “2D LUTs” is a set of two-dimensional lookup tables that gives a current vector reference in the synchronously rotating reference frame that will result in maximum torque ampere or effective field weakening. The block “ $C(s)$ ” is the transfer function of the current vector controller. This could be a PI controller with integrator anti-windup and speed voltage decoupling, in which case a flux linkage vector estimate and the electrical rotor speed are also necessary as inputs to that control block.

The blocks with  $e^{j\theta_r}$  and  $e^{-j\theta_r}$  are the forward and reverse transformations between the stationary and synchronously rotating reference frames, and they use the electrical rotor position  $\theta_r$  as one of the inputs. In this figure it is shown that the rotor position is measured (the details of mechanical to electrical rotor position conversion and the zero position are omitted). And from the position measurement the rotor speed is estimated in the block “ $W(s)$ ”. The circle with “M3” represents the three-phase electrical machine. “PWM” is the pulse width modulator block for the voltage vector control and the only remaining block represents the inverter.

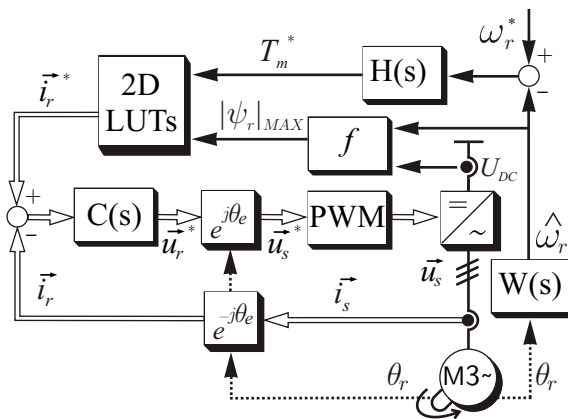


Figure 4.1: Cascaded control structure.

# Chapter 5

## Voltage vector control

The most inner loop of machine control is voltage control. This chapter gives a very brief overview and an implementation example of voltage synthesis for a three-phase two-level inverter using a microcontroller or digital signal processing (DSP) device and a FPGA to generate the inverter switching signals.

### 5.1 Pulse width modulation

For field oriented control (FOC) of a three-phase machine, the voltage reference in the  $ABC$  reference frame is commonly synthesized by pulse width modulation (PWM). There exist many PWM schemes and the goals are to obtain maximum use of the DC bus voltage, to reduce switching losses, to extend the linear range of voltage synthesis, to reduce computational effort and to ease implementation [65, 67, 68, 69, 70, 71, 72]. Due to non-linear load dependent inverter effects, additional effort is usually required to achieve a better linear response [73].

The basic method of PWM is referred to as the sub-oscillation method [70] or the triangle comparison method [68] or the sine-triangle method [67], and with it a maximum balanced three phase voltage magnitude of  $\frac{U_{DC}}{2}$  may be obtained, where  $U_{DC}$  is the DC bus voltage. For each phase, the voltage reference is normalized with respect to the DC bus voltage as well as a counter value, and is then compared to the counter in real time. If the voltage reference is larger than the counter value, the top switch (IGBT or MOSFET) in the inverter leg for that phase is switched on; if the voltage reference is smaller than the counter value, the bottom switch is switched on. Deadtime between the switching states is introduced to prevent both switches from conducting simultaneously, which would cause the DC bus to short circuit. Deadtime has a prominent effect when voltage references are small, and deadtime compensation methods are used to counter this effect.

Space vector pulse width modulation (SVPWM) allows an increase of 15 percent in the maximum voltage magnitude, and a reduction of switching losses (depending on the specific method). SVPWM may be implemented easily by changing the three-phase voltage references before comparing them to the counter value [67], or in many other ways. Over-

modulation techniques also exist, but this is out of the scope of this thesis.

As an implementation example, a rapid prototyping system (RPS) developed at the Electrical Machines and Drives (EMAD) Laboratory, University of Wuppertal in Germany was used. The PWM card has a 10 bit counter, i.e. it counts from 0 to 1023, generates an interrupt, then counts down to 0, generates another interrupt and the process repeats. The interrupt invokes an interrupt service routine (ISR), in which the voltage references are calculated. The PWM card also includes the deadtime.

In the ISR, the voltage reference magnitude in the  $\alpha\beta$  reference frame is first limited to the maximum value that SVPWM offers ( $0.577 \cdot U_{DC}$ ), keeping the voltage angle and setting a saturation flag high when the limit has been reached (the saturation flag is used by the current vector controller to prevent integrator windup, see chapter 6). The voltage reference in  $\alpha\beta$  is then transformed into a voltage reference in  $ABC$ . Maximum and minimum instantaneous values are then found and the  $ABC$  reference is modified so that SVPWM results. The voltage reference is then normalized by  $\frac{U_{DC}}{2}$ , the number one is added, the counter value is normalised by half of the counter's maximum value (in this case a 10 bit counter is used), and finally it is casted into an integer value, which may be compared with the counter, as shown in Fig. 5.1. The counter values are written to addresses on the PWM card each time the interrupt occurs.

The diagram in Fig. 5.1 illustrates the voltage control loop (it is an open loop voltage control), indicating the software and hardware parts. The correct functioning of the voltage control has been tested in the lab by giving various stationary voltage references and measuring the actual phase-to-phase voltages. Deadtime at the inverter input signals is also verified, as shown in Fig. 5.2 and it should be checked for each phase. Finally, the voltage references in  $ABC$  before and after the SVPWM adjustment are shown in Fig. 5.3. It is clear that the line-to-line voltage reference is larger in the case of the modified references. In this thesis there is no consideration of dead-time compensation or other non-linear inverter behaviour.

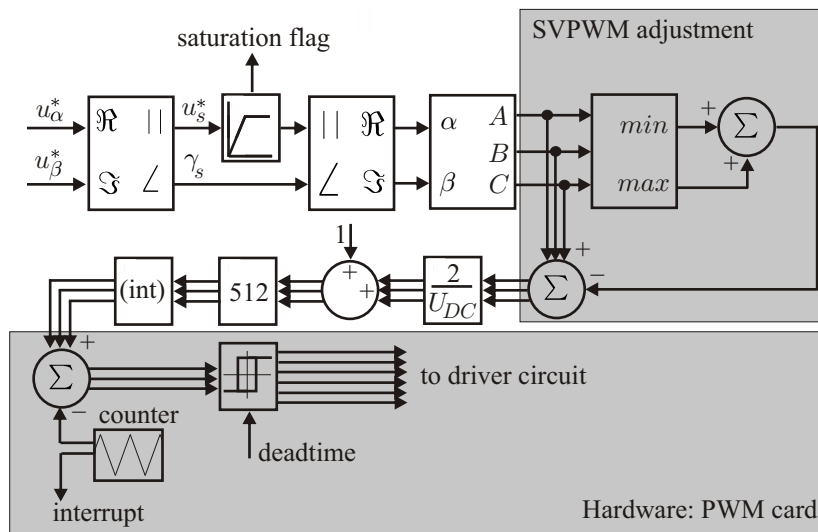
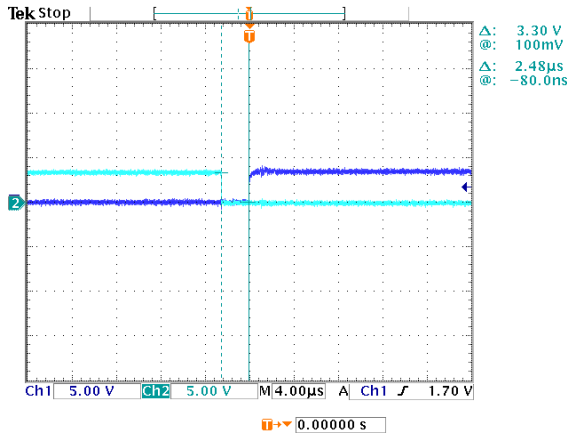


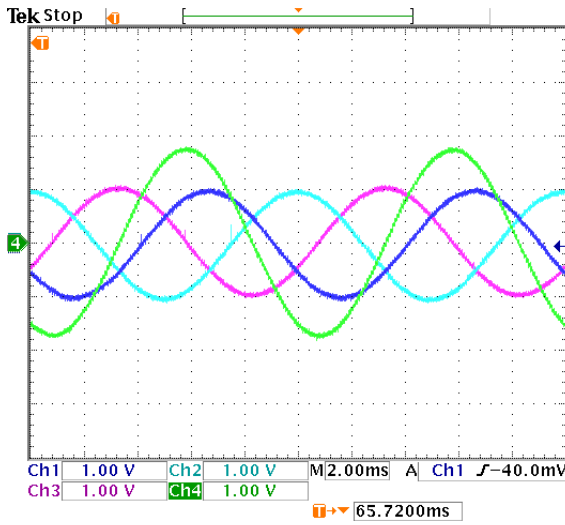
Figure 5.1: Voltage vector control using PWM.



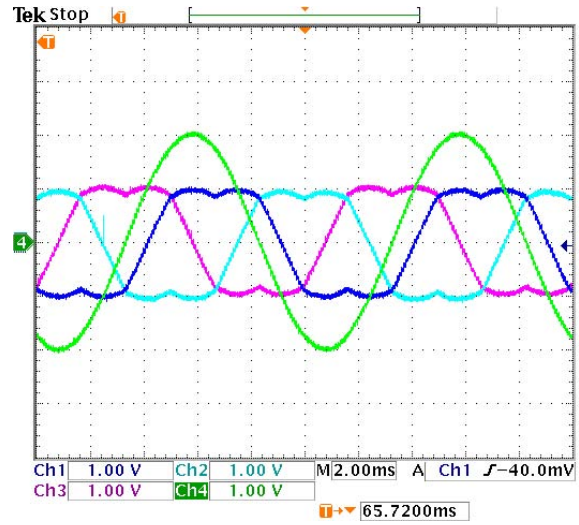
Ch1	$A_{TOP}$	5	V/div
Ch2	$A_{BOT}$	5	V/div
Time	$t$	4	$\mu\text{s}/\text{div}$

Figure 5.2: Dead-time measurement.

Ch1	$\frac{u_A^*}{0.5 \cdot U_{DC}}$	1	const/div
Ch2	$\frac{u_B^*}{0.5 \cdot U_{DC}}$	1	const/div
Ch3	$\frac{u_C^*}{0.5 \cdot U_{DC}}$	1	const/div
Ch4	$\frac{u_{AB}^*}{0.5 \cdot U_{DC}}$	1	const/div
Time	$t$	2	ms/div



(a) Sinusoidal PWM reference.



(b) Modified Sinusoidal PWM reference.

Figure 5.3: Sinusoidal vs. modified PWM references.

# Chapter 6

## Current vector control

The torque of a machine is the cross product of the airgap flux linkage vector with the magnetizing current vector. The ultimate goal is to have dynamic torque control with a possible reduction in the natural torque ripple (i.e. the torque ripple due to the inherent machine design). The airgap flux linkage is a function of magnetizing current, or vice-versa. To control the torque indirectly, one should control the airgap flux linkage, or the magnetizing current, or a combination. Since the current is a measurable quantity (at least the terminal current), it is most common that the current is controlled. In any case, this control strategy is known as field orientated control (FOC), and it is popular, because it can be used with space vector pulse width modulation (SVPWM), which was introduced in chapter 5. Direct torque control (DTC) using switching tables to select the switching states of the inverter is an alternative method, and will be further discussed in chapter 7.

This chapter proposes a control structure to control the current vector effectively. A PI controller with integrator anti-windup and feed-forward speed voltage decoupling is suggested. Simulation and practical results are shown.

### 6.1 PI current vector controller for RSM

The current vector reference is given in the  $dq$  reference frame, as in  $\vec{i}_r^*$ . To get the actual current vector in the  $dq$  reference frame  $\vec{i}_r$ , the current must first be measured in the  $ABC$  reference frame, then transformed to the  $\alpha\beta$  reference frame as in  $\vec{i}_s$  and then transformed to the  $dq$  reference frame using the electrical rotor position  $\theta_r$ , as in equation (6.1) The current error vector can then be calculated as in (6.2).

A vector PI controller is now used to obtain a control voltage vector that will force the current to the reference current, but it is assisted by a feed-forward speed voltage decoupling and the integral part of the PI controller is protected against windup. Firstly the flux linkage vector  $\vec{\psi}_r$  is estimated using 2D lookup tables (LUTs) with 2D interpolation that is obtained from FE analysis. This estimated flux linkage vector is then multiplied by  $j\omega_r$  to obtain the estimated speed voltage term. The speed voltage term is added to the output of the PI controller, so that the PI controller only needs to take care of the resistive voltage term and

the derivative of the flux linkage term, see equation (2.12).

Now the voltage reference vector needs to be limited, since the inverter is supplied with a limited amount of DC bus-voltage. If sinusoidal PWM is used, the maximum voltage magnitude is  $\frac{U_{DC}}{2}$ , and with space vector PWM there is a 15% increase, as shown in chapter 5. Whatever method of PWM is used, there is a maximum magnitude  $U_{max}$  that  $u_r^*$  can be and therefore it needs to be limited: if the voltage reference magnitude  $u_r^* \geq U_{max}$ , then the magnitude is limited to  $U_{max}$ , but the original voltage reference angle is kept, as in (6.3). Also, when the limitation has been reached, a “saturation flag” is set high and stops the integration process in the PI controller, so that the output of the integrators remain constant and do not run away. Finally, the voltage reference in the  $\alpha\beta$  reference frame is obtained as in (6.4). A block diagram showing these concepts is shown in Fig. 6.1.

$$\vec{i}_r = \vec{i}_s e^{-j\theta_r} \quad (6.1)$$

$$\tilde{i}_r = \vec{i}_r^* - \vec{i}_r \quad (6.2)$$

$$\vec{u}_r^* = \begin{cases} U_{max} \angle \alpha_r^* & \text{if } u_r^* \geq U_{max} \\ K_p \tilde{i}_r + K_i \int \tilde{i}_r dt + j\omega_r \hat{\psi}_r & \text{if } u_r^* < U_{max} \end{cases} \quad (6.3)$$

$$\vec{u}_s^* = \vec{u}_r^* e^{j\theta_r} \quad (6.4)$$

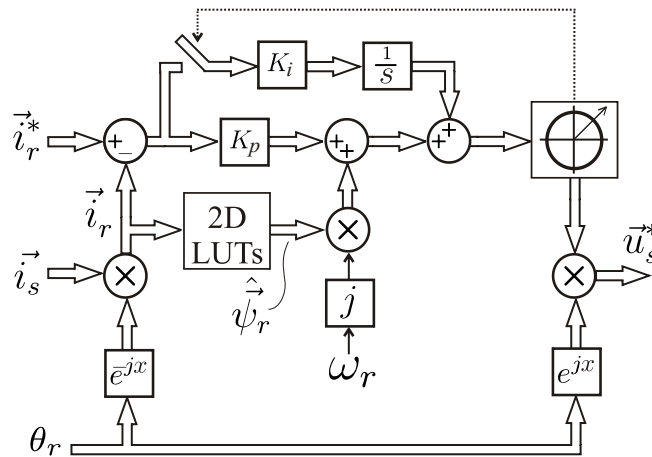


Figure 6.1: Current vector control block diagram.

## 6.2 Zero-position

The current vector control is performed in the synchronously rotating reference frame; therefore the electrical rotor position is required. A mechanical position measurement may be obtained from a position sensor, e.g. resolver or encoder, and can then be converted to the electrical rotor position by multiplication with the number of pole pairs. However, the position measurement may start at any arbitrary position, and therefore an offset needs to be

added so that the  $d$ -axis is aligned with the  $\alpha$ -axis when  $\theta_r = 0$ , according to the definition. This offset is known as the “zero position”.

One method to set the zero position is to apply slowly varying voltage vector (0.1 Hz) with fairly high magnitude and to compare electrical rotor position with  $u_\alpha^*$  and  $u_\beta^*$ . Under these conditions the rotor aligns itself and moves slowly in synchronism, so that  $u_\alpha^* \approx U \cos \theta_r$  and  $u_\beta^* \approx U \sin \theta_r$ . In such a measurement, as shown in Fig. 6.2(a), the phase-difference between the point where  $\theta_r = 0$  and  $u_\alpha^* = 0$  is the zero position. By setting the zero-position to the correct value, 104 degrees in this example, the rotor position measurement is calibrated, as shown in Fig. 6.2(b).

Ch2	$\theta_r$	1	rad/div
Ch3	$u_\alpha^*$	20	V/div
Ch4	$u_\beta^*$	20	V/div
Time	$t$	2	s/div

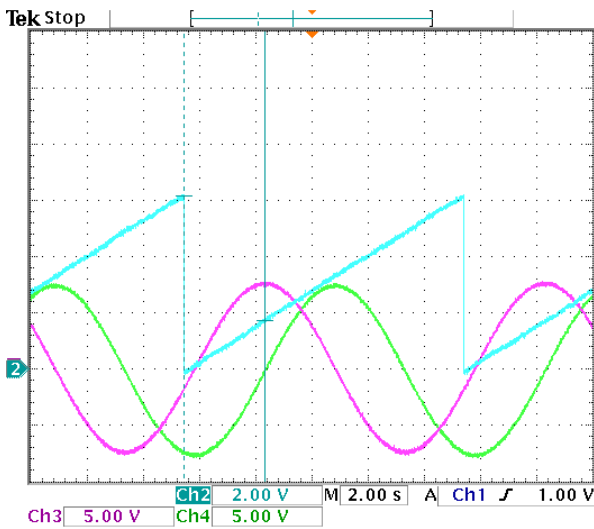
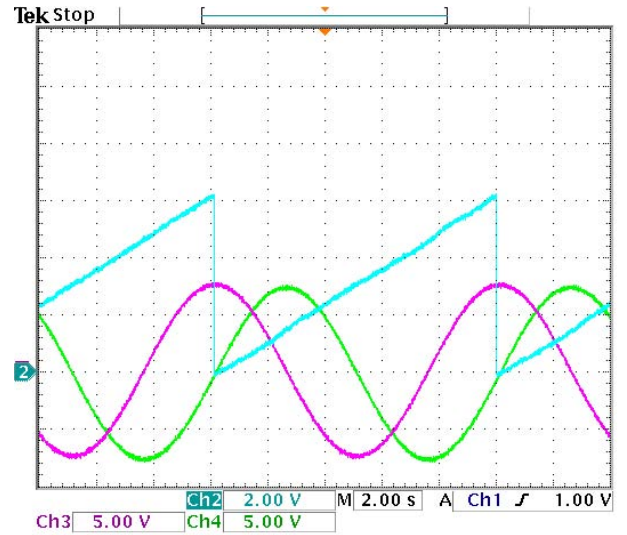
(a) Zero-position =  $0^\circ$ , not aligned.(b) Zero-position =  $104^\circ$ , aligned

Figure 6.2: Aligning the measured- and actual electrical rotor position.

## 6.3 Simulated and practical results

In Fig. 6.3 the  $d$ -axis current control response is shown. The reference magnitude is chosen as the rated magnitude for the  $d$ -axis, i.e.  $i_r^* = 5 \cdot \cos(60)$ , and the current angle is alternated between 0 and 180 degrees, at a rate of 10 Hz. Figures 6.3(a) and 6.3(c) show the simulated and practical results respectively (note the time scale of 20 ms). Figs. 6.3(b) and 6.3(d) show the simulated and practical results, zoomed in on the rising edge of the reference (note the time scale of 1 ms). It is noted that the response time of  $i_d$  is about 8.0 ms.

In Fig. 6.4 the  $q$ -axis current control response is shown. The reference magnitude is chosen as the rated magnitude for the  $q$ -axis, i.e.  $i_r^* = 5 \cdot \sin(60)$ , and the current angle is alternated between 90 and 270 degrees, at a rate of 10 Hz. Figs. 6.4(a) and 6.4(c) show the simulated and practical results respectively (note the time scale of 20 ms). Figs. 6.4(b) and 6.4(d) show the simulated and practical results, zoomed in on the rising edge of the reference (note the time scale of 1 ms). It is noted that the response time of  $i_q$  is about 4.0 ms.

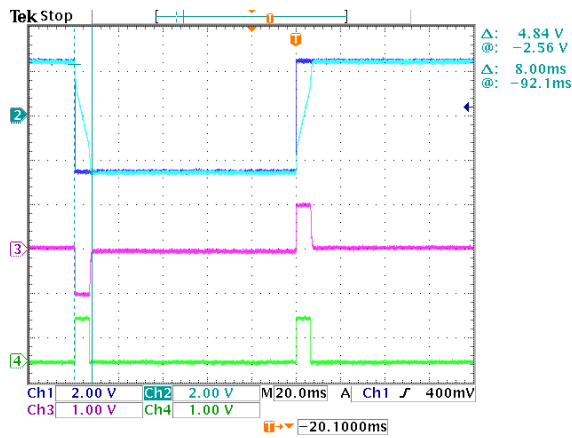
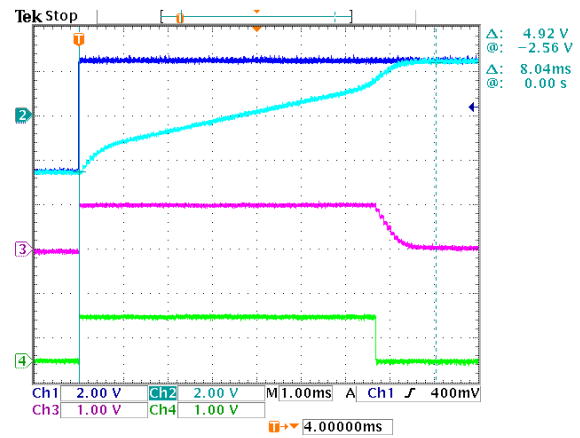
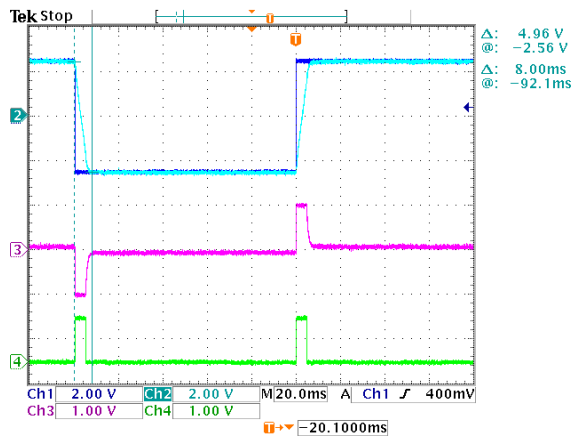
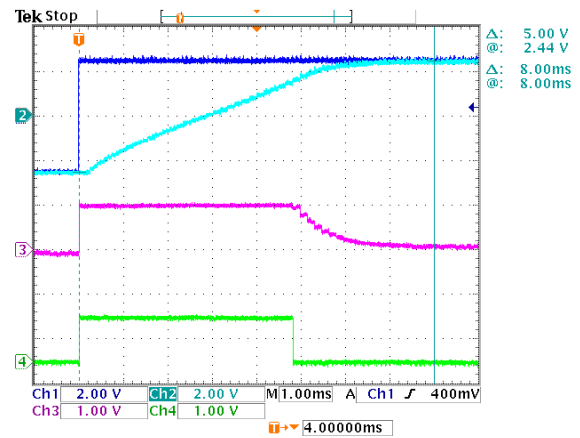
In Fig. 6.4 the MTPA-axis current control response is shown. The reference magnitude is chosen as the rated magnitude for the  $d$ -axis, i.e.  $i_r^* = 5$ , and the current angle is alternated between 60 and 120 degrees, at a rate of 10 Hz. Figs. 6.5(a) and 6.5(c) show the simulated and practical results respectively (note the time scale of 20 ms). Figs. 6.5(b) and 6.5(d) show the simulated and practical results, zoomed in on the rising edge of the reference (note the time scale of 1 ms). It is noted that the response time of  $i_r$  is about 8.0 ms, i.e. the same as the  $d$ -axis current. The reason is that in this example  $i_d$  is required to change sign, while  $i_q^*$  is constant. The choice could also be made that the current angle alternate between 60 and -60 degrees, thereby keeping  $i_d^*$  constant and requiring  $i_q$  to change sign. In the latter case the response time for  $i_r$  should be that of  $i_q$ .

The reason for choosing the upper half of the current plane for the current vector reference instead of the lower half can be found by inspecting Fig. 3.5 closely: theoretically the inverter's voltage limitation affects the lower half of the current plane more, i.e. the achievable points (marked by solid lines) in the lower half are less. This offset is due to the resistive loss term: observe that the voltage in Fig. 3.5(d) is not only a rotation of the flux linkage and scaled by the speed, but the  $R_s \vec{i}_r$  term causes the voltage to be more compressed in the left half of the voltage plane. In practice, at least for this RSM, it was found that it does not matter if the upper half or the left-hand half of the current plane is selected (results are not shown). However, it must be noted that for a permanent magnet assisted RSM, the upper half of the current plane must be selected to obtain equal motoring and generating capabilities [34].



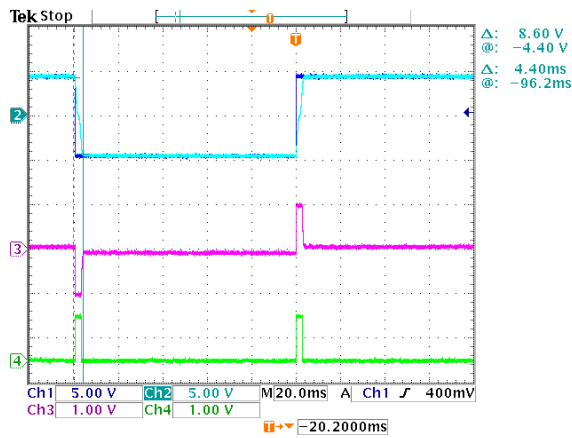
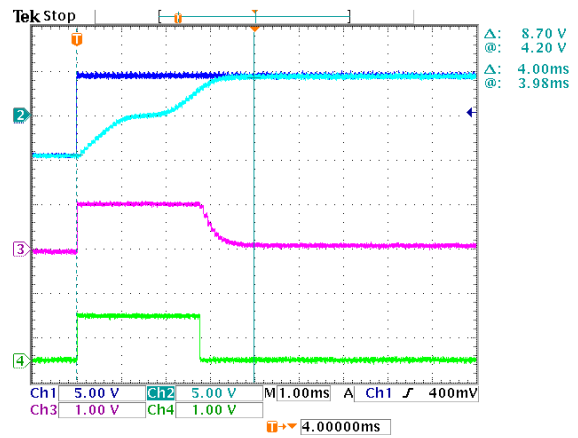
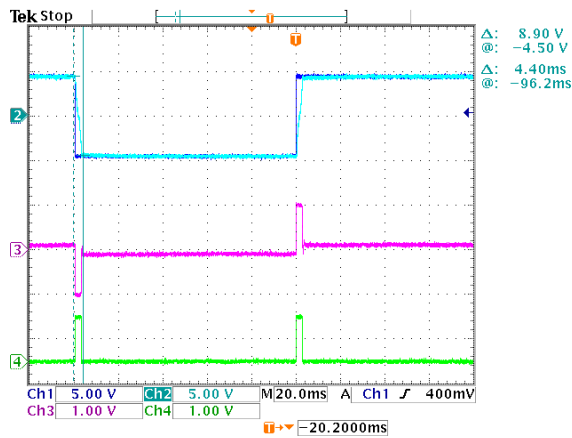
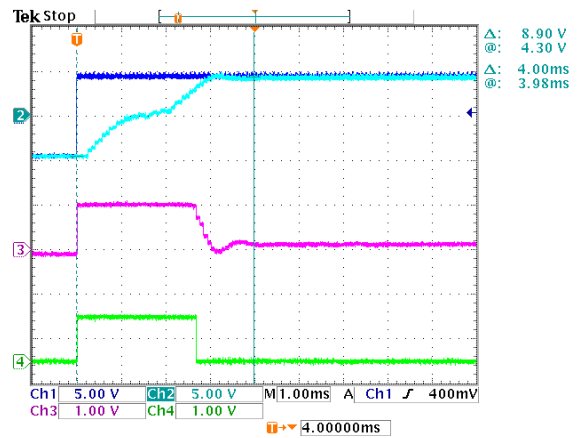
Ch1	$i_d^*$	1	A/div
Ch2	$i_d$	1	A/div
Ch3	$u_d^*$	$(0.54) \cdot U_{dc}$	V/div
Ch4	satflag	1	1/div
Time	$t$	20	ms/div

Ch1	$i_d^*$	1	A/div
Ch2	$i_d$	1	A/div
Ch3	$u_d^*$	$(0.54) \cdot U_{dc}$	V/div
Ch4	satflag	1	1/div
Time	$t$	1	ms/div

(a)  $d$ -axis: simulation(b)  $d$ -axis: simulation zoom(c)  $d$ -axis: practical(d)  $d$ -axis: practical zoomFigure 6.3:  $d$ -axis current control: simulation and practical results.

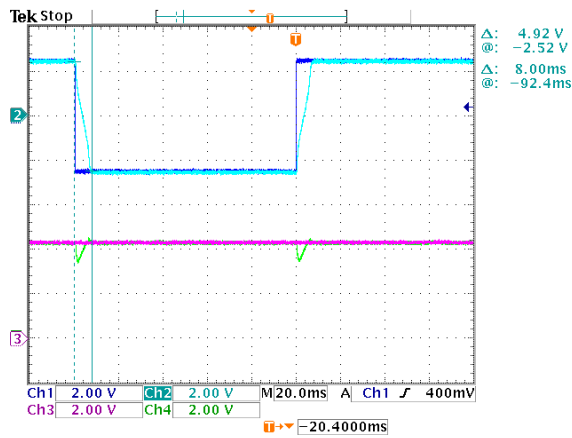
Ch1	$i_q^*$	2	A/div
Ch2	$i_q$	2	A/div
Ch3	$u_q^*$	$(0.54) \cdot U_{dc}$	V/div
Ch4	satflag	1	1/div
Time	$t$	20	ms/div

Ch1	$i_q^*$	2	A/div
Ch2	$i_q$	2	A/div
Ch3	$u_q^*$	$(0.54) \cdot U_{dc}$	V/div
Ch4	satflag	1	1/div
Time	$t$	1	ms/div

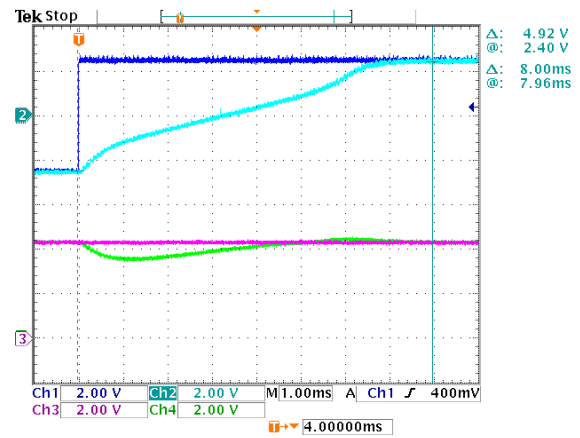
(a)  $q$ -axis: simulation(b)  $q$ -axis: simulation zoom(c)  $q$ -axis: practical(d)  $q$ -axis: practical zoomFigure 6.4:  $q$ -axis current control: simulation and practical results.

Ch1	$i_d^*$	1	A/div
Ch2	$i_d$	1	A/div
Ch3	$i_q^*$	2	A/div
Ch4	$i_q$	2	A/div
Time	$t$	20	ms/div

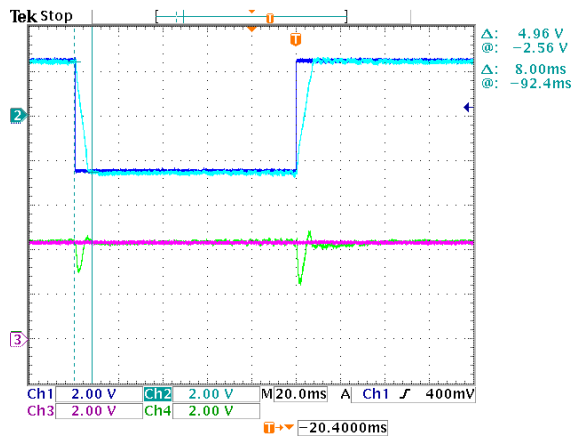
Ch1	$i_d^*$	1	A/div
Ch2	$i_d$	1	A/div
Ch3	$i_q^*$	2	A/div
Ch4	$i_q$	2	A/div
Time	$t$	1	ms/div



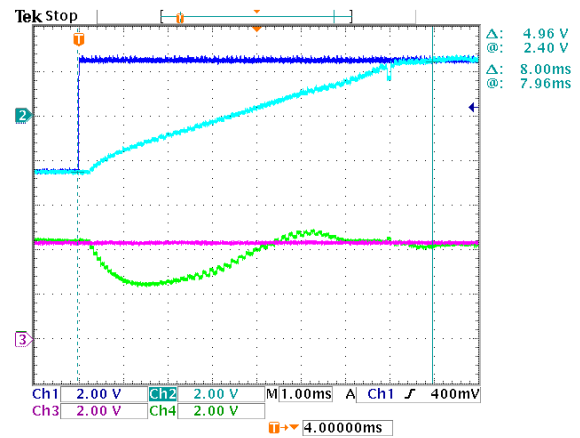
(a) MTPA-axis: simulation



(b) MTPA-axis: simulation zoom



(c) MTPA-axis: practical



(d) MTPA-axis: practical zoom

Figure 6.5: MTPA-axis current control: simulation and practical results.

# Chapter 7

## Torque control

The proposed torque control algorithm in this thesis is generic for a family of synchronous machines namely RSM, PMARSM, PMSM and IPMSM. The work was first developed for a IPMSM [56]. The work was then repeated for the RSM that serves as an example in this thesis, and the results will be shown here for the first time, i.e. they have not been published at conferences or in journals. In this chapter a straightforward torque control strategy for the entire speed range is demonstrated. Practical implementation is very simple, since the calculations are removed from the load of the digital signal processor and are done off-line in an automated process. The process relies on machine specific data from finite element analysis and therefore includes non-linear effects such as saturation and cross-coupling. Simulated and practical results show that the torque is controlled effectively in the entire speed range.

### 7.1 Optimal indirect torque control

Open loop torque control is implemented for zero to maximum speed using a method that gives Maximum Torque per Ampere (MTPA) below base speed and efficient field weakening (FW) above base speed. As the speed of the motor increases, the back-EMF also increases: at the “base speed” the back-EMF magnitude is approximately equal to the maximum voltage magnitude that can be given by the inverter. At high speeds the flux linkage magnitude needs to be reduced to avoid voltage saturation, but at the same time the flux linkage angle needs to be chosen so that the maximum achievable amount of torque can be generated so that the maximum speed achievable may be increased.

Using Finite Element (FE) analysis or practical measurements, the MTPA points of the  $dq$  current plane may be identified, as shown in Fig. 3.5, and used within a lookup table (LUT). Either way, once the machine advances beyond a certain speed, the flux linkage caused by the MTPA current reference cannot be maintained due to the inverter’s voltage limitation. Current references have to then deviate from the MTPA locus in order to get the flux linkage magnitude within limit. Moreover, assuming copper losses to be dominant, the current references above base speed have to be selected to be as close to the MTPA locus as

possible.

Some torque control strategies within the FOC category, similar to what has been presented in this article, have been suggested [45, 50, 49]. In [45], the torque control problem is explained very well. The authors suggest a control scheme within the synchronously rotating  $dq$  reference frame. The  $q$ -axis current reference is given by a PI speed controller, and the  $d$ -axis current reference is calculated: a decision between MTPA or FW control is made based on the measured speed, and in both cases, the  $d$ -axis current reference is calculated using analytical machine equations with constant parameters. High dynamic decoupling current controllers are used to give the voltage reference. A voltage reference compensation function, to limit the voltage reference in a way that give preference to controlling the  $d$ -axis current, is also suggested. It has been demonstrated that this kind of control leads to a much greater output torque, compared to a control scheme that does not utilize the reluctance torque, and also that a high dynamic response is possible. The switch-over from MTPA to FW does not seem to be a problem, using the given decision-making trees. In [50] and [49], similar ideas are presented.

From FE analysis we know that the machine parameters are not constant, and in applications such as electrical vehicles where the DC bus voltage can vary widely, a decision for current references based only on the measured speed will not work. Any scheme that is based on parameter approximation of the non-linear functions, and that uses complicated decision trees, does not seem to be the most simple and elegant solution. For industry acceptance, a scheme that is easy to implement, is always an advantage.

In the following suggested algorithm, the flux linkage magnitude restriction is calculated using the measured speed and the measured DC bus voltage and the calculation also considers the type of PWM applied (e.g. sinusoidal or space vector). The correct current reference for the requested torque, under the flux linkage magnitude restriction, is then obtained from two-dimensional lookup tables (LUTs). In this method, there is a direct translation from the torque reference and flux linkage restriction to the current vector reference, i.e. there are no complicated equations, approximation or any decision-making tables, plus the method may work at any DC bus voltage and any speed. Therefore, the calculation effort has been removed from the load of the DSP and is rather performed off-line. FE results are used directly and there is no approximation of parameters. Implementation is greatly simplified.

Fig. 7.1 shows the basic idea, where  $f$  is a function that has the measured DC bus voltage  $U_{DC}$  and the estimated electrical speed  $\hat{\omega}_r$  as inputs, and is used to calculate a flux linkage magnitude constraint  $|\psi_r|_{MAX}$ . This constraint is used with the torque reference  $T_m^*$  as inputs to a set of 2D lookup tables (LUTs), which give the current vector reference in the synchronously rotating  $dq$  reference frame  $\vec{i}_r^*$ .

Considering the voltage vector equation 2.12, the flux linkage magnitude restriction for steady state may be approximated by (7.1), where  $U_{max}$  is the maximum voltage vector magnitude that may be obtained (e.g.  $U_{max} = 0.5U_{DC}$  for sinusoidal PWM, and  $U_{max} = 0.575U_{DC}$  for space vector PWM) and  $U_{buf}$  is a voltage buffer that is kept for the resistive

voltage drop and derivative of the flux linkage vector term. The creation of the 2D LUTs is explained in the next section.

$$|\vec{\psi}_r| < \frac{U_{max} - U_{buf}}{\omega_r} \quad (7.1)$$

## 7.2 Optimal current vector reference

Since the electrical machine is non-linear due to saturation and cross-coupling, it is not a trivial task to obtain optimal performance. The proposed method makes direct use of finite element (FE) results to derive a set of 2D lookup tables (LUTs) that give the optimal current vector reference for any speed and any DC bus voltage.

To create the LUTs, a series of constraints are expressed as contour lines on the  $dq$  current plane and decision-making logic is used to find the correct current references. First of all, the MTPA contour is used as the line that represents the optimal solution. The torque reference contour and maximum flux linkage contour represent the constraints. (A constraint on the current magnitude may also be given, or in the case of the IPMSM, the negative  $d$ -axis current may be limited as in [56], but it has not been done here in this example.) To illustrate the decision logic, three examples are given next.

At high speed, for a given DC bus voltage, there is a maximum flux linkage that may be obtained and can be approximated by (7.1). A current reference that lies on the maximum flux linkage contour needs to be selected, and therefore the reference torque may not be obtained. However, a point ( $dq$  current combination) on the maximum flux linkage contour giving a torque that is as close to the reference torque as possible can be selected. In this case therefore, maximum torque per given amount of voltage (MTPV operation) is obtained. This situation is shown in Fig. 7.2(a).

At medium speed, the maximum flux linkage constraint is not so tough, and it could be possible to obtain the reference torque. In this case, the intersection of the torque reference contour and maximum flux linkage contour is selected. This situation is shown in Fig. 7.2(b). In fact, as can be clearly seen, there are two points of intersection - the point that results in

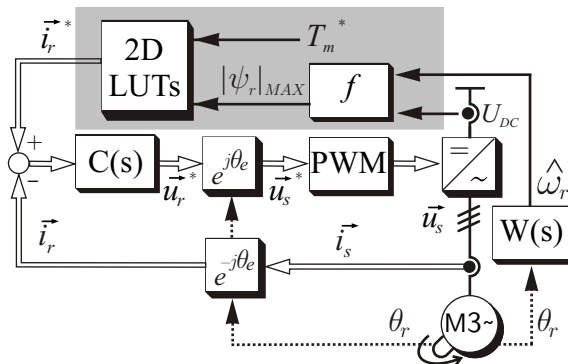


Figure 7.1: Torque control block diagram.

the lowest current magnitude is selected.

At low speed, the maximum flux linkage constraint is very light, and it could be possible to obtain the reference torque using less flux linkage than the constraint, i.e. to use a point on the MTPA curve. This situation is shown in Fig. 7.2(c).

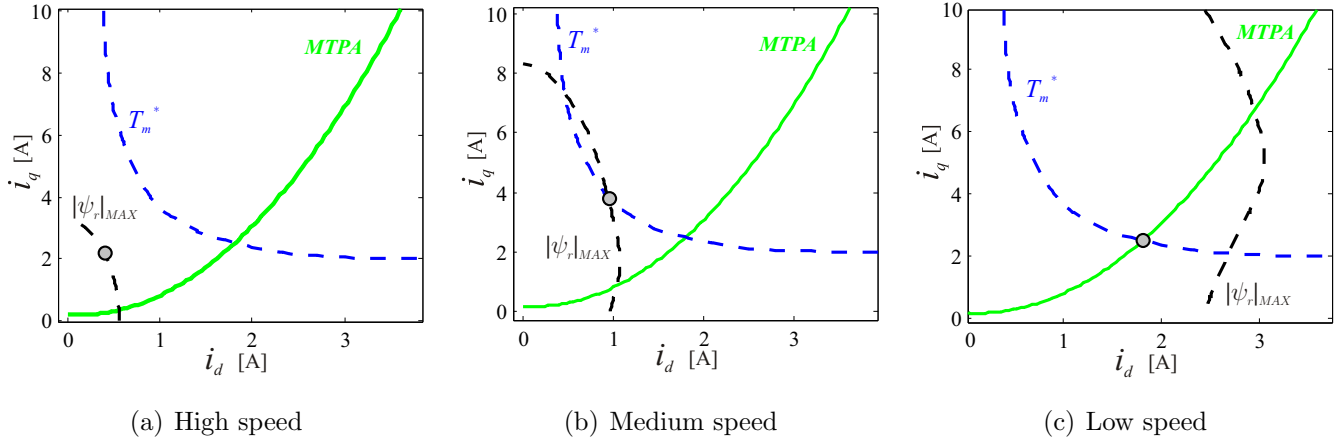


Figure 7.2: Three examples for torque control table creation.

To further illustrate this concept, two additional figures are shown in Fig. 7.3(a) and Fig. 7.3(b). They show the chosen current vector points (filled grey circles) for a series of flux linkage magnitude restrictions (black dotted contours) for half rated torque reference and full rated torque reference respectively.

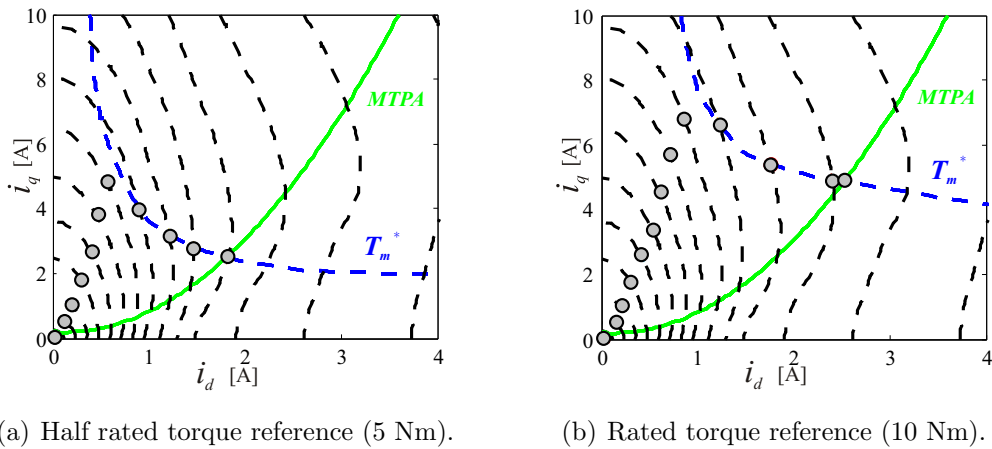


Figure 7.3: Torque control lookup table creation.

Two tables are created in an automated decision-making process, for use inside the control program, and are illustrated by Figs. 7.4(a) and 7.4(b). This decision-making process has been automated so that the 2D tables are constructed within minutes. See section B.3 to download the Matlab program (m-file) that was used to create these tables. A program flow diagram is given in Fig. 7.6.

The obtained flux linkage magnitude and torque for the specified choice of current references, are illustrated by 7.5(a) and Figs. 7.5(b) respectively. In Fig. 7.5(b) it can be clearly

seen that for low maximum flux linkage magnitude (high speed), the reference torque is not obtained. For higher maximum flux linkage magnitude (lower speed) the reference torque can be obtained. Fig. 7.5(a) shows that for a high maximum flux linkage magnitude (low speed), the amount of flux linkage that is used is less than that available: in this way the machine operates efficiently.

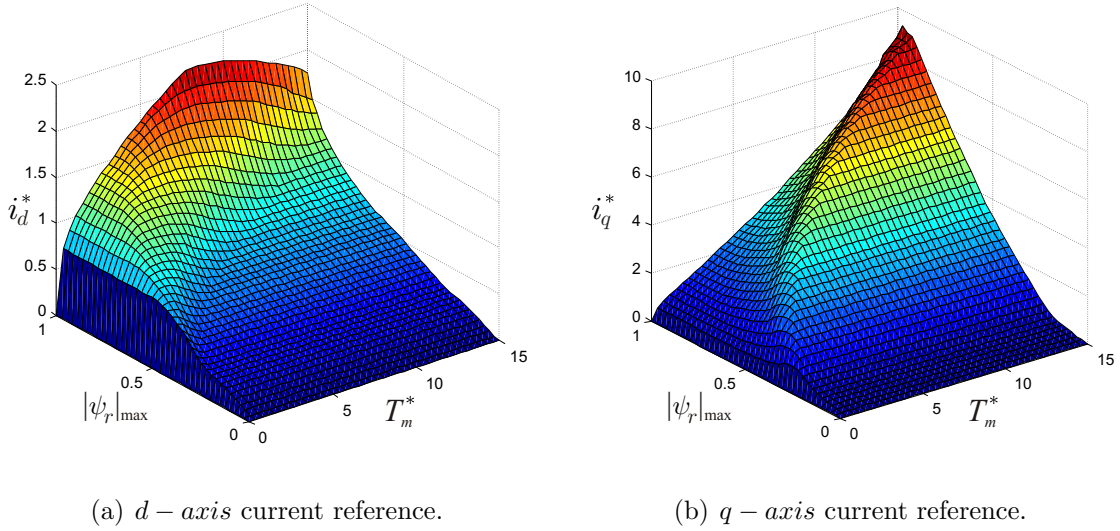


Figure 7.4: Torque control: lookup tables.

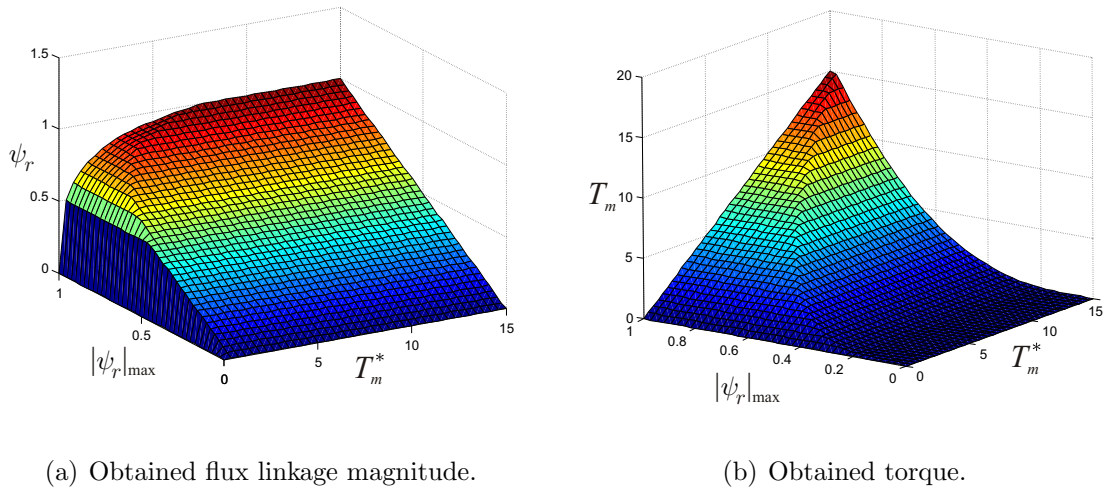


Figure 7.5: Expected torque and flux linkage magnitudes.

The concept was first developed for an IPMSM [56], after which the whole process and implementation for the RSM was repeated within a very short period of time. Since 2D interpolation is used in the control program, the table size can also be fairly small. A lookup operation is also much faster than any iterative decision-making logic during execution. The method is exact, because it uses the FE analysis, so there is not even an attempt to linearize the machine or to find approximation functions.



For further details on implementation, please refer to the Matlab Simulink simulation files (see section B.1 to download simulation files), as well as the actual control program (see section B.4 to download the ANSI-C program).

## 7.3 Simulated and practical results

In the following results, the flux linkage magnitude restriction was chosen as follows:  $|\psi_r|^* = \frac{0.45 \cdot U_{dc}}{1 + \hat{\omega}_r}$ ; the voltage vector limit for the current vector controller output is chosen as  $U_{max} = 0.54 \cdot U_{dc}$ , and the maximum voltage vector magnitude that can be given by the modified PWM strategy is  $U_{PWM-max} = 0.575 \cdot U_{dc}$ . These limits are important to avoid long periods of voltage saturation, i.e. no controllability.

A dynamic test is performed whereby a torque reference reversal is applied under no load conditions, i.e. first a positive torque reference of 9 Nm is given (rated torque) and the machine is allowed to speed up and go into flux weakening; then a negative torque reference of -9 Nm is given and the machine is allowed to reverse its speed. The simulation result is shown in Fig. 7.7(a), while the practical result is shown in Fig. 7.7(b). Both simulation and practical test were performed using the rapid prototyping system. Important to note is the equal performance in both directions, i.e. the same speed magnitude is reached in each case, indicating that the zero-position is set correctly and that the control algorithm that includes field weakening is effective.

In Fig. 7.7 the estimated torque  $\hat{T}_m$ , estimated speed, current magnitude  $i_r$  and current angle  $\phi_r$  are shown. Unfortunately the practical setup with the RSM did not have a torque sensor, so that the actual torque could not be measured and compared to the estimated torque.

In Fig. 7.8 the torque vs. speed curves are shown, which were obtained by post-processing the results shown in Fig. 7.7. The torque is normalized with 9 Nm and the speed is normalized with 1500 rpm, which are the rated values for this RSM. The torque is simply plotted against the speed, and from the result it is clear that equal four quadrant performance is obtained. Simulation and practical results correlate very well, but as mentioned previously, the actual torque measurement was unfortunately not available.

## 7.4 Summary: torque control

An optimal torque control strategy was presented in this chapter that is applicable to a family of machines, namely the RSM, PMSM, PMARSM and the IPMSM. It was shown in [56] that the method works for an IPMSM for an electrical vehicle application. In that publication, steady state tests are shown that include the actual torque measurement. In this chapter it is shown that the ideas are equally applicable to the RSM, and a dynamic test is shown. The method is “optimal” since for any speed or DC bus voltage, a current vector reference is selected that will result in either maximum torque per ampere (MTPA)

or efficient field weakening. Voltage saturation is avoided by always giving an achievable current vector reference. It is clear from Fig. 7.7 that the scheme works under dynamic conditions. From Fig. 7.8 it is clear that the flux weakening capability of an RSM is not so good (comparing this to the results in [56] for the IPMSM). However, there are applications for which the flux weakening range is not strictly necessary, e.g. fans or pumps.

Several other publications about torque control have been studied and are given here [46, 38, 75, 39, 40, 24, 47, 48, 41, 72, 42, 43, 76, 51, 52, 77, 44]. These works will not be compared to the method shown in this chapter due to time and space constraints, but it is believed that the developed torque control algorithm has the merit to stand with other important works about torque control. The method shown in this chapter was developed, implemented and tested within a period of six months. This torque controller is just as dynamic as the current vector controller. No particular attention was given for reducing the amount of torque ripple. The method is very easy to implement, since it relies completely on a set of 2D lookup tables (LUTs). The construction of the 2D LUTs is based on results from FE analysis, and can be automated so that the construction is completed within a few minutes. Good results were obtained for steady state and dynamic tests.

The actual implementations of the 2D Lookup Tables construction, the control system Simulation in Matlab Simulink and the practical implementation in ANSI-C can be downloaded: see appendix B.

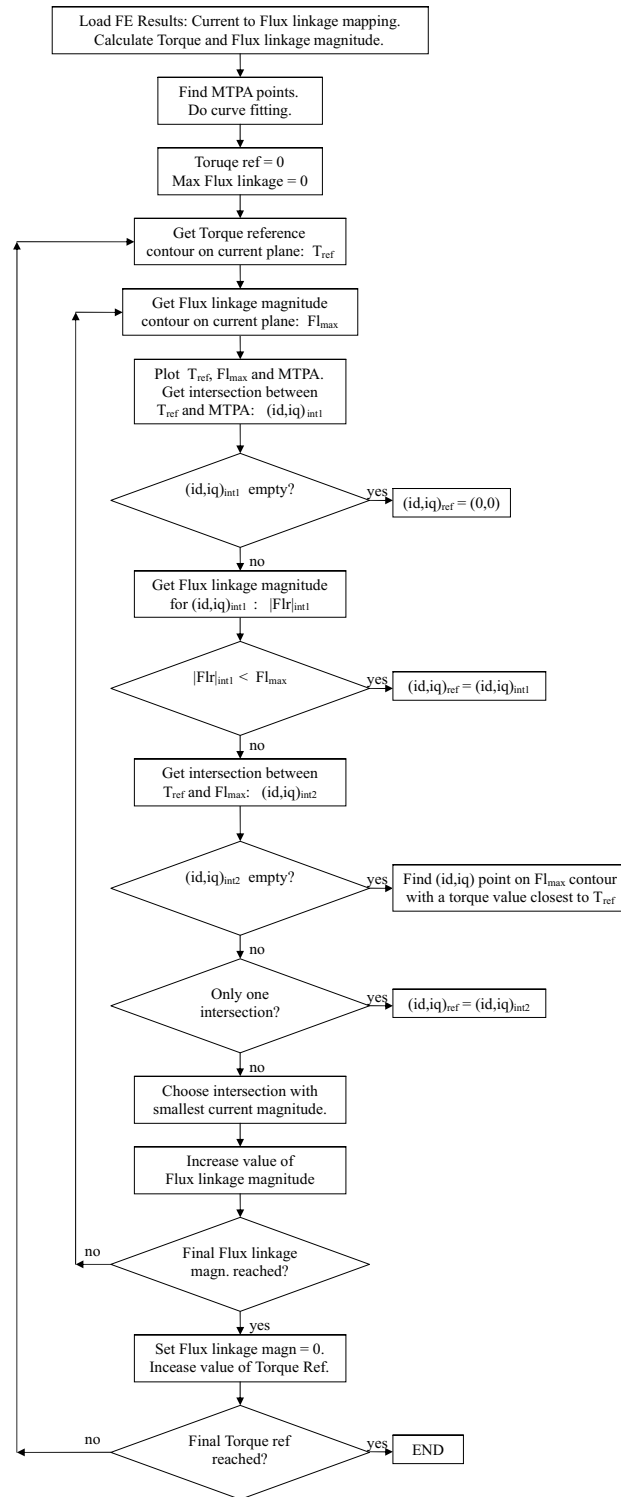
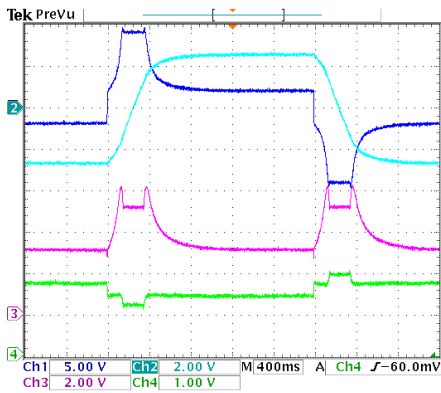
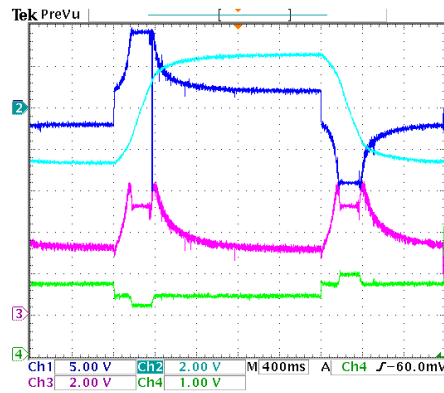


Figure 7.6: Program for LUTs creation flow diagram.

Ch1	$\hat{T}_m$	5	N.m/div
Ch2	speed	2000	rpm/div
Ch3	$i_r$	2	A/div
Ch4	$\phi_r$	1	rad/div
Time	$t$	400	ms/div

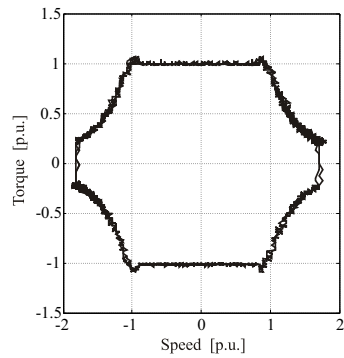


(a) Torque control: simulation.

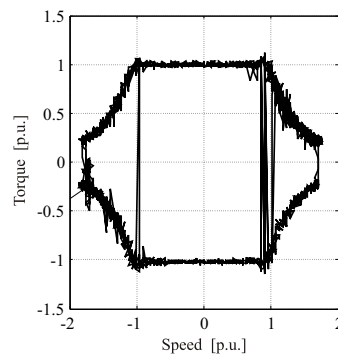


(b) Torque control: practical.

Figure 7.7: Torque control dynamic test - simulation and practical results.



(a) Torque vs Speed: simulation.



(b) Torque vs Speed: practical.

Figure 7.8: Torque vs Speed - simulation and practical results.

# Chapter 8

## Speed control

The focus of this thesis is not on speed control specifically, and therefore this chapter only gives a quick discussion and show some simulation and practical results. For the implementation of the speed controller a simple PI controller was used that gives a torque reference. The torque controller described in the previous chapter then takes care that the reference torque is reached. Of course, under high speed conditions it could be that the actual torque cannot reach the torque reference from the speed controller due to the inherent flux linkage magnitude constraint. Under such conditions windup in the speed controller's integrator should be avoided.

Since there is access to lookup tables (LUTs) that gives an estimate of the flux linkage vector from the current vector in the  $dq$  reference frame, it is also possible to estimate the torque and ultimately the load torque [53, 54, 34]. By adding the estimated load torque to the output of the speed PI controller, the load torque is essentially decoupled and the work of the PI controller is reduced to only take care of speed reference changes. In this thesis only a simple PI controller is used and a few no load tests are presented, in effect just to show that the torque controller is functional as part of a speed controller.

### 8.1 Dynamic tests

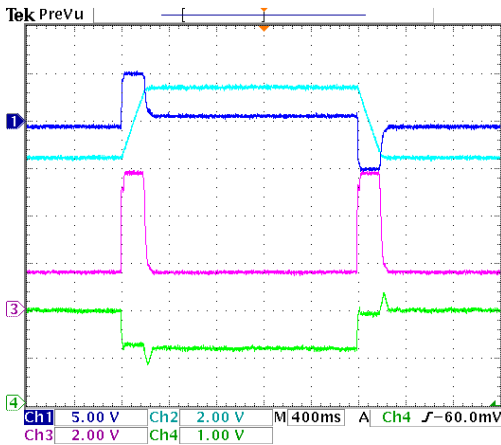
In the following no-load tests, a speed reference of the rated positive and negative speed is given (see Fig. 8.1(a) for the simulation result and Fig. 8.1(b) for the practical result), and then a speed reference of twice the rated positive and negative speed is given (see Fig. 8.1(c) for the simulation result and Fig. 8.1(d) for the practical result). In the table describing the signals  $\hat{T}_m$  is the estimated load torque,  $i_r$  is the current magnitude and  $\phi_r$  is the current angle.

From the figures it is clear that the simulation and practical results are in very good correlation. It is also clear that the current magnitude  $i_r$  does not go to zero when the speed reference has been reached, although the estimated torque goes to zero. The reason is that these tests are performed with modified LUTs in the torque controller that always gives a  $q$ -axis current reference, even under no-load conditions, i.e. maximum torque per Ampere

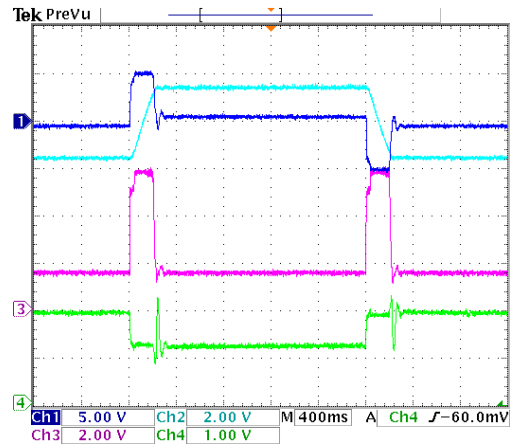
is not followed. The reason for giving a  $q$ -axis current reference under no-load conditions will become clear in the chapter about position sensorless control - the  $q$ -axis of the RSM needs to be saturated in order for the position estimator based of HF signal injection to correctly find the rotor position. These dynamic speed tests were however performed using the measured position signal to do the field orientated control.

Ultimately it is clear that speed control is fairly dynamic under no load conditions and that the RSM is able to reach even up to twice the rated speed. Due to time constraints and scope limitation of the thesis no further tests with the speed controller were performed.

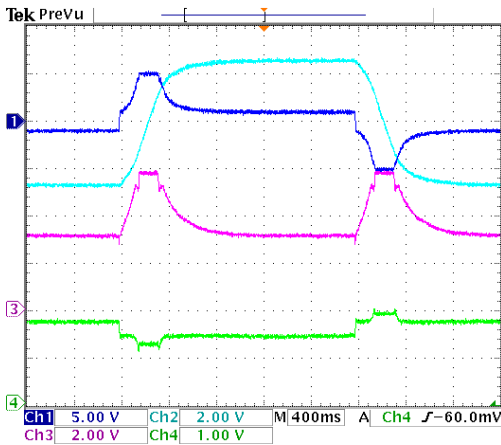
Ch1	$\hat{T}_m$	10	N.m/div
Ch2	Speed	2000	rpm/div
Ch3	$i_r$	2	A/div
Ch4	$\phi_r$	1	rad/div
Time	$t$	400	ms/div



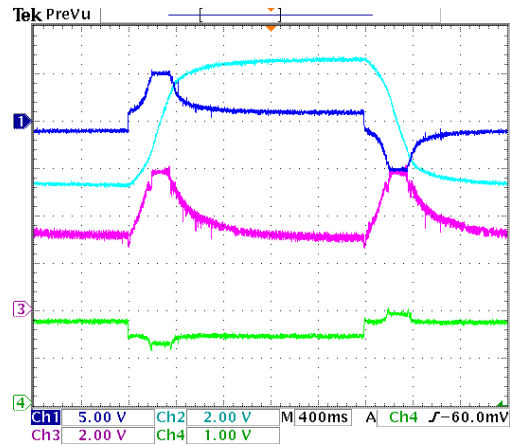
(a) Speed control (rated): simulation.



(b) Speed control (rated): practical.



(c) Speed control (2.0 x rated): simulation.



(d) Speed control (2.0 x rated): practical.

Figure 8.1: Speed control: no load dynamic tests.

# Chapter 9

## Position sensorless control

The idea of position sensorless control is already very mature. Research work started in the 1980's and the focus was mainly on the induction machine. Although the induction machine still seems to be the industry standard, there has been a gradual shift towards synchronous machines, with energy efficiency being the main driving force. In recent years the permanent magnet synchronous machine (PMSM) received much attention. The reluctance synchronous machine (RSM), often confused with the switched reluctance machine (SRM), is far less popular. Combined reluctance and PM machines, i.e. interior PMSM (IPMSM) and PM-assisted RSM (PMARSM), have also received some attention.

The amount of literature available about sensorless control is overwhelming. For the most part, any literature concerning the induction machine is not considered in this work. Only the literature regarding the family of synchronous machines: RSM, PMSM, IPMSM and PMARSM, were considered. Although this thesis focuses mainly on the RSM, references regarding the PMSM and IPMSM are given here, since the ideas presented are important and often generic [78, 79, 80, 5, 81, 82, 83, 84, 6, 85, 86, 7, 87, 88, 8, 4, 9, 89, 10, 90, 91, 11, 92, 12, 93, 94, 14, 95, 96, 64, 13, 97, 98, 99, 100, 101, 102, 15, 103, 104, 105, 106, 107, 108, 109, 110, 111, 112, 57, 113]. References regarding RSM and PMARSM that are considered are also given here [17, 18, 19, 20, 21, 22, 23, 24, 25, 26, 27, 28, ?, 29, 35, 36, 114, 30, 31, 32]. More general discussions about sensorless control for these machines can be found in [115, 116, 117, 118, 119, 12, 110, 120, 121, 55, 113, 55].

Position sensorless control requires either a control scheme that does not need the rotor position, as in the case of direct torque control (DTC), or the position must be estimated, as in the case of field orientated control (FOC). This work does not discuss DTC, however it can be noted that even for DTC a position signal is required at startup [7]. Since the optimal torque control strategy introduced in chapter 7 makes use of FOC, an accurate position estimation in the whole speed range is required.

Considering the voltage equation, the rotor position information is embedded in the voltage, current and flux linkage, if the frequency is greater than zero. Therefore, if one has an accurate fundamental model of the machine, a fundamental model-based rotor position estimator may be used. However, at zero speed in the steady state, the voltage equation

reduces to the resistive voltage drop, and no position information is available. At low speed a fundamental model based position estimation scheme would be plagued by machine model errors (the stator resistance changes in the course of time due to heat dissipation), as well as non-ideal inverter effects such a dead-time. Stator resistor estimation and dead-time compensation can improve the performance of such an estimator. More advanced methods such as neural networks (NN) and artificial intelligence (AI) could be used to assist in this process.

An alternative method is to apply high frequency (HF) voltages onto the machine using the standard inverter, and to use saliency information embedded in the HF currents to estimate the rotor position. Considering the voltage equation again, now with HF signals, the voltage equation reduces to the time-derivative of the flux linkage term, as explained in section 3.4. Therefore the machine itself can be used as a resolver when it has magnetic saliency or magnetic anisotropy. In general the RSM, PMARSM, PMSM and IPMSM all have magnetic saliency to a certain extent.

The fundamental model based position estimation is only accurate when the back-EMF is sufficiently large. The back-EMF is the product of the flux linkage and speed; therefore both quantities need to be large enough. The HF-model based position estimation is only viable for low speed, since at high speed the maximum voltage is needed and a part of the voltage should not be used for additional HF voltage excitation. To combine these different estimation methods, some researchers have proposed phase-over methods or Kalmen filters. Another approach is to keep the fundamental-model based position estimation active all the time, and assist it with HF signals at the critical working points.

This chapter starts with the fundamental model based approach to position estimation. Then the HF-model approach is discussed in detail, since this was the focus and starting point for this work. Finally a hybrid or combined approach is discussed.

## 9.1 Fundamental model based position estimation

In recent years there have been some publications about fundamental-model based rotor position estimation for RSM, PMSM, PMARSM and IPMSM. In [6] an extended back-EMF model is introduced, which is used to derive a least order rotor position and speed observer. In [8] the extended back-EMF model is also used, but a state filter in the stationary reference frame is used, unlike the scheme in [6], which is implemented in the estimated rotating reference frame. A more traditional approach is followed in this thesis, which is similar to that used in [36]. A complete explanation with mathematical derivation and estimator block diagram, as well as practically measured results are presented in this section.

The space phasor voltage equation for synchronous machines in the stationary ( $\alpha\beta$ ) reference frame is given in equation (9.1): the stator voltage is the sum of the resistive voltage drop and the back-EMF. Therefore, the back-EMF vector can simply be estimated by subtracting the resistive voltage drop from the voltage vector. However, the stator voltage



is not measured in practice (to avoid additional cost), and therefore it needs to be estimated as well. In practice, the voltage vector reference input to the pulse-width modulator is taken as the estimate of the voltage that is applied to the machine terminals. Since dead-time is added to the switching signals for the inverter, and due to other unmodelled and non-linear inverter effects, the actual terminal voltage is not exactly equal to the reference. The error between the actual voltage and the voltage reference is significant for small voltage references, which means at low speed and low flux linkage in the steady state, since the back-EMF is then small. Furthermore, the stator resistance  $R_s$  is not constant, since it is a function of temperature. In practice, the stator resistance is measured once, and this value is used as a constant in the estimation. The  $\vec{u}_s$  estimate could therefore be improved by doing dead-time compensation and stator resistance estimation [112].

The stator terminal currents are measured in practice and usually only two phases, since the third phase can be calculated under the assumption that the sum of the three-phase currents is zero. However, one should note that the obtained current vector, calculated from these terminal current measurements, is not exactly equal to the magnetizing current vector, as used in (9.1), due to iron-loss [122]. One should also note that offsets in the current measurement circuit will lead to an offset error in the estimated back-EMF. Following all these considerations, the back-EMF estimation is given in (9.2).

The back-EMF is the derivative of the air-gap flux linkage vector, as in (9.3). Therefore, the flux linkage vector  $\vec{\psi}_s$  can simply be estimated as the integral of the back-EMF. However, the initial conditions are necessary, as shown in (9.4). Since in practice the initial conditions are normally chosen as zero, there will be an offset in the estimated flux linkage vector, and integrator drift will further increase such an offset.

Therefore, a mechanism is required to compensate the integrator drift. The model of the machine in the synchronously rotating reference frame can assist us in this regard. Using an estimate of the rotor position (this will be dealt with soon, for now, just assume that we have it or that we use the measured position), the estimated current vector in the  $dq$  reference can be obtained, as in (9.5) (this is required for the current control as well). Using a model of the machine in the  $dq$  reference frame (here it is assumed that the model is non-linear and that a 2D lookup tables (LUT) with 2D interpolation is used to translate from  $\vec{i}_r$  to  $\vec{\psi}_r$ , as obtained from finite element (FE) analysis), the flux linkage vector estimate in the  $dq$  reference frame is obtained, as in (9.6). Using  $\vec{\psi}_r$ , we can obtain another flux linkage estimate in the  $\alpha\beta$  reference frame, as shown in (9.7). The vector  $\hat{\psi}_{sL}$  does not have an offset and is basically our model reference - we can compare it to the estimate  $\hat{\psi}_s$  and use the error to eliminate the integrator drift.

The drift compensation therefore relies on a second estimation of  $\psi_s$ , which does not contain an offset, and the difference between the two estimates is scaled with a small gain  $K_3$  and added to the back-EMF estimate in (9.2), before it is integrated to obtain the flux linkage estimate.

The final step in this estimator is to get the position estimate from the estimated flux

linkages. Using the dot (scalar) product as in (9.9) and (9.10), and normalizing the signals with the product of the vector magnitudes, the cosine and sine of the rotor position are obtained respectively.

$$\vec{u}_s = R_s \vec{i}_s + \vec{e}_s \quad (9.1)$$

$$\hat{e}_s = \vec{u}_s^* - \hat{R}_s \hat{i}_s \quad (9.2)$$

$$\vec{e}_s = \frac{d\vec{\psi}_s}{dt} \quad (9.3)$$

$$\hat{\psi}_s = \int \hat{e}_s dt + \hat{\psi}_{s0} \quad (9.4)$$

$$\hat{i}_r = \hat{i}_s e^{-j\hat{\theta}_r} \quad (9.5)$$

$$\hat{\psi}_r = \text{LUT} \left\{ \hat{i}_r \right\} \quad (9.6)$$

$$\hat{\psi}_{sL} = \hat{\psi}_r e^{j\hat{\theta}_r} \quad (9.7)$$

$$\vec{e}_{\text{drift}} = K_3 \left( \hat{\psi}_{sL} - \hat{\psi}_s \right) \quad (9.8)$$

$$\cos \hat{\theta}_r = \cos \left( \hat{\delta}_s - \hat{\delta}_r \right) = \frac{\hat{\psi}_r \cdot \hat{\psi}_s}{\hat{\psi}_r \hat{\psi}_s} \quad (9.9)$$

$$\sin \hat{\theta}_r = \sin \left( \hat{\delta}_s - \hat{\delta}_r \right) = \frac{j \hat{\psi}_r \cdot \hat{\psi}_s}{\hat{\psi}_r \hat{\psi}_s} \quad (9.10)$$

It is not strictly necessary to get  $\hat{\theta}_r$  on its own, since the cosine and sine of  $\hat{\theta}_r$  are used in the forward and reverse transformations between the stationary and the synchronously rotating reference frames. However, for comparison to the measured rotor position and also for speed estimation,  $\hat{\theta}_r$  may be obtained directly using the arctan function and  $\hat{\omega}_r$  may be obtained from  $\hat{\theta}_r$  by differentiation. Differentiation is generally frowned upon, since any noise results in spikes when differentiated. An alternative method to estimate the speed is using a phase locked loop (PLL) structure that is a rotating vector tracker. Equations (9.11) through (9.15) represent such a PLL. Note that in practice the cosine and sine terms are used to calculate the cross product in (9.11), therefore the normalized signals (9.9) and (9.10) can be used directly.

$$\theta_{\text{err}} = j e^{j\theta_{\text{obs}}} \cdot e^{j\hat{\theta}_r} = \sin \left( \hat{\theta}_r - \theta_{\text{obs}} \right) \approx \hat{\theta}_r - \theta_{\text{obs}} \quad (9.11)$$

$$\omega_{\text{obs}} = \int K_2 \theta_{\text{err}} \quad (9.12)$$

$$\theta_{\text{obs}} = \int (\omega_{\text{obs}} + K_1 \theta_{\text{err}}) \quad (9.13)$$

$$K_1 = 2BW_{\text{obs}} \quad (9.14)$$

$$K_2 = BW_{\text{obs}}^2 \quad (9.15)$$

The full estimator shown here is an estimator of the back-EMF in  $\alpha\beta$ , the current in  $dq$ , the flux linkage in  $\alpha\beta$  and  $dq$ , the rotor position and the rotor speed. It only works when

there is a certain amount of flux linkage and when the rotor speed is fairly high. The block diagram in Fig. 9.1 shows the complete estimator with PLL for the speed estimation.

In Fig. 9.1, the cosine and sine terms are not normalized, as in equations (9.9) and (9.10). The normalization is necessary when these signals are used directly for the reference frame transformation, or if the PLL method is used as suggested here, the normalization is still necessary to keep the bandwidth of the PLL constant. However, normalization is not strictly necessary for the PLL to work, it just affects the bandwidth.

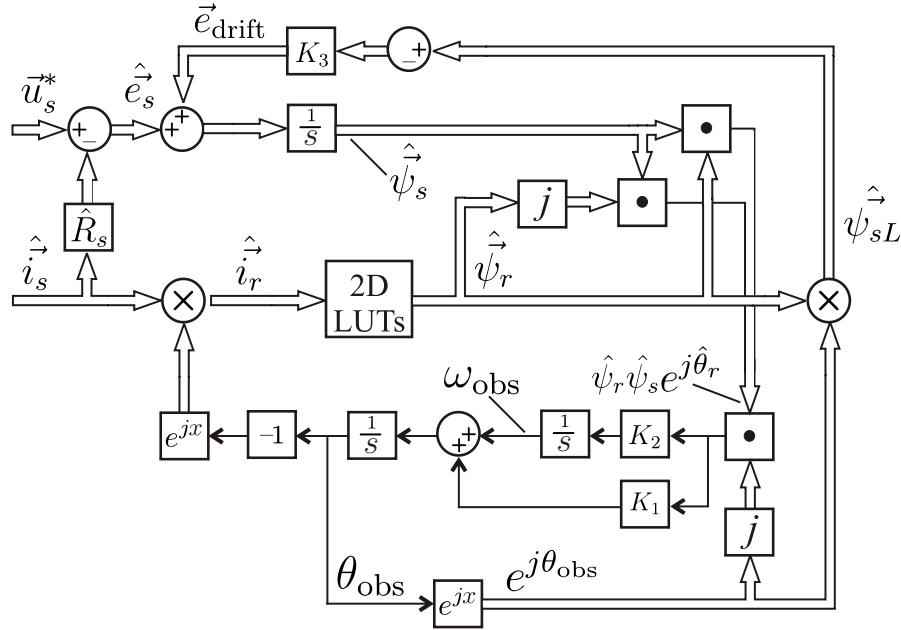


Figure 9.1: Position estimated based on fundamental model

### 9.1.1 Simulation and practical tests

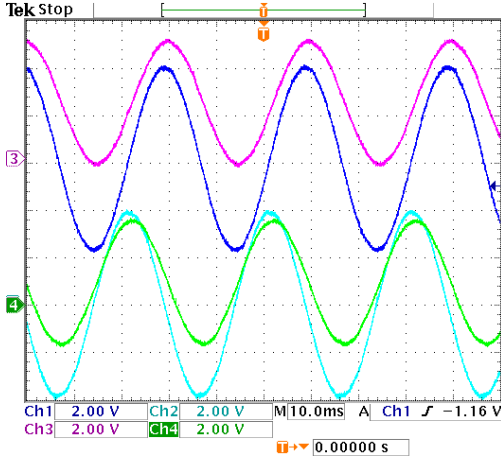
Simulation and practical experiments are performed in order to verify the theory presented in this section. Since the machine model used in the simulation and the parameters chosen for the estimator match each other perfectly, and non-modeled inverter effects as well as all other non-modeled effects do not come into play, the simulation shows that this estimator is able to work also at very low speed. Simulation results are not shown here.

The first problem encountered in practice is the integrator drift, when no compensation is provided. In Fig. 9.2(a) the estimated flux linkages in the stationary reference frame from the LUTs and from the back-EMF integration are shown. It is clear that the flux linkage estimation from the LUTs ( $\hat{\psi}_{sL}$ ) has no offset, and that the flux linkage estimate from the back-EMF integration ( $\hat{\psi}_s$ ) does have offset. It can also be noted that the magnitudes are not equal, i.e.  $\hat{\psi}_{sL} \neq \hat{\psi}_s$ .

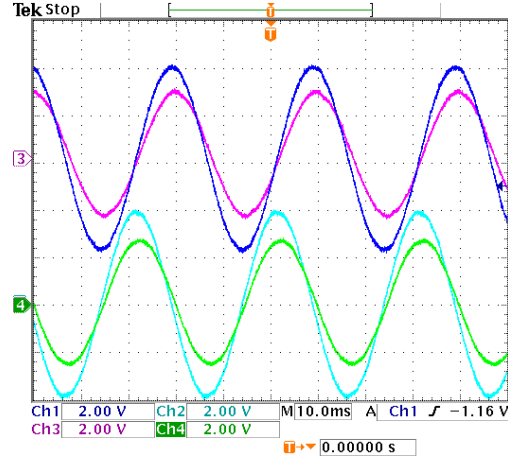
By setting the gain  $K_3$  to a small value, e.g.  $K_3 = 2$  rad/sec, the drift problem is solved, as shown in Fig. 9.2(b). Note that the idea is not to force the magnitude of  $\hat{\psi}_s$  to be equal to that from the LUTs  $\hat{\psi}_{sL}$  - in fact, we are not interested in the magnitude, but only in the

phase information since we are aiming at estimating the rotor position.

Ch1	$\hat{\psi}_{\alpha L}$	0.4	V.s/div
Ch2	$\hat{\psi}_{\beta L}$	0.4	V.s/div
Ch3	$\hat{\psi}_{\alpha}$	0.4	V.s/div
Ch4	$\hat{\psi}_{\beta}$	0.4	V.s/div
Time	$t$	10	ms/div



(a) No drift compensation.



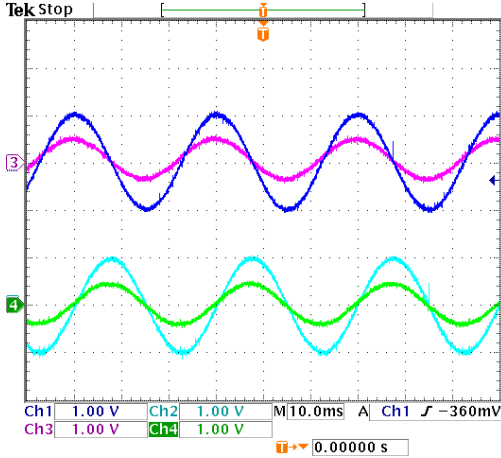
(b) With drift compensation.

Figure 9.2: Flux linkage estimation based on back-EMF.

Now with the drift problem solved, there is still the issue that the flux linkage magnitudes are not the same, i.e. the prediction from the LUT is not the same as the amount integrated from the back-EMF, as shown in Fig. 9.2(b). Also, the signals are not exactly in phase. Since we are only interested in the phase information, we continue and calculate the cos and sin of the angle, as in equations (9.9) and (9.10), by taking the dot and cross products of the estimated  $dq$  flux linkage from the LUTs and the estimated  $\alpha\beta$  flux linkage from the integral of the estimated back-EMF. These are compared to the cos and sin of the measured position, as shown in 9.3. Using the atan2 function, the estimated rotor position can be calculated from  $\hat{\psi}_r \hat{\psi}_s \cos \hat{\theta}_r$  and  $\hat{\psi}_r \hat{\psi}_s \sin \hat{\theta}_r$ . The estimated and measured positions are shown in Fig. 9.4 for comparison.

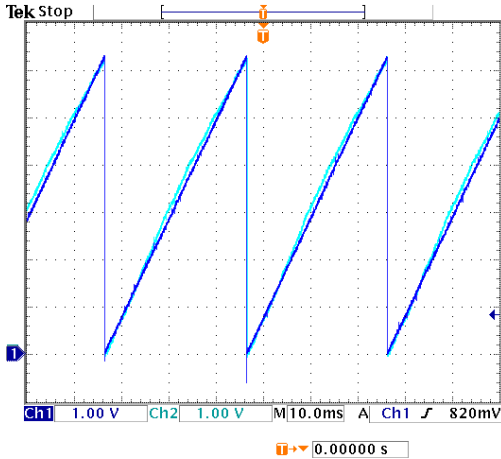
The rotor position estimation using a fundamental model based estimator seems to work, but only for a certain amount of flux linkage and speed. There are methods to improve this estimator, e.g. dead-time compensation and stator resistance estimation. Some researchers have suggested a similar estimator, but with added HF signal assistance [112, 36]. In the next section, position estimation by HF signals only are examined. Then the combined or hybrid structures are discussed.

For interest's sake, the observer structure shown in Fig. 9.1 was used to repeat the test discussed in section 3.3, i.e. to compare practically obtained flux linkages with the results from FE analysis. The experiment was performed under the same conditions, i.e. the speed



Ch1	$\cos \hat{\theta}_r$	1	const/div
Ch2	$\sin \hat{\theta}_r$	1	const/div
Ch3	$\hat{\psi}_r \hat{\psi}_s \cos \hat{\theta}_r$	0.4	$V^2 \cdot s^2 / \text{div}$
Ch4	$\hat{\psi}_r \hat{\psi}_s \sin \hat{\theta}_r$	0.4	$V^2 \cdot s^2 / \text{div}$
Time	$t$	10	ms/div

Figure 9.3: Measured vs. estimated cos and sin



Ch1	$\theta_r$	1	rad/div
Ch2	$\hat{\theta}_r$	1	rad/div
Time	$t$	10	ms/div

Figure 9.4: Measured vs. estimated rotor position

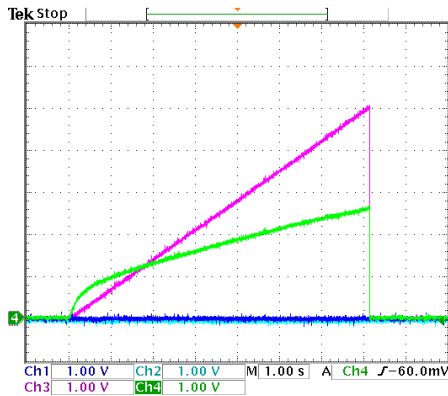
of the load machine was controlled to be high and constant, while the current vector of the RSM was controlled from zero to rated current along the  $q$ -axis,  $d$ -axis for  $\phi_r = 60^\circ$ . The simulation and practical results obtained with the flux observer structure is shown in Fig. 9.5. These results can be compared directly with the results shown in Fig. 3.14.

## 9.2 Position estimation using additional HF signals

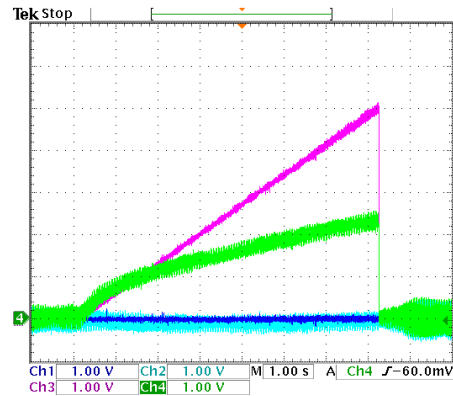
The electrical rotor position  $\theta_r$  may be obtained by applying an additional HF voltage, superimposed on the fundamental control voltages, and using the resulting HF currents in a demodulation scheme [19, 5, 22, 23, 82, 27, 83, 84, 7, 88, 4, 89, 10, 35, 11, 12, 93, 94, 14, 95, 64, 13, 97, 100, 101, 36, 114, 102, 103, 105, 106, 108, 31, 32, 109, 111, 112, 55, 113]. One major requirement is the presence of a magnetic saliency (anisotropy) that is spatially positioned related to the rotor position. The HF current is amplitude modulated by such a saliency and therefore the saliency position (anisotropy position)  $\theta_A$  may be found by an appropriate demodulation scheme. Under ideal circumstances  $\theta_r = \theta_A$ .

However, since the machine is not designed to be a resolver, the non-linear effects such as

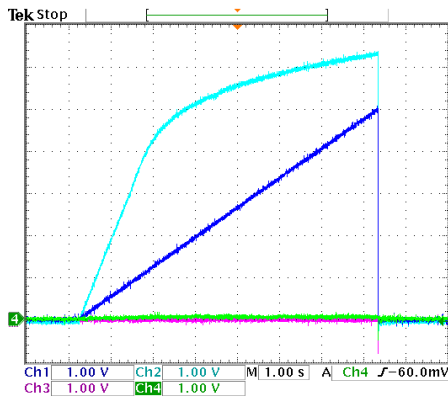
Ch1	$i_d$	1	A/div
Ch2	$\psi_d$	0.2	V.s/div
Ch3	$i_q$	1	A/div
Ch4	$\psi_q$	0.2	V.s/div
Time	$t$	1	s/div



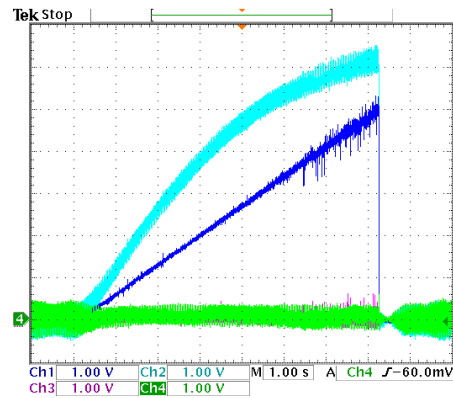
(a) Zero to rated current for  $\phi_r = 90^\circ$ : sim



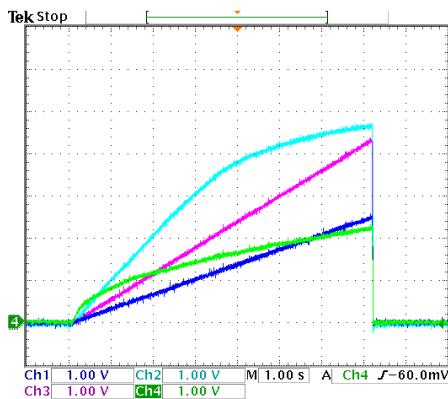
(b) Zero to rated current for  $\phi_r = 90^\circ$ : prac



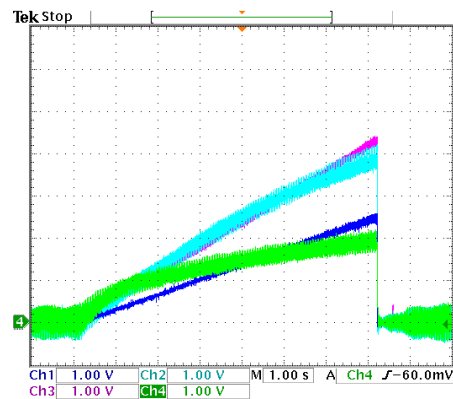
(c) Zero to rated current for  $\phi_r = 0^\circ$ : sim



(d) Zero to rated current for  $\phi_r = 0^\circ$ : prac



(e) Zero to rated current for  $\phi_r = 60^\circ$ : sim



(f) Zero to rated current for  $\phi_r = 60^\circ$ : prac

Figure 9.5: Fundamental model: simulation vs. practical using observer structure

saturation, cross-coupling and flux linkage variation with varying rotor position affects the rotor position estimation heavily. Parameter sensitivity could be a problem. A good property for any control system or estimation scheme is robustness. A position and speed estimation scheme that is parameter independent is of-course the ultimate goal. The fundamental flux linkage has a great influence on the HF parameters, as shown in section 3.4: saturation within the machine causes a reduction in inductance and could even cause an inductance swop in the  $dq$  reference frame. Mutual coupling causes an offset error in rotor position estimation, as stressed by [36]. Flux linkage variation, and consequently inductance (including mutual inductance) variation, during rotation, causes a time-varying (position dependent) error in the position estimation [57, 32, 55]. These problems are explained in detail further on in the chapter.

To start with, an ideal machine model (constant anisotropy model with no mutual inductance) is given and is used to derive two possible rotor position estimation schemes:

1. Rotating voltage vector in the stationary reference frame (like resolver)
2. Alternating voltage vector in the estimated reference frame (PLL)

Rotor speed estimation is also required, for speed control and also for the decoupling terms in the current vector controller. For phase locked loop (PLL) methods, speed estimation is an inherent part of the process. In open-loop methods, the speed estimation needs to be done separately. One speed estimation method is to differentiate the estimated rotor position and use a LPF to minimize the noise. Alternatively an observer structure may be used to estimate the speed, or Fourier Transform methods may also be used. Throughout this chapter, speed estimation is also considered.

### 9.2.1 Anisotropy model

The words “anisotropy” and “saliency” can be used equivalently. Anisotropy is modelled mathematically as a difference in inductance between two perpendicular axes. The model is given in equations (9.16) through (9.18), with the subscript  $A$  to indicate that we are speaking about a general anisotropy.

$$u_{dA} = L_{dA} \frac{di_{dA}}{dt} \tag{9.16}$$

$$u_{qA} = L_{qA} \frac{di_{qA}}{dt} \tag{9.17}$$

$$L_{dA} \neq L_{qA} \tag{9.18}$$

### 9.2.2 Rotating HF voltage vector in the stationary reference frame

A popular method of finding the anisotropy position is to apply a rotating HF voltage vector in the stationary reference frame, to filter out the HF current vector from the stator current

and to use the information contained in the HF current signal to find the anisotropy position. A mathematical derivation is given next to explain the method step-by-step.

First of all, a rotating HF voltage vector is superimposed on the fundamental control voltages. The HF voltage that is added is given as in equation (9.19). This HF rotating voltage, as seen within a reference frame that is aligned with the anisotropy position  $\theta_A$  is given in (9.20). According to the anisotropy model as in equations (9.16) through (9.18), the current in the anisotropy reference frame is given as in (9.21) (note that this is only the HF content of the stator current). Now if we make the assumption that the speed at which the anisotropy is moving  $\dot{\theta}_A$  is close to zero, or we assume that  $\omega_{HF} \gg \dot{\theta}_A$ , then equation (9.21) can be approximated as (9.22). However, it should be noted that this approximation cannot be justified completely.

Since there is only access to the stator current in the stationary reference frame, equation (9.22) must be transformed back into the stationary reference frame as in (9.23). It is noted that the mathematics involved is rated complicated.

$$\vec{u}_{sHF}^* = U_{HF} \cdot e^{j\omega_{HF}t} \quad (9.19)$$

$$\begin{aligned} \vec{u}_A &= \vec{u}_{sHF}^* e^{-j\theta_A} \\ &= U_{HF} e^{j(\omega_{HF}t - \theta_A)} \end{aligned} \quad (9.20)$$

$$\vec{i}_A = \int \left( \frac{U_{HF}}{L_{dA}} \cos(\omega_{HF}t - \theta_A) \right) dt + j \int \left( \frac{U_{HF}}{L_{qA}} \sin(\omega_{HF}t - \theta_A) \right) dt \quad (9.21)$$

$$\approx \frac{U_{HF}}{\omega_{HF}} \left( \frac{\cos(\omega_{HF}t - \theta_A)}{L_{dA}} + j \frac{\sin(\omega_{HF}t - \theta_A)}{L_{qA}} \right) \quad (9.22)$$

$$\begin{aligned} \vec{i}_s &= \vec{i}_r e^{j\theta_A} \\ &= \frac{U_{HF}}{\omega_{HF}} \left( \frac{\cos(\omega_{HF}t - \theta_A)}{L_{dA}} + j \frac{\sin(\omega_{HF}t - \theta_A)}{L_{qA}} \right) (\cos \theta_A + j \sin \theta_A) \\ &= \frac{U_{HF}}{\omega_{HF}} \left( \frac{\cos(\omega_{HF}t - \theta_A) \cos \theta_A - \sin(\omega_{HF}t - \theta_A) \sin \theta_A}{L_{dA}} - \frac{\sin(\omega_{HF}t - \theta_A) \sin \theta_A}{L_{qA}} \right) \dots \\ &\dots + j \frac{U_{HF}}{\omega_{HF}} \left( \frac{\cos(\omega_{HF}t - \theta_A) \sin \theta_A + \sin(\omega_{HF}t - \theta_A) \cos \theta_A}{L_{dA}} + \frac{\sin(\omega_{HF}t - \theta_A) \cos \theta_A}{L_{qA}} \right) \\ &= \frac{U_{HF}}{\omega_{HF}} \left( \frac{\cos(\omega_{HF}t - 2\theta_A) + \cos \omega_{HF}t}{2L_{dA}} - \frac{\cos(\omega_{HF}t - 2\theta_A) - \cos \omega_{HF}t}{2L_{qA}} \right) \dots \\ &\dots + j \frac{U_{HF}}{\omega_{HF}} \left( \frac{\sin \omega_{HF}t - \sin(\omega_{HF}t - 2\theta_A)}{2L_{dA}} + \frac{\sin \omega_{HF}t + \sin(\omega_{HF}t - 2\theta_A)}{2L_{qA}} \right) \\ &= \frac{U_{HF}}{2\omega_{HF}} \left[ \cos(\omega_{HF}t - 2\theta_A) \left( \frac{1}{L_{dA}} - \frac{1}{L_{qA}} \right) + \cos(\omega_{HF}t) \left( \frac{1}{L_{dA}} + \frac{1}{L_{qA}} \right) \right] \dots \\ &\dots + j \frac{U_{HF}}{2\omega_{HF}} \left[ \sin(\omega_{HF}t) \left( \frac{1}{L_{dA}} + \frac{1}{L_{qA}} \right) - \sin(\omega_{HF}t - 2\theta_A) \left( \frac{1}{L_{dA}} - \frac{1}{L_{qA}} \right) \right] \\ &= \frac{U_{HF}}{2\omega_{HF}} \left[ \left( \frac{1}{L_{dA}} - \frac{1}{L_{qA}} \right) e^{-j(\omega_{HF}t - 2\theta_A)} + \left( \frac{1}{L_{dA}} + \frac{1}{L_{qA}} \right) e^{j\omega_{HF}t} \right] \end{aligned} \quad (9.23)$$



### Open-loop demodulation.

The anisotropy position may be found from the stator current, given in (9.23), by filtering out and demodulating the HF content, as in equations (9.24) and (9.25). There is still some post-processing needed to obtain  $\theta_A$  from  $2\theta_A$ . Once  $\theta_A$  is obtained, it is also possible to determine the anisotropy speed by direct differentiation of the position signal, and low-pass filtering to remove noise, as in (9.26). As mentioned, other methods could also be used to estimate the speed.

$$\vec{i}_{HF} = \frac{U_{HF}}{2\omega_{HF}} \left( \frac{1}{L_{dA}} - \frac{1}{L_{qA}} \right) e^{j2\theta_A} \approx \text{LPF}\{\vec{i}_s e^{j\omega_{HF}t}\} \quad (9.24)$$

$$2\theta_A = \tan^{-1} \frac{\Re\{\vec{i}_{HF}\}}{\Im\{\vec{i}_{HF}\}} \quad (9.25)$$

$$\omega_A = \text{LPF}\{\dot{\theta}_A\} \quad (9.26)$$

### Closed-loop demodulation.

An alternative method is to feed the signal  $\vec{i}_{HF}$  to a rotating vector tracker, i.e. a PLL structure, that will drive the estimated anisotropy speed until the estimated anisotropy position is in phase with the real anisotropy position. In that way, the anisotropy speed is tracked automatically.

To be clear, an error signal is built by taking the cross product of  $e^{2j\hat{\theta}_A}$  with the signal  $\vec{i}_{HF}$ , as in (9.27). This error is fed to a PI controller so that it will be driven to zero, thereby aligning  $\hat{\theta}_A$  with  $\theta_A$ . The output of the integrator branch of the PI controller is the estimated anisotropy speed as in (9.28), which is then added to an error-proportional term and integrated to get the estimated anisotropy position as in (9.29). The estimation block diagram is shown in Fig. 9.6.

$$\begin{aligned} \epsilon_A &= j e^{j\hat{\theta}_A} \cdot \vec{i}_{HF} \\ &= \frac{U_{HF}}{2\omega_{HF}} \left( \frac{1}{L_{dA}} - \frac{1}{L_{qA}} \right) \sin 2(\theta_A - \hat{\theta}_A) \end{aligned} \quad (9.27)$$

$$\hat{\omega}_A = K_i \int \epsilon_A dt \quad (9.28)$$

$$\hat{\theta}_A = \int (K_p \epsilon_A + \hat{\omega}_A) \quad (9.29)$$

### 9.2.3 Alternating HF voltage vector in the estimated anisotropy reference frame

Another popular method to obtain the anisotropy position is by superimposing a pulsating HF voltage vector in the estimated anisotropy reference frame on the fundamental control

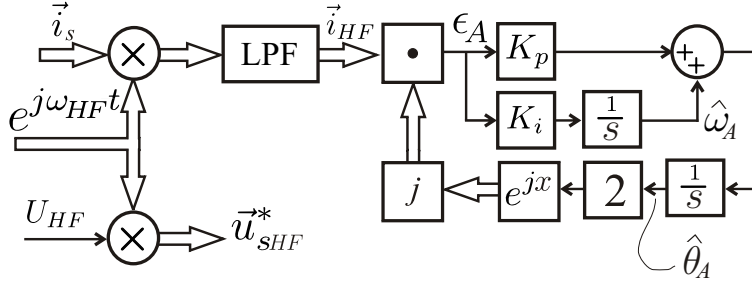


Figure 9.6: Position estimated based on rotating HF

voltage vector; then one must filter out the resulting HF current vector from the measured current, and find the saliency position information within the HF current that allows one to estimate the saliency position. Using the estimated saliency position, the rotor position can also be estimated, as has been described by numerous authors including [4, 32, 113]. Of course, we would like to use the inherent rotor saliency that is provided by physical rotor design [102, 15], so that the anisotropy position closely resembles the rotor position.

The estimation process is described mathematically, in easy to follow and logical steps, by (9.30) through (9.48) and is illustrated by the block diagram Fig. 9.7. The anisotropy position estimation takes place within a reference frame that is aligned with the anisotropy. A pulsating HF voltage is applied in an arbitrary direction  $\delta$ , as in (9.31), with respect to the estimated anisotropy position  $\hat{\theta}_A$ . The common choices are  $\delta = 0$  or  $\delta = \frac{\pi}{2}$ , although it has been suggested that the injection direction should resemble the maximum torque per ampere (MTPA) axis, in an effort to minimize the effect of inductance change due to saturation [104].

The HF voltage amplitude  $U_{HF}$  is usually chosen as constant and needs to be large enough to give a substantial HF current. If the machine has a very small inductance, then a small voltage amplitude causes a relatively large HF current. It has been suggested that the voltage amplitude be varied in an effort to reduce acoustic noise [106], so that it only has a high value during acceleration or high load.

The chosen frequency  $\omega_{HF}$  also largely influences the amplitude of the HF current and the acoustic noise, and needs to be selected so that digital filters can successfully separate the HF current from the fundamental current and so that the fundamental current vector controller does not influence the HF currents much, i.e. a certain amount of frequency separation is needed. In many papers and also in the author's experience  $\omega_{HF} = 2\pi 500$  [rad/sec] was a good choice for the machines at hand.

Following (9.30) and (9.31), the pulsating HF voltage in stationary reference frame is given by (9.32), and so the pulsating voltage in the reference frame aligned to the actual anisotropy at position  $\theta_A$  is given by (9.33). This pulsating voltage causes the HF current in the actual anisotropy reference frame as in (9.34).

Assuming a slowly varying error  $\tilde{\theta}_A$ , the HF current in the actual anisotropy reference frame may be approximated as in (9.35). This is a totally valid approximation if a PI controller is used to drive the error  $\tilde{\theta}_A$  to zero. This estimation algorithm is not restricted

to very low rotor speeds and can work up to high speed.

However, since we do not know  $\theta_A$  and only have access to  $\hat{\theta}_A$ , we need to find the expression for the HF current in the estimated anisotropy reference frame, as in (9.36). The useful information, i.e. the modulated amplitude of  $\vec{i}_{\hat{A}}$ , is expressed by (9.37).

$$\vec{u}_{HF} = U_{HF} \cos(\omega_{HF}t) + j0 \quad (9.30)$$

$$\vec{u}_{\hat{A}} = \vec{u}_{HF} e^{j\delta} \quad (9.31)$$

$$\vec{u}_{sHF} = \vec{u}_{\hat{A}} e^{j\hat{\theta}_A} \quad (9.32)$$

$$\vec{u}_A = \vec{u}_{sHF} e^{-j\theta_A} = \vec{u}_{\hat{A}} e^{-j\tilde{\theta}_A} \quad (9.33)$$

$$\tilde{\theta}_A = \theta_A - \hat{\theta}_A$$

$$\begin{bmatrix} i_{dA} \\ i_{qA} \end{bmatrix} = \begin{bmatrix} L_{dA} & 0 \\ 0 & L_{qA} \end{bmatrix}^{-1} \begin{bmatrix} \int u_{dA} dt \\ \int u_{qA} dt \end{bmatrix} \quad (9.34)$$

$$\vec{i}_A \approx \vec{\psi}_{HF} \left( \frac{1}{L_{dA}} \cos \tilde{\theta}_A - j \frac{1}{L_{qA}} \sin \tilde{\theta}_A \right) \quad (9.35)$$

$$\vec{\psi}_{HF} = \frac{U_{HF}}{\omega_{HF}} \sin(\omega_{HF}t + \zeta) e^{j\delta}$$

$$\vec{i}_{\hat{A}} = \vec{i}_A e^{j\hat{\theta}_A} = \vec{\psi}_{HF} \vec{A} \quad (9.36)$$

$$\vec{A} = \left( \frac{1}{\Sigma L} + \frac{1}{\Delta L} e^{j2\tilde{\theta}_A} \right) \quad (9.37)$$

$$\Sigma L = 2 \frac{L_{qA} \cdot L_{dA}}{L_{qA} + L_{dA}}$$

$$\Delta L = 2 \frac{L_{qA} \cdot L_{dA}}{L_{qA} - L_{dA}}$$

### Closed-loop demodulation using alternating HF current vector in the estimated reference frame

The superposition of the HF voltage vector onto the fundamental control voltage vector, as in (9.38) results in a HF current vector that can be separated from the fundamental current vector with a band pass filter (BPF), as in (9.39). We are only interested in the useful information given by  $\vec{A}$  and can get this from  $\vec{i}_{\hat{A}}$  using the demodulation given in (9.40). The demodulation sine wave  $F_{dem}$ , as in (9.41), has the phase shift  $\zeta$ , which should be zero in theory. In practice the phase shift between HF voltage and HF current could be larger than  $90^\circ$  due to digital system delays. In the demodulation it is therefore important to check that the HF current and the demodulation sine wave  $F_{dem}$  is in phase, by setting  $\zeta$  to an appropriate value.

Now, using the imaginary part of  $\vec{A}$  as in (9.42), as the input signal to a PI controller, i.e. driving this signal to zero, we can assume that  $\tilde{\theta}_A$  will be small and (9.43) becomes valid. Therefore, in this closed loop tracking system (see Eqs. (9.44), (9.45) and (9.46)), or phase locked loop (PLL), we can be sure to track the anisotropy position, and the speed at

which it moves, wherever it may be. Important is the normalization with the constant  $\Delta L$  in (9.42) and the sign that it has, since negative feedback (stability) has to be ensured.

As the final step, we may estimate the rotor position  $\theta_r$  from our estimated anisotropy position  $\hat{\theta}_A$  as in (9.47), and in the ideal case  $\theta_{comp}$  is zero or a constant. We can also estimate the rotor speed using our estimated anisotropy speed, as in (9.48). Since  $\hat{\omega}_A$  is used in part to drive the integrator so that the anisotropy position is tracked, and therefore might have large and fast changes, we might need additional low pass filtering to obtain a reasonable rotor speed estimation.

$$\vec{u}_s^* = \vec{u}_{s1}^* + \vec{u}_{sHF} \quad (9.38)$$

$$\vec{i}_{\hat{A}} = \text{BPF} \left\{ \vec{i}_s e^{-j\hat{\theta}_A} \right\} \quad (9.39)$$

$$\vec{A} = \text{LPF} \left\{ \vec{i}_{\hat{A}} e^{-j\delta} \cdot F_{dem} \right\} \quad (9.40)$$

$$F_{dem} = 2 \frac{\omega_{HF}}{U_{HF}} \sin(\omega_{HF} t + \zeta) \quad (9.41)$$

$$\sin(2\tilde{\theta}_A) = (\Delta L) \Im m \left\{ \vec{A} \right\} \quad (9.42)$$

$$2\tilde{\theta}_A \approx \sin(2\tilde{\theta}_A) \quad (9.43)$$

$$\tilde{\theta}_A = \theta_A - \hat{\theta}_A \quad (9.44)$$

$$\hat{\omega}_A = K_i \int \tilde{\theta}_A dt \quad (9.45)$$

$$\hat{\theta}_A = \int (K_p \tilde{\theta}_A + \hat{\omega}_A) dt \quad (9.46)$$

$$\hat{\theta}_r = \hat{\theta}_A + \theta_{comp} \quad (9.47)$$

$$\hat{\omega}_r = \text{LPF} \left\{ \hat{\omega}_A \right\} \quad (9.48)$$

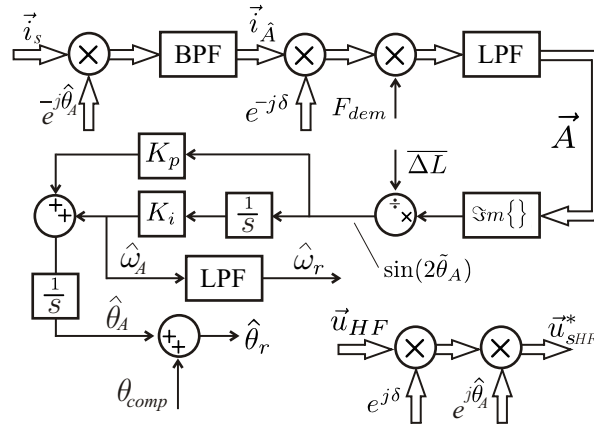


Figure 9.7: Position estimated based on alternating HF

### 9.2.4 Simulation and practical tests

The following simulation and practical results were performed to test and evaluate the performance of the rotor position estimation schemes using the scheme with rotating HF voltage

excitation in the stationary reference frame, and the scheme with alternating HF voltage excitation in the estimated anisotropy reference frame.

### **Rotating HF voltage excitation in the stationary reference frame**

The first test is to evaluate the position estimation performance for different speeds and constant the load (the load is zero, but a small amount of  $q$ -axis current is applied to the RSM to saturate the  $q$ -axis). The detected anisotropy position is compared to the measured rotor position in each case, and the phase difference is studied. Only practically measured results are shown here in Fig. 9.8, i.e. no simulation was performed. From the measurements it is noted that as the speed increases, the phase difference between the measured rotor position and the estimated anisotropy position also increases, i.e. this estimation process is speed dependent. This could have been predicted following the mathematical derivation, where it was assumed that the rotor speed is close to zero, or the high frequency is much higher than the fundamental frequency - in this case where the HF is 500 Hz, the assumption is obviously not valid.

The second test is to evaluate the position estimation under varying load. The speed is kept constant, while the load is increased. The measured rotor position is compared to the detected anisotropy position, as shown in Fig. 9.9, and the phase difference is studied. It is clear that the phase difference decreases under loaded conditions. Therefore the detected anisotropy position is also load dependent.

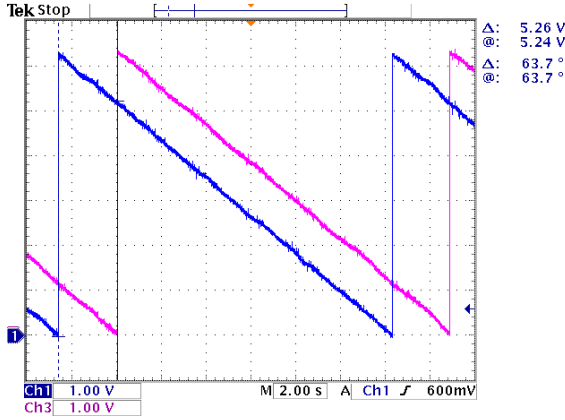
Following the results shown in Figs. 9.8 and 9.9, it is concluded that the anisotropy position estimation using rotating HF voltage excitation in the stationary reference frame is speed and load dependent, and therefore not suitable to be used for rotor position estimation.

### **Alternating HF voltage excitation in the estimated reference frame**

The first test is to evaluate the position estimation performance for different speeds and constant load (the load is zero, but a small amount of  $q$ -axis current is applied to the RSM to saturate the  $q$ -axis). The detected anisotropy position is compared to the measured rotor position in each case, and the phase difference is studied. Only practical results are shown here in Fig. 9.10, i.e. no simulation is performed. From the measurements it is clear that the phase difference is fairly constant and in each case close to 90 degrees, i.e. the saturated  $q$ -axis is detected.

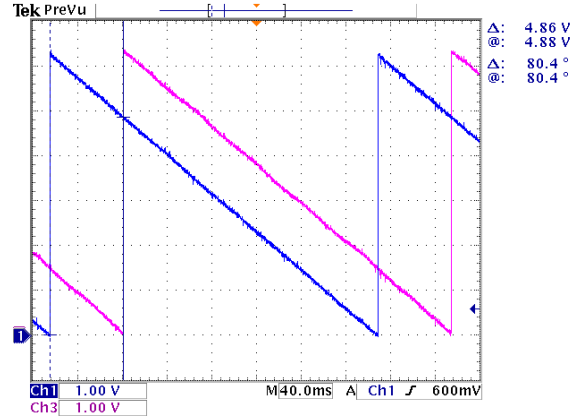
The second test is to evaluate the position estimation under varying load. The speed is kept constant, while the load is increased. The measured rotor position is compared to the detected anisotropy position, as shown in Fig. 9.11, and the phase difference is studied. It is clear that the phase difference increases under loaded conditions. Therefore the detected anisotropy position is load dependent. It is also noted that the detected anisotropy position becomes distorted under loaded conditions - the reason might be that higher order anisotropies are detected.

Ch1	$\theta_r$	1	rad/div
Ch3	$\theta_A$	1	rad/div
Time	$t$	2	s/div



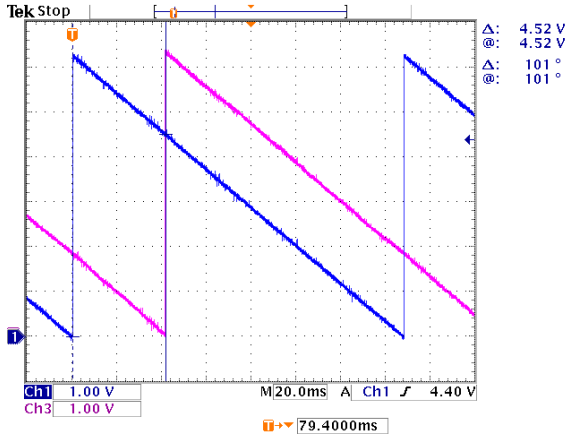
(a) Load = 0 Nm, Speed = 1 rpm

Ch1	$\theta_r$	1	rad/div
Ch3	$\theta_A$	1	rad/div
Time	$t$	40	ms/div



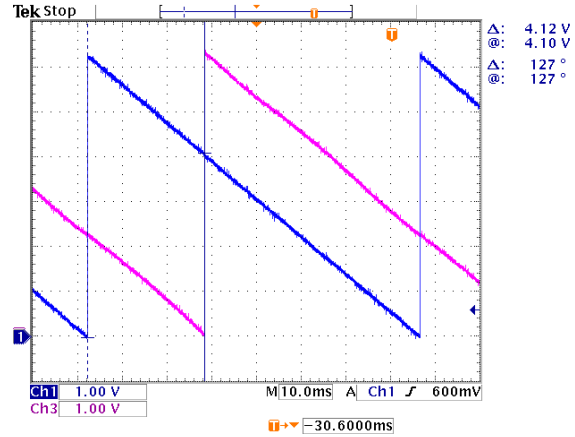
(b) Load = 0 Nm, Speed = 102 rpm

Ch1	$\theta_r$	1	rad/div
Ch3	$\theta_A$	1	rad/div
Time	$t$	20	ms/div



(c) Load = 0 Nm, Speed = 202 rpm

Ch1	$\theta_r$	1	rad/div
Ch3	$\theta_A$	1	rad/div
Time	$t$	10	ms/div



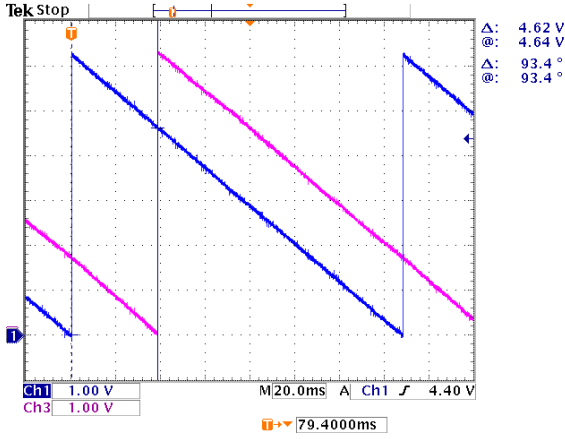
(d) Load = 0 Nm, Speed = 402 rpm

Figure 9.8: Rotating HF observer: speed dependence test.

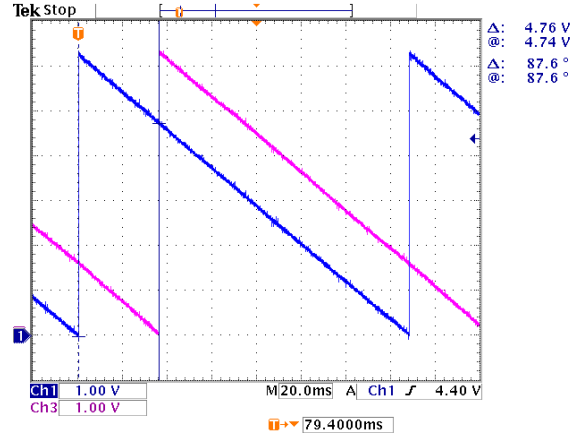
It is concluded that the anisotropy position detection using alternating HF voltage excitation is not speed dependent, but definitely load dependent and under loaded conditions the position signal unfortunately becomes rather distorted.

To confirm that it is really the saturated  $q$ -axis that is detected, a third test is performed. Firstly no fundamental current at all is applied, then positive  $i_q$  and then negative  $i_q$ . Each time the detected anisotropy position is compared to the measured rotor position, as shown in Fig. 9.12. The speed is kept constant at 200 rpm. For the case where there is no fundamental current in the machine Fig. 9.12(a), the  $q$ -axis is still unsaturated and it must be only the geometric anisotropy that is being detected. In Fig. 9.12(b) the positive  $q$ -axis

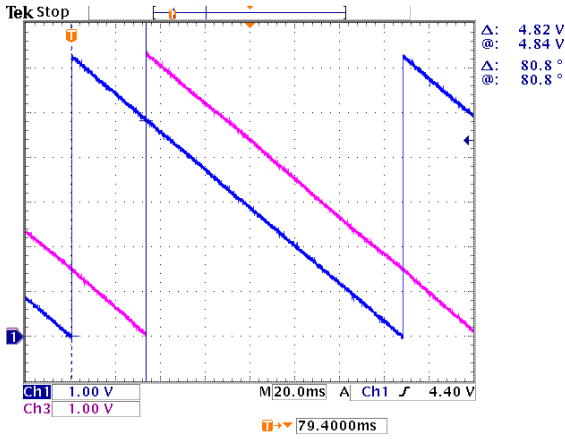
Ch1	$\theta_r$	1	rad/div
Ch3	$\theta_A$	1	rad/div
Time	$t$	20	ms/div



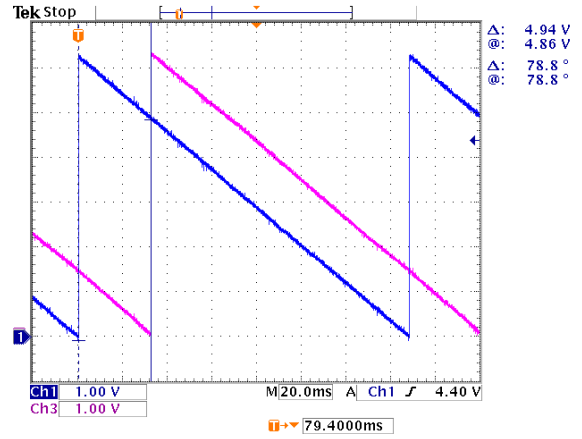
(a) Load = 3 Nm, Speed = 202 rpm



(b) Load = 5 Nm, Speed = 202 rpm



(c) Load = 8 Nm, Speed = 202 rpm



(d) Load = 10 Nm, Speed = 202 rpm

Figure 9.9: Rotating HF observer: load dependence test.

is saturated and it is this saturation anisotropy that is detected, as can be confirmed from the result, since  $\hat{\theta}_A$  leads  $\theta_r$  by 90 degrees. In Fig. 9.12(c) the negative  $q$ -axis is saturated and it is this saturation anisotropy that is detected, as can be confirmed from the result, since  $\hat{\theta}_A$  lags  $\theta_r$  by 90 degrees.

So it is clear that it is the saturation anisotropy that is detected in the RSM, which is rather surprising, since one would think that the geometric anisotropy is very strong. Therefore, once the  $q$ -axis is saturated, it can be successfully detected by the scheme with alternating HF voltage excitation. As the load increases however, the  $d$ -axis is also saturated to a certain extent, and due to mutual coupling, the saturation anisotropy position moves away from the  $q$ -axis towards the  $d$ -axis. It is clear that the difference between the actual rotor position and the detected anisotropy position has an offset component that is load dependent, but also a time-varying or rather position-varying component. The fourth test

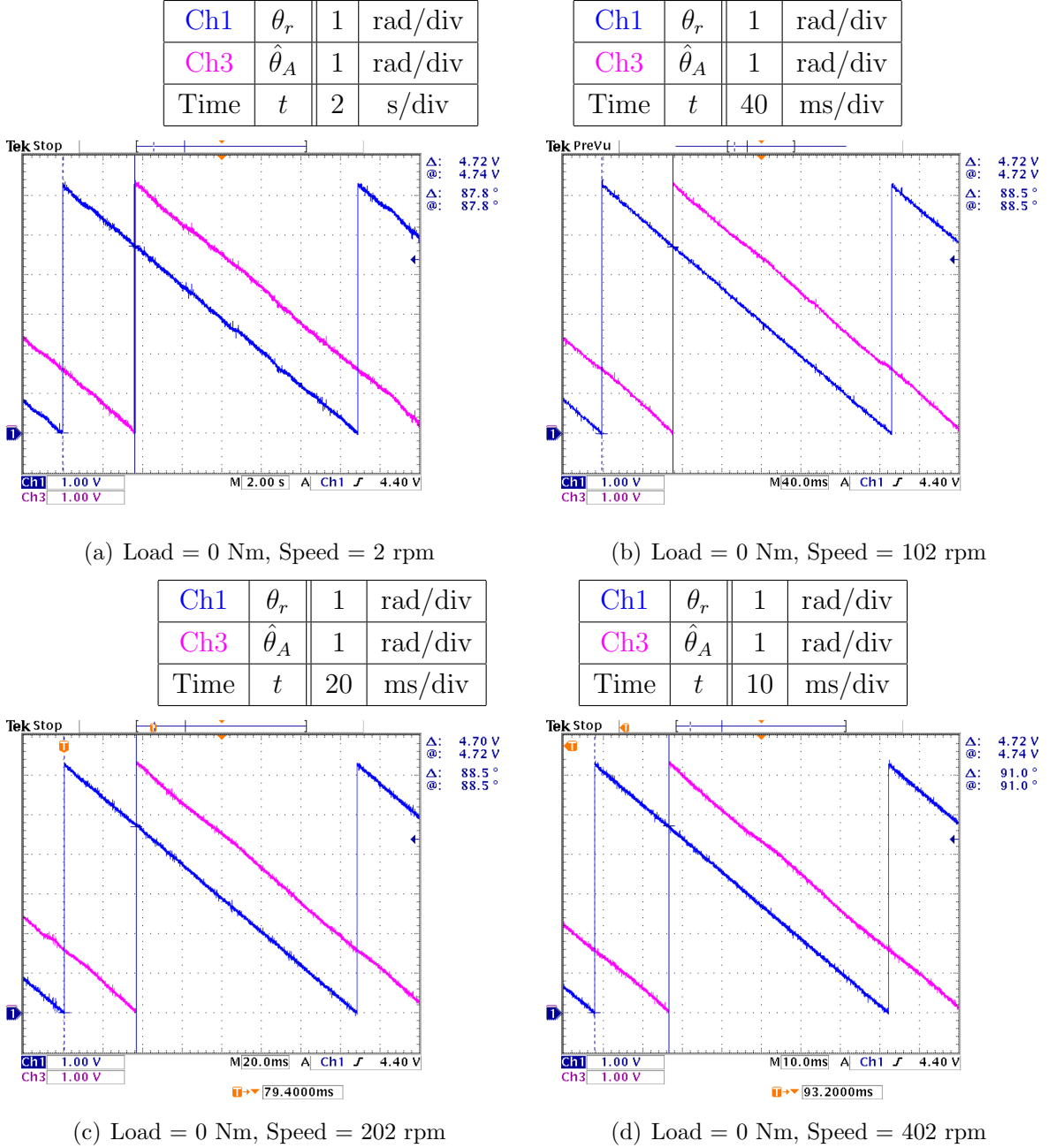


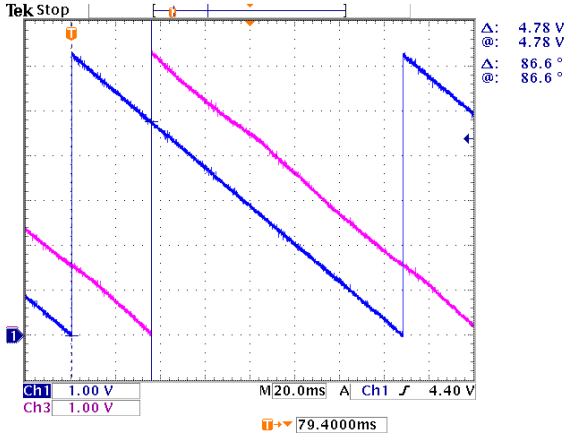
Figure 9.10: Alternating HF observer: speed dependence test.

studies this phase difference in detail and the results are shown in Fig. 9.13. In this figure the torque reference, estimated torque, current magnitude and anisotropy position deviation from the  $q$ -axis are shown, for a constant speed of 200 rpm at different load levels. The results for positive load are shown in Figs. 9.13(a) through 9.13(e); the results for negative torque is symmetrical to the results for positive torque and are therefore not shown here. The summarized result for the offset error is shown in Fig. 9.13(f), where the actual measurements are shown with one line and Matlab curve fitting was used to obtain an equation for the measured curve, which in turn was used to plot the fitted curve.

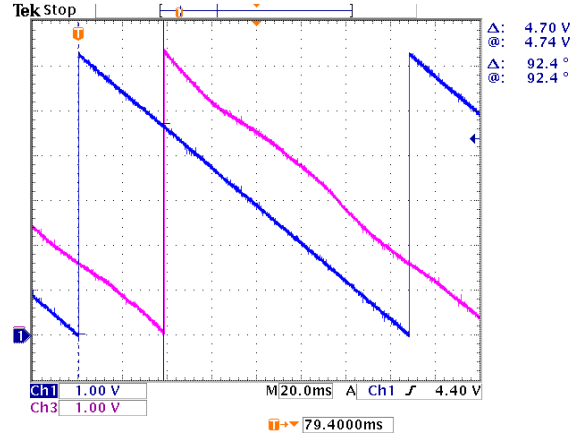
It is noted that this offset error increases with load, but also that the shape of the



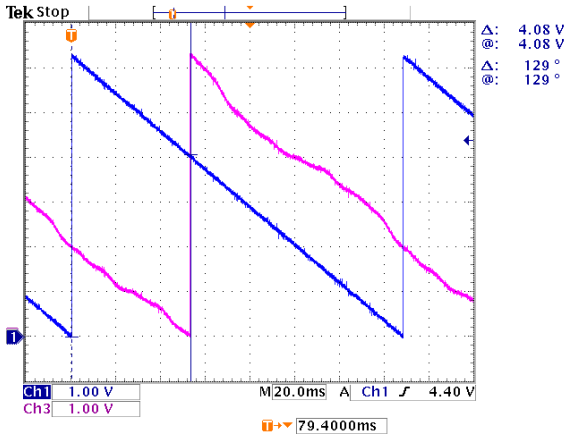
Ch1	$\theta_r$	1	rad/div
Ch3	$\hat{\theta}_A$	1	rad/div
Time	$t$	20	ms/div



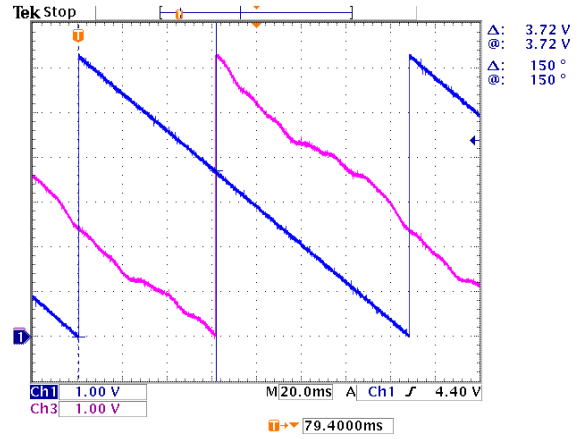
(a) Load = 3 Nm, Speed = 202 rpm



(b) Load = 5 Nm, Speed = 202 rpm



(c) Load = 8 Nm, Speed = 202 rpm



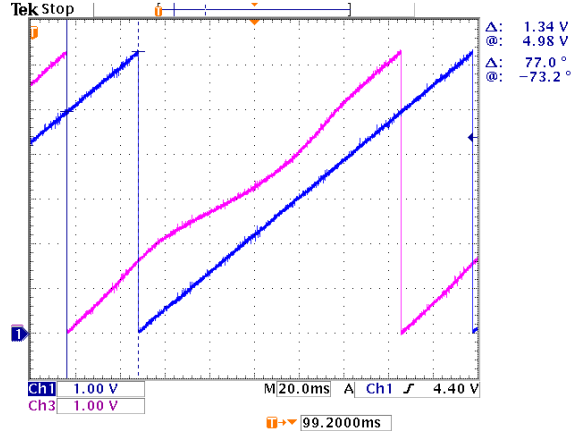
(d) Load = 10 Nm, Speed = 202 rpm

Figure 9.11: Alternating HF observer: load dependence test.

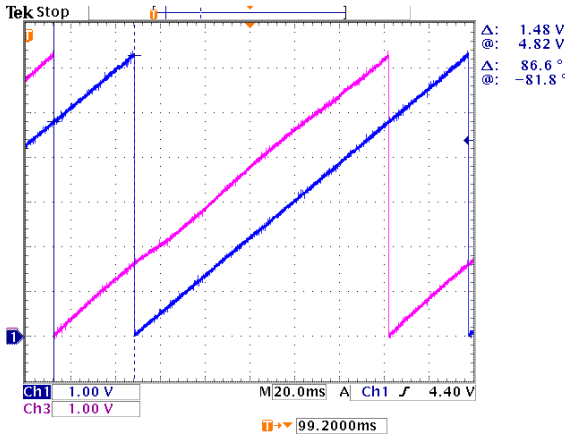
position varying error changes with load. This offset error can be compensated, but it is very difficult to compensate the position varying error. The offset error can be explained by mutual inductance, and the position varying error is there due to higher order anisotropies that are not considered in the simple anisotropy model.

The next step therefore is to compensate the load dependent offset error in the rotor position estimation. It has been shown that the compensation can be placed at the final stage of the estimation, as shown in Fig. 9.7 using the  $\theta_{comp}$ . These results have been published for this RSM [32], and also for a PMSM [57] [article in German], and a comparison has also been made [55]. By doing the compensation in that way, the anisotropy position detection is separate from the field orientated control, in other words there is the detected anisotropy position on the one hand and the estimated rotor position on the other hand. The problem then is that it is difficult to combine this position estimator with the fundamental model

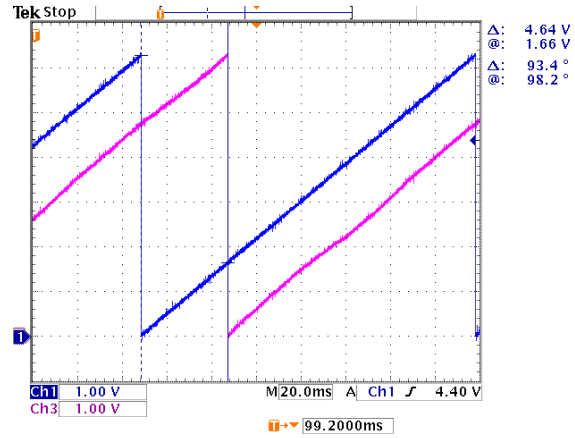
Ch1	$\theta_r$	1	rad/div
Ch3	$\hat{\theta}_A$	1	rad/div
Time	$t$	20	ms/div



(a)  $i_q = 0$  A, Speed = 200 rpm



(b)  $i_q = 2$  A, Speed = 200 rpm



(c)  $i_q = -2$  A, Speed = 200 rpm

Figure 9.12: Alternating HF observer: detected position

based position estimator, since there are two angles to consider the whole time.

It has been found and is shown for the first time in this work, i.e. this is not published yet, that the offset error compensation can also be done by changing the HF voltage injection direction, i.e. by changing the angle  $\delta$  as shown in Fig. 9.7 as a function of the load according to Fig. 9.13(f). If this is done, the compensation  $\theta_{comp}$  falls away and the rotor position is estimated directly.

In the following results shown in Fig. 9.14, the fundamental current is controlled using the estimated rotor position, i.e. sensorless control is performed. The time scale is increased, i.e. the results are shown for a longer period of time, at constant speed and for different load levels. It is illustrated that the position estimation is accurate for positive as well as negative torque. There is almost no offset error at any load, but the position varying error is still clearly visible. This estimator is not capable of eliminating the position varying error, since it is tracking higher order anisotropies that are present within the machine, but are not present in the simplified anisotropy model.

Nevertheless, it is possible to control the RSM from zero to fairly high speed, from zero up to rated load, using this position estimator. If there was no voltage limitation due to limited

DC bus voltage, the scheme could probably work up to very high speeds, depending on the bandwidth of the PLL. However, the position varying error is a serious problem and needs to be addressed. It is suspected, that an estimator structure that employs neural networks, or learning capability, might be able to deal with this problem, but of course much further research is necessary.

All the tests shown have been in the steady state. One dynamic test will be shown to prove that a torque reversal step can be applied using sensorless control. The result is shown in Fig. 9.15. The experiment is performed at zero speed. The load step is from half the rated load negative to half the rated load positive. The maximum position error obtained is 10 degrees.

### 9.2.5 HF machine model including mutual inductance

The load dependent phase error between the detected anisotropy position and the actual rotor position can be explained mathematically by introducing load dependent mutual inductance into the anisotropy model. As shown in the high frequency machine model identification practical measurements Fig. 3.15, there is indeed mutual inductance. The significance thereof is clear for the sensorless control scheme using alternating HF voltage excitation: by injecting HF voltage in the  $d$ -axis and expecting only to find  $|i_{dHF}|$ , one would normally drive  $|i_{qHF}|$  to zero in order to align the estimated and actual  $dq$  reference frames [4]; in this case it is predicted that this method will result in an estimation error, since a large part of  $|i_{qHF}|$  is due to cross-coupling and not due to misalignment of the reference frames.

Other researchers also stress this idea [36], where an equation is given for the error that is made by the HF excitation based estimation schemes. This equation is given in (9.49), where the symbol  $L_{dq}$  denotes mutual inductance, instead of the  $M$  symbol previously used. The symbols  $L_d$  and  $L_q$  are the  $d$ -axis and  $q$ -axis tangential inductances, as previously used, but without the  $t$  subscript. In [36] the authors make no distinction between high frequency tangential inductances and fundamental model tangential inductances. It probably depends on the machine and the chosen frequency for the HF voltage excitation: in the case studied this work and the results presented in Fig. 3.15, there is a difference. This is still a point of discussion and further research is necessary.

$$\theta_r - \hat{\theta}_r = \frac{1}{2} \tan^{-1} \frac{2L_{dq}}{L_d - L_q} \quad (9.49)$$

In this section, equation (9.49) is derived by introducing mutual inductance in the anisotropy model, as in equations (9.50) and (9.51). Now, the HF excitation voltage that is applied in the estimated reference frame in an arbitrary direction  $\alpha$  as in (9.52), can be transformed to the actual  $dq$ -reference frame as in (9.53). The vector  $\vec{u}_r$  is given in its  $d$  and  $q$  components in equations (9.54) and (9.55) respectively.

$$u_d \approx L_d \frac{di_d}{dt} + L_{dq} \frac{di_q}{dt} \quad (9.50)$$

$$u_q \approx L_{dq} \frac{di_d}{dt} + L_q \frac{di_q}{dt} \quad (9.51)$$

$$\vec{u}_r = U_{HF} \cos(\omega_{HF}t) e^{j\hat{\alpha}} \quad (9.52)$$

$$\vec{u}_r = U_{HF} \cos(\omega_{HF}t) e^{j(\hat{\alpha} - \tilde{\theta}_r)} \quad (9.53)$$

$$\int u_d dt = \frac{U_{HF}}{\omega_{HF}} \sin(\omega_{HF}t) \cos(\hat{\alpha} - \tilde{\theta}_r) \quad (9.54)$$

$$\int u_q dt = \frac{U_{HF}}{\omega_{HF}} \sin(\omega_{HF}t) \sin(\hat{\alpha} - \tilde{\theta}_r) \quad (9.55)$$

The current in the actual  $dq$  reference frame is then given by (9.56) and (9.57). Substituting these equations into each other, expressions for them in terms of the integrals of the voltages are obtained as in (9.58) and (9.59). Substituting equations (9.54) and (9.55) into equations (9.58) and (9.59), and by assuming that the error between the actual and estimated rotor position is slowly varying, an expression for the HF current vector in the actual  $dq$ -reference frame is obtained, as in equation (9.63). Finally the HF current vector in the estimated  $dq$ -reference frame is given as in equation (9.64).

$$i_d \approx \frac{1}{L_d} \int \left( u_d - L_{dq} \frac{di_q}{dt} \right) dt = \frac{1}{L_d} \int u_d dt - \frac{L_{dq}}{L_d} i_q \quad (9.56)$$

$$i_q \approx \frac{1}{L_q} \int \left( u_q - L_{dq} \frac{di_d}{dt} \right) dt = \frac{1}{L_q} \int u_q dt - \frac{L_{dq}}{L_q} i_d \quad (9.57)$$

$$i_d \approx \frac{L_d L_q}{L_d L_q - L_{dq}^2} \left( \frac{1}{L_d} \int u_d dt - \frac{L_{dq}}{L_d L_q} \int u_q dt \right) \quad (9.58)$$

$$i_q \approx \frac{L_d L_q}{L_d L_q - L_{dq}^2} \left( \frac{1}{L_q} \int u_q dt - \frac{L_{dq}}{L_d L_q} \int u_d dt \right) \quad (9.59)$$

$$I_{HF} = \frac{U_{HF}}{\omega_{HF}} \sin(\omega_{HF}t) \left( \frac{L_d L_q}{L_d L_q - L_{dq}^2} \right) \quad (9.60)$$

$$i_d \approx I_{HF} \left( \frac{\cos(\hat{\alpha} - \tilde{\theta}_r)}{L_d} - \frac{L_{dq}}{L_d L_q} \sin(\hat{\alpha} - \tilde{\theta}_r) \right) \quad (9.61)$$

$$i_q \approx I_{HF} \left( \frac{\sin(\hat{\alpha} - \tilde{\theta}_r)}{L_q} - \frac{L_{dq}}{L_d L_q} \cos(\hat{\alpha} - \tilde{\theta}_r) \right) \quad (9.62)$$

$$\vec{i}_r \approx I_{HF} \left( \frac{\cos(\hat{\alpha} - \tilde{\theta}_r)}{L_d} + j \frac{\sin(\hat{\alpha} - \tilde{\theta}_r)}{L_q} - j \frac{L_{dq}}{L_d L_q} e^{-j(\hat{\alpha} - \tilde{\theta}_r)} \right) \quad (9.63)$$

$$\begin{aligned} \vec{i}_r &= \vec{i}_r e^{j\tilde{\theta}_r} \\ &= I_{HF} \left[ \left( \frac{1}{L_d} + \frac{1}{L_q} \right) e^{j\hat{\alpha}_r} + \left( \frac{1}{L_d} - \frac{1}{L_q} \right) e^{-j(\hat{\alpha} - 2\tilde{\theta}_r)} - 2j \left( \frac{L_{dq}}{L_d L_q} \right) e^{-j(\hat{\alpha} - 2\tilde{\theta}_r)} \right] \quad (9.64) \end{aligned}$$

For the demodulation, the injection direction  $\alpha$  needs to be taken into consideration, but let us choose it to be zero for the moment (this is usually the choice that people make - they inject the HF voltage in the estimated  $d$ -axis). Then the  $q$ -axis HF current amplitude is driven to zero, so that the estimated reference frame aligns with the actual  $dq$  reference frame. The amplitude of the imaginary component of the HF current in the estimated reference frame, as given in (9.65) is set to zero, and is given after simplification in (9.66). This can be rewritten in the form of (9.67), and solving for the error the result is given in equation (9.68), which is exactly the same as given in (9.49).

$$\frac{U_{HF}}{\omega_{HF}} \left( \frac{L_d L_q}{L_d L_q - L_{dq}^2} \right) \left[ \left( \frac{1}{L_d} - \frac{1}{L_q} \right) \sin 2\tilde{\theta}_r - 2 \frac{L_{dq}}{L_d L_q} \cos 2\tilde{\theta}_r \right] = 0 \quad (9.65)$$

$$\left( \frac{1}{L_d} - \frac{1}{L_q} \right) \sin 2\tilde{\theta}_r - 2 \frac{L_{dq}}{L_d L_q} \cos 2\tilde{\theta}_r = 0 \quad (9.66)$$

$$\tan 2\tilde{\theta}_r = \frac{2L_{dq}}{L_q - L_d} \quad (9.67)$$

$$\tilde{\theta}_r = \frac{1}{2} \tan^{-1} \left( \frac{2L_{dq}}{L_q - L_d} \right) \quad (9.68)$$

Using this formula in (9.68), the offset error for the estimator can be predicted. However, the correct values of  $L_{dq}$ ,  $L_d$  and  $L_q$  need to be known. It has been shown in this work that the fundamental model inductances and the HF model inductances are not the same, where in [36] they are assumed to be the same. It is still a question whether 2D finite element analysis is capable of accurately predicting combined fundamental and HF behaviour of machines. This is another point of discussion and further research is necessary.

### 9.3 Hybrid estimation structure

It has already been shown that hybrid position estimation structures can provide good performance [117, 100, 12, 36, 31, 112]. From the work discussed in this chapter, it is clear that much time was spent on the concepts concerning position estimation with additional HF signals. In order for a hybrid position estimation structure to work, the position estimation based on the fundamental model also needs to be fairly accurate. As already mentioned, position estimation based on back-EMF does not work at low speed, but it also does not work at very low flux linkage magnitudes. Therefore, it is not possible to implement maximum torque per ampere control and rely on rotor position estimation for the field oriented control. A hybrid estimation structure was implemented and tested, but the results are not yet satisfactory, and are not shown here.

## 9.4 Summary for sensorless control

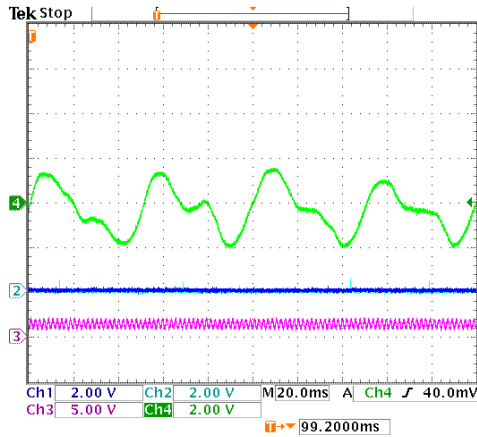
In this chapter some ideas concerning position sensorless control have been presented. The aim of this research was to find a position estimation scheme for the family of synchronous machines namely RSM, PMSM, PMARSM and IPMSM that is capable of working under all operating conditions, i.e. from zero to high speed and zero to full load. Several interesting conclusions were drawn and are given here summarized:

- Geometric and saturation anisotropies can be detected using additional HF voltage excitation. Under no-load conditions, the geometric anisotropy of an RSM can be detected, but it is weak. If the  $q$ -axis of the RSM is saturated due to fundamental  $i_q$ , this is the anisotropy that is detected. The  $q$ -axis is very easily saturated since it has the flux barriers. Therefore in the RSM it is a combination of geometric and saturation anisotropy that is detected, however the saturation anisotropy is much stronger.
- Applying also fundamental  $i_d$  in the RSM, the saturation position (or anisotropy position) shifts away from the  $q$ -axis due to mutual inductance - this causes an offset error between the actual  $q$ -axis and the detected anisotropy position. This offset error can be compensated in two ways: 1) add a load dependent offset to the anisotropy position to obtain the rotor position, 2) change the injection direction according to a load dependent function so that the anisotropy position is always equal to the actual rotor position.
- The variation of the flux linkage vector with varying rotor position causes the self- and mutual inductances to be rotor position dependent as well, and this poses a problem for the rotor position estimation scheme: a rotor position varying estimation error is caused. The shape of the rotor position varying error is periodic, but it is load dependent not even near sinusoidal - the estimation schemes given here do not have the ability to overcome this problem. This raises an interesting question: since skewing the rotor can reduce the flux linkage variation with varying rotor position, could it also improve the position estimation performance?
- In the optimal torque control scheme given in chapter 7, the value of  $i_r^*$  is zero if the torque reference is zero. However, it has been shown that for the rotor position estimation using HF signals to be successful, the  $q$ -axis needs to be saturated. The torque control LUTs can be modified so that a small  $i_q$  is always present, but then it is not maximum torque per ampere any more.
- As shown in [55], the offset error is much more dominant in the case of a RSM compared to the case of a PMSM. The reason is that there is a high amount of mutual inductance in the RSM. Also, the position-varying error is much more dominant in the case of a PMSM compared to the case of a RSM: the reason for this is not so clear,

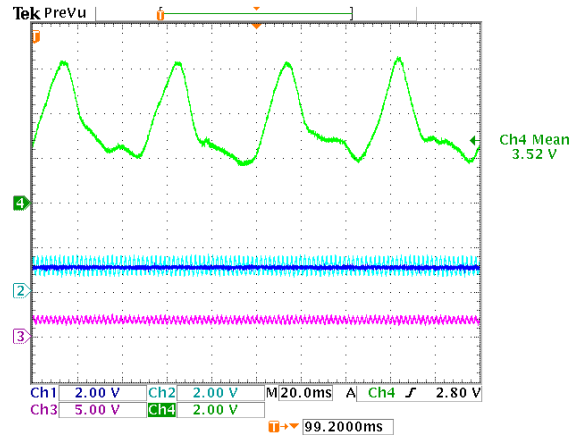
but it seems that high inductance machines are more resilient to flux linkage change with changing rotor position than low inductance machines.

- The rotor position can also be estimated using the fundamental model, but only if both the flux linkage magnitude and the speed have fairly high values, since it is their product that gives the back-EMF. The optimal torque control scheme suggested implies zero current for zero torque reference, but that also implies zero flux linkage, i.e. the position becomes unobservable. More work is necessary in order to combine the fundamental model based estimation scheme with the HF signal based estimation scheme so that the position estimation may be accurate for the operating conditions prescribed by the optimal torque control scheme.

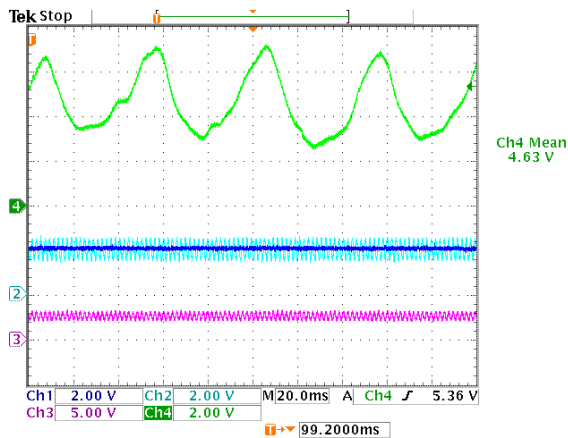
Ch1	$T_m^*$	4	N.m/div
Ch2	$\hat{T}_m$	4	N.m/div
Ch3	$i_r$	5	A/div
Ch4	$\theta_r - \hat{\theta}_r$	2	degrees/div
Time	$t$	20	ms/div



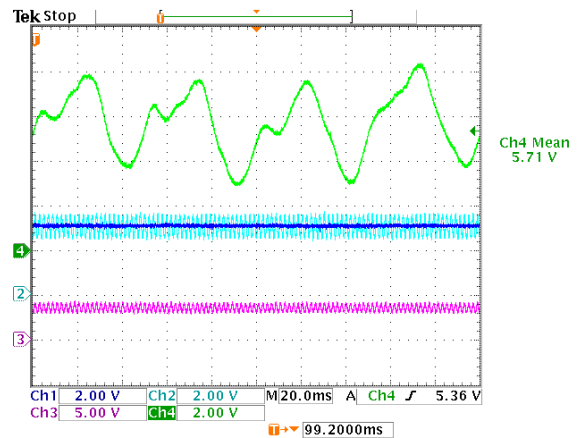
(a) Load = 0 Nm, Speed = 180 rpm



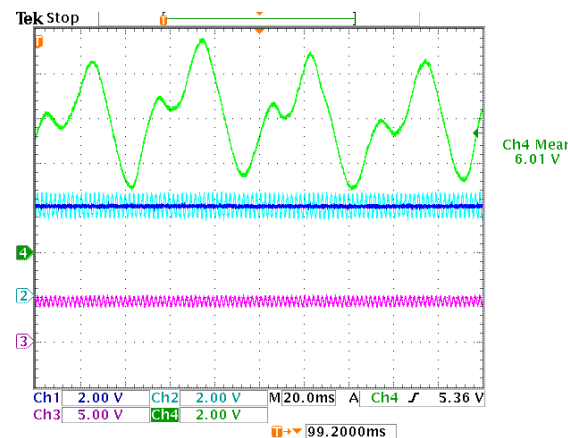
(b) Load = 2 Nm, Speed = 180 rpm



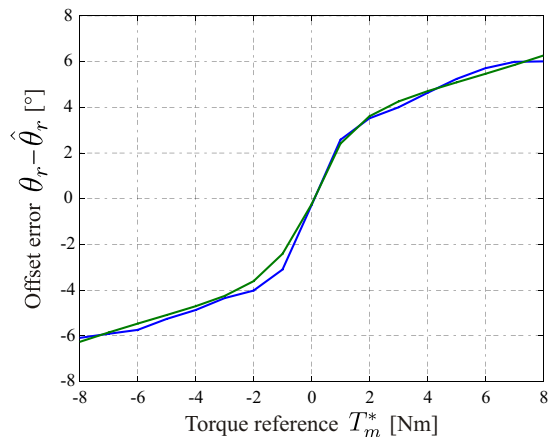
(c) Load = 4 Nm, Speed = 180 rpm



(d) Load = 6 Nm, Speed = 180 rpm



(e) Load = 8 Nm, Speed = 180 rpm

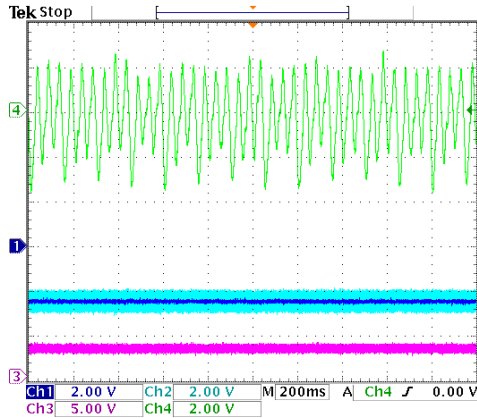


(f) Offset error vs. Torque reference

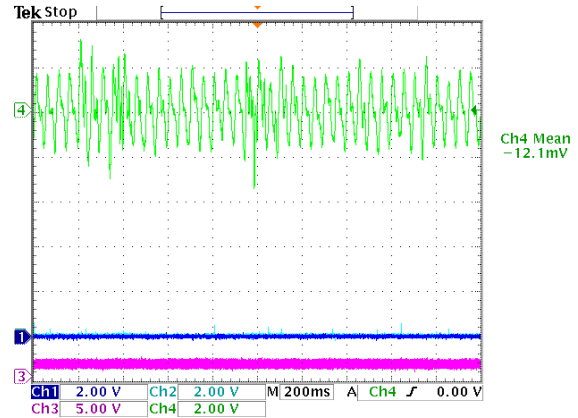
Figure 9.13: Alternating HF observer: estimated position error under load



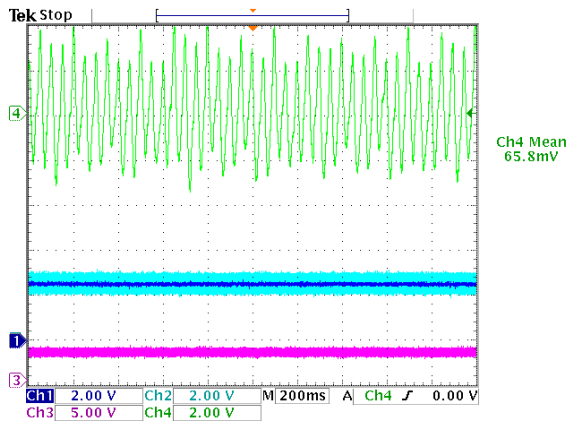
Ch1	$T_m^*$	4	N.m/div
Ch2	$\hat{T}_m$	4	N.m/div
Ch3	$i_r$	5	A/div
Ch4	$\theta_r - \hat{\theta}_r$	2	degrees/div
Time	$t$	200	ms/div



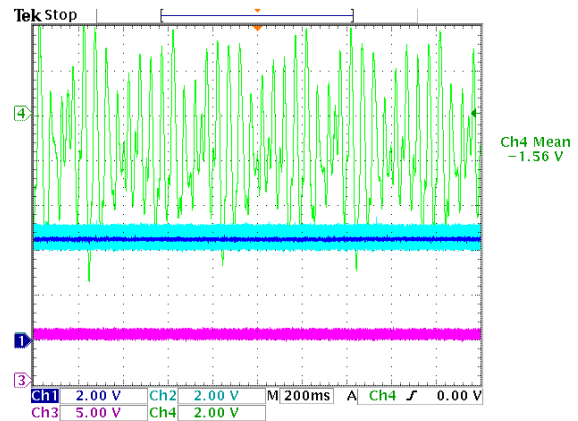
(a) Load = -5 Nm, Speed = 180 rpm



(b) Load = 0 Nm, Speed = 180 rpm

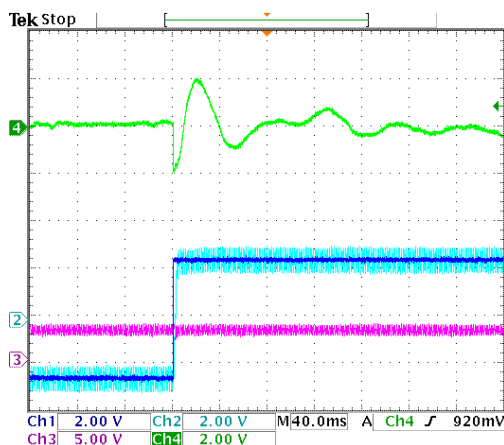


(c) Load = 5 Nm, Speed = 180 rpm



(d) Load = 9 Nm, Speed = 180 rpm

Figure 9.14: Sensorless control - load test



Ch1	$T_m^*$	4	N.m/div
Ch2	$\hat{T}_m$	4	N.m/div
Ch3	$i_r$	5	A/div
Ch4	$\theta_r - \hat{\theta}_r$	10	degrees/div
Time	$t$	40	ms/div

Figure 9.15: Dynamic estimator test.

# Chapter 10

## Conclusions

### **Machine model using space phasor representation**

This thesis started with an introduction to a family of synchronous machines, which includes the permanent magnet synchronous machine (PMSM), interior permanent magnet synchronous machine (IPMSM), reluctance synchronous machine (RSM) and permanent magnet assisted reluctance synchronous machine (PMARSM). In chapter 2 the space phasor theory was applied to give a general mathematical description of the electrical machine model that is applicable to all machines within this family. It was concluded that the space phasor theory is very useful in this regard and crucial for the understanding of machine control and estimation algorithms (including the position sensorless techniques). Some effort was spent in discussing power losses within the machine and a machine model that includes iron-losses and end-winding losses was introduced. However, it was concluded that for many cases regarding the control of the machine, it is sufficient to use the simplified model that does not consider iron-losses or end-winding losses.

### ***dq* machine model in polar coordinates**

The work in this thesis is applicable to the family of synchronous machines introduced. A RSM is used as an example throughout the thesis. Chapter 3 provides an in-depth view into the RSM model based on the space vector theory. The model in the synchronously rotating *dq* reference frame is shown in Cartesian, Polar and Cylindrical coordinates, providing the opportunity to understand the space vector concepts and non-linear machine behaviour fully. Fig. 3.5 is very important, since it highlights several aspects including maximum torque per ampere and the effect that the inverter's voltage limitation has on the achievable operating conditions. This mathematical representation of the machine is paramount to the understanding of the machine behaviour and the development of an energy efficient torque control strategy that includes maximum torque per ampere and effective field weakening.

### Field orientated control

The focus is then shifted to machine control. Field orientated control (FOC) (see chapter 4), which is closed loop current vector control through open loop voltage vector control using pulse width modulation (PWM), is chosen as the preferred control method over direct torque control (DTC). There is no in-depth discussion about the positive and negative aspects of both the control schemes and the choice is based only on past experience. Therefore no conclusions can be drawn whether FOC is better than DTC or the other way around.

Chapter 5 focuses on practical implementation of the voltage vector control and shows that by changing the three-phase voltage references before they are compared to a carrier value after normalization, a better utilization of the DC bus voltage may be obtained in an easy way. Space vector pulse width modulation (SVPWM) is not implemented directly, but the result of the modified references with carrier-based PWM is the same as that of SVPWM. That is, by modifying the three-phase voltage references, zero vectors are introduced, which are not present in the method with normal sinusoidal voltage reference comparison with the carrier. It is concluded that for ease of implementation, the selected PWM method proved to be a good choice.

In chapter 6 the implementation of a current vector controller in the synchronously rotating  $dq$  reference frame is discussed. A vector proportional integral (PI) controller is suggested, with the added features of speed voltage vector decoupling and integrator anti-windup. The speed voltage vector is calculated as the product of the estimated electrical speed and the estimated flux linkage vector in the  $dq$  reference frame, which is obtained by using a set of two-dimensional lookup tables (from finite element (FE) analysis) and two-dimensional interpolation. If the speed voltage vector decoupling is effective, the vector PI controller only needs to take care of the resistive voltage vector, the derivative of the flux linkage vector and any other unmodelled machine behaviour. The integrator anti-windup is achieved by simply setting the input to the integrators equal to zero when the voltage magnitude limit has been reached. Although there has been no thorough comparison with other methods of integrator anti-windup, it is found that this method is effective and it is easy to implement. It is also clear when comparing the simulation and practical results shown in this chapter, that the machine model from finite element analysis (FEA) and the method of simulation using the rapid prototyping system (RPS) are very accurate. It is clearly stressed in this chapter that we are dealing with a current vector and not two separate systems in the  $d$ -axis and  $q$ -axis. The current vector control with some advanced features is clearly explained and it is concluded that the method is effective.

### Torque and speed control

One of the most important contributions of this work is described in chapter 7, which is about torque control. A generic method of open loop torque control, which is applicable to all the machines in the family of synchronous machines introduced, is presented. Compared to other

methods of torque control, there is no approximation of machine parameters, no iterative procedures or complicated decision trees to follow. The method can work at any speed and for any DC bus voltage. There is also a strong emphasis on ease of implementation and reduced processing power needed to execute the algorithm, since most of the calculations are performed off-line in an automated process that relies on the results of finite element analysis (FEA). A set of two-dimensional lookup tables with the torque reference and the maximum flux linkage magnitude as inputs and the optimal achievable current vector reference as output is the core of the algorithm. Two-dimensional interpolation is used so that the size of the tables may be reduced. The tables are created in an automated process that is based on decision making logic and uses the FE results directly. The first implementation was for an IPMSM and in this thesis it is shown that it is equally applicable to the RSM. In conclusion it is found that this method of torque control results in high energy efficiency and effective flux weakening, and the method is suitable for industrial applications.

The chapter on speed control (see chapter 8) is rather insignificant in this work, but it is shown that using a simple PI controller, the speed response for rated speed under no load conditions is good and twice the rated speed under no load conditions can almost be reached. The good correlation between the simulated and practical results proves that the simple mechanical model of the RSM, which was used in the simulation, is effective.

### **Position sensorless control**

The largest and most important part in this work is the chapter on position sensorless control (see chapter 9). Fundamental frequency model based rotor position estimation is introduced first, and it is shown that the rotor position becomes unobservable for zero flux linkage magnitude or zero speed. An alternative method in which the actual machine is used like a resolver is introduced to overcome the limitation at zero speed. This method is based on a simple anisotropy model ( $L_d \neq L_q$ ), and it is shown that a high frequency (HF) model of the actual machine is similar to this simple anisotropy model, but only when the cross coupling and variation of flux linkage with varying rotor position are both zero. And even if there is little cross coupling (mutual inductance) and only a small variation of flux linkage with varying rotor position, the values of self inductances  $L_d$  and  $L_q$  may change a lot under heavy saturation, influencing the stability of the scheme using the phase locked loop (PLL) structure.

Two rotor position estimation schemes using HF signals are discussed: firstly the rotating voltage vector in the stationary reference frame and secondly the alternating voltage vector in the estimated anisotropy reference frame. In the first case a large assumption is made that the speed is close to zero, and therefore the method does not work at any other other speed than very low speeds. In the second case, the only assumption that is made is that the error between the estimated and actual anisotropy reference frame is small, which is true when a PLL structure is used to track the anisotropy position. Therefore, the second method may

be used to track rotor speed from zero to a high value. But of course the voltage is needed at high speed for the fundamental frequency excitation and should not be used for additional HF voltage excitation.

When focusing on the rotor position estimation method with alternating HF voltage vector excitation in the estimated anisotropy reference frame, several interesting results have been found. For a PMSM the anisotropy position can be found at the point where the permanent magnet saturates the stator, i.e. under no load the anisotropy position is equal to the rotor position. This should be valid for any load, however under high load conditions the anisotropy position may shift away from the rotor position due to cross-coupling. This is a load dependent offset error that must be compensated, unless it is very small. There is however also a position varying error between the detected anisotropy position and actual rotor position, due to the fact that the variation of the flux linkage vector with varying rotor position is not equal to zero. That implies that all inductances, including mutual inductance, is also position dependent. This “time-varying” or actually position varying error is very difficult to compensate, and therefore the focus should rather be on designing the machine better (basically less torque ripple).

One would expect the RSM to be a very easy machine to control position sensorless, because “the machine has a very large saliency”. This statement is true in a way, since the only torque producing mechanism is through saliency. Saliency is expressed mathematically as a difference in quadrature inductances. However, one should clearly make the distinction between secant inductances (used in the torque equation) and tangential inductances (used in the voltage equation). For sensorless control, only the tangential (also called differential or partial) inductances come into play. Now in the RSM, under no-load conditions there is a very small difference between  $L_{dt}$  and  $L_{qt}$ . Using the HF voltage injection, a kind of geometric anisotropy can be detected, but it is very weak. The  $q$ -axis of the RSM is very easily saturated, since this is the axis with the flux barriers and there are usually small iron ribs that saturate easily. It is therefore concluded that the  $q$ -axis of the RSM should be kept in saturation, even under no load conditions, to improve the quality of rotor position estimation. This is of-course against the policy of energy efficient or maximum torque per Ampere (MTPA) control, but it has been shown that the quality of rotor position estimation is much better when the  $q$ -axis is saturated.

The RSM does have a large degree of cross coupling. Therefore it is clear that once the machine is loaded, the anisotropy position moves from the  $q$ -axis towards the  $d$ -axis, in a non-linear way. It has been shown in this work, that this offset error can be compensated in two ways: by injecting the alternating voltage vector in a constant direction and by applying the load dependent compensation at the end, i.e. having two separate reference frames, one for the anisotropy and one for the actual rotor position; or the direction; or by injecting the alternating voltage vector in a direction than depends on the load and thereby aligning the detected anisotropy position with the actual rotor position. The second method of compensation is preferred since this eases the integration of this rotor position estimation

method with the fundamental frequency model based estimation method.

Another interesting feature of the RSM is that the flux linkage vector variation with varying rotor position is not so big under loaded conditions, which helps to improve the quality of rotor position estimation. It is expected that a PM assisted RSM is a good machine for position sensorless control, since the  $q$ -axis is already saturated due to the PMs in the flux barriers, the mutual coupling and the variation of the flux linkage vector with varying rotor position is generally less than for a normal RSM. However, a major disadvantage of having PMs in the rotor is that the polarity also has to be detected in a separate procedure at startup.

Ultimately the goal was to achieve rotor position and speed estimation with good quality in the full speed range. It is believed that a hybrid structure that uses both a fundamental frequency model based rotor position estimation and HF signal injection is the answer. Although some initial tests were performed and the theory is clear, successful implementation has not been achieved. In order for these estimation schemes to work properly, there must always be a certain amount of flux linkage magnitude, even under no load conditions, and that is against the idea of MTPA. It is concluded that further research is necessary in this regard.

### **Final remark**

This thesis has highlighted several concepts that are important for energy efficient, robust, reliable and cost effective control of the next generation of electrical machine drives. An overview with respect to several applications is provided, as well as in-depth views into various machine control aspects. Several publications at international conferences have resulted as a part of this work, and still many results are unpublished. It is believed that this work will play an important role in many applications if it is implemented and developed further.

# Chapter 11

## Recommendations

Based on the research and development that has taken place during the course of this work, the following recommendations are made concerning further research, development and industrial implementation.

### **Practical test bench**

The Rapid Prototyping System (RPS) that has been developed over many years at the University of Wuppertal in Germany is a wonderful tool for laboratory experiments, since it has been proven in this work that both simulation and practical results may be obtained using it. The RPS runs the Linux operating system with the Real Time Applications Interface (RTAI) and in this work all the control and simulation programming code is written in ANSI C as "kernel modules". All code is written in a modular structure, so that it should be easy to adapt the code quickly for a new machine or a different configuration of the RPS. For example, there is a "toolbox" library that contains functions like integrators, two-dimensional interpolation for two-dimensional lookup tables, PI controllers etc, and there is another library called "machine" that contains the most important machine parameters and functions to simulate machine behaviour etc. It is recommended that this modular structure for the programming code be used in future work, since it has proven to be very effective for conducting research.

However, there is still room for improvement in the program, especially concerning optimization of the code to make it less computationally intensive. It is recommended that the program be critically evaluated and rewritten to be more efficient.

The practical test bench used during the course of this work did not have a torque sensor and it is recommended that such a sensor be used in future work to enhance the quality and accuracy. The system with two electrical machines connected mechanically which are fed by two inverters that share the same DC bus voltage proved to be very useful. It is recommended that such a system be used, only with the inclusion of a torque sensor.

Although the Wuppertal RPS is a good choice based on cost, it is believed that other similar systems could be used to accelerate the pace at which research is performed and results are published further. A popular choice is known as "dSpace" ([www.dspace.de](http://www.dspace.de)),

however there are also other alternatives available, e.g. from a Belgium company known as “Triphase” ([www.triphase.com](http://www.triphase.com)). It is recommended that alternative rapid prototyping systems be tested and the features that are missing in the Wuppertal RPS be developed and implemented for it.

### **Electrical machine control**

The concept of energy efficient torque control and effective flux weakening presented in this thesis has been shown to be a success, based on work that was performed for an interior permanent magnet synchronous machine (IPMSM) with concentrated stator windings, and for a reluctance synchronous machine (RSM) with distributed stator windings. It is recommended that the work should also be tested for a permanent magnet synchronous machine (PMSM) and a permanent magnet assisted reluctance synchronous machine (PMARSM), so that it is clear that this method is generic.

In this work it is assumed that the machine in question has a model in a finite element (FE) program, so the results from this program can be used to generate a set of lookup tables (LUTs) needed in this torque control scheme. Although it is very common practice today that machines are designed by such programs, it could be that one would like to implement this scheme for a synchronous machine without a model in a FE program. It is recommended that a practical test procedure be put into place that will give the necessary data needed, i.e. a mapping of current to flux linkage in the  $dq$  reference frame.

In this work an increased usage of DC bus voltage is obtained by using a PWM method equivalent to space vector PWM, instead of using the normal sub-oscillation method (sinusoidal carrier based method). However, this voltage limitation still does not use the full hexagon that is available. It is recommended that the PWM method and voltage limitation method be modified to make full use of the available DC bus voltage, and that over-modulation methods be studied and implemented to further increase the voltage capacity.

### **Rotor position and speed estimation**

In this work a rotor position and speed estimator based of the fundamental frequency model of a synchronous machine is shown. It relies on the premise that neither the speed nor the flux linkage magnitude is zero, since the rotor position is estimated from the flux linkage vector, which is estimated from the back-EMF vector, which is the product of speed and flux linkage in the steady state. It is recommended that inverter dead-time compensation and stator resistance estimation be included in this scheme, to expand the limits of its operation range. Furthermore, it should be determined at what speed level and flux linkage magnitude level this method of rotor position estimation is accurate enough to be used.

It is clear that at zero speed the only way to obtain the rotor position is to use additional high frequency (HF) signals. The additional voltage needed to excite the HF signals is no problem at zero and low speed, but it should also be clear that at high speed all the voltage is needed for the fundamental frequency machine control. It is recommended that alternating



HF voltage excitation in the estimated reference frame be used, instead of rotating HF voltage excitation in the stationary reference frame. Furthermore, to compensate the effects of cross-coupling (offset error in the position estimation), it is recommended that the angle of voltage injection be a function of load, so that the average value of the resulting detected anisotropy position is equal to the actual rotor position. Of course this function needs to be found somehow, therefore it is recommended that a test procedure be standardized and that the prediction from FE analysis using this test be compared with practical measurements. It will be very convenient if this compensation function can be generated using only FE results.

The combination of the fundamental frequency model based and HF signal based rotor position estimation techniques will be much easier once each of them is accurate on its own and the limits of operating range for each one is known. It is recommended that different structures of a combined or hybrid estimation scheme be considered.

# Bibliography

- [1] B. Ackermann, “Single-phase induction motor with permanent magnet excitation,” *Magnetics, IEEE Transactions on*, vol. 36, no. 5, pp. 3530–3532, 2000.
- [2] M. Popescu, T. Miller, M. McGilp, G. Strappazon, N. Trivillin, and R. Santarossa, “Asynchronous performance analysis of a single-phase capacitor-start, capacitor-run permanent magnet motor,” *Energy Conversion, IEEE Transaction on*, vol. 20, no. 1, pp. 142–150, 2005.
- [3] T. Tsuda, T. Fukami, Y. Kanamaru, and T. Miyamoto, “Effects of the built-in permanent magnet rotor on the equivalent circuit parameters of a permanent magnet induction generator,” *Energy Conversion, IEEE Transaction on*, vol. 22, no. 3, pp. 798–799, 2007.
- [4] M. Linke, R. Kennel, and J. Holtz, “Sensorless speed and position control of synchronous machines using alternating carrier injection,” in *Electric Machines and Drives Conference, 2003. IEMDC’03. IEEE International*, vol. 2, 2003, pp. 1211–1217 vol.2.
- [5] M. Corley and R. Lorenz, “Rotor position and velocity estimation for a salient-pole permanent magnet synchronous machine at standstill and high speeds,” *Industry Applications, IEEE Transactions on*, vol. 34, no. 4, pp. 784–789, 1998.
- [6] S. Morimoto, K. Kawamoto, M. Sanada, and Y. Takeda, “Sensorless control strategy for salient-pole pmsm based on extended emf in rotating reference frame,” *Industry Applications, IEEE Transactions on*, vol. 38, no. 4, pp. 1054–1061, 2002.
- [7] M. Haque, L. Zhong, and M. Rahman, “A sensorless initial rotor position estimation scheme for a direct torque controlled interior permanent magnet synchronous motor drive,” *Power Electronics, IEEE Transactions on*, vol. 18, no. 6, pp. 1376–1383, 2003.
- [8] H. Kim, M. Harke, and R. Lorenz, “Sensorless control of interior permanent-magnet machine drives with zero-phase lag position estimation,” *Industry Applications, IEEE Transactions on*, vol. 39, no. 6, pp. 1726–1733, 2003.
- [9] V. Petrovic, A. Stankovic, and V. Blasko, “Position estimation in salient pm synchronous motors based on pwm excitation transients,” *Industry Applications, IEEE Transactions on*, vol. 39, no. 3, pp. 835–843, 2003.

- [10] H. Kim, K.-K. Huh, R. Lorenz, and T. Jahns, "A novel method for initial rotor position estimation for ipm synchronous machine drives," *Industry Applications, IEEE Transactions on*, vol. 40, no. 5, pp. 1369–1378, 2004.
- [11] Y.-s. Jeong, R. Lorenz, T. Jahns, and S.-K. Sul, "Initial rotor position estimation of an interior permanent-magnet synchronous machine using carrier-frequency injection methods," *Industry Applications, IEEE Transactions on*, vol. 41, no. 1, pp. 38–45, 2005.
- [12] O. Wallmark, L. Harnefors, and O. Carlson, "An improved speed and position estimator for salient permanent-magnet synchronous motors," *Industrial Electronics, IEEE Transactions on*, vol. 52, no. 1, pp. 255–262, 2005.
- [13] N. Imai, S. Morimoto, M. Sanada, and Y. Takeda, "Influence of magnetic saturation on sensorless control for interior permanent-magnet synchronous motors with concentrated windings," *Industry Applications, IEEE Transactions on*, vol. 42, no. 5, pp. 1193–1200, 2006.
- [14] N. Bianchi, S. Bolognani, J.-H. Jang, and S.-K. Sul, "Comparison of pm motor structures and sensorless control techniques for zero-speed rotor position detection," in *Power Electronics Specialists Conference, 2006. PESC '06. 37th IEEE*, 2006, pp. 1–7.
- [15] —, "Comparison of pm motor structures and sensorless control techniques for zero-speed rotor position detection," *Power Electronics, IEEE Transactions on*, vol. 22, no. 6, pp. 2466–2475, 2007.
- [16] M. Kamper, F. Van der Merwe, and S. Williamson, "Direct finite element design optimisation of the cageless reluctance synchronous machine," *Energy Conversion, IEEE Transaction on*, vol. 11, no. 3, pp. 547–555, 1996.
- [17] M. Arefeen, M. Ehsani, and A. Lipo, "Sensorless position measurement in synchronous reluctance motor," *Power Electronics, IEEE Transactions on*, vol. 9, no. 6, pp. 624–630, 1994.
- [18] R. Lagerquist, I. Boldea, and T. Miller, "Sensorless-control of the synchronous reluctance motor," *Industry Applications, IEEE Transactions on*, vol. 30, no. 3, pp. 673–682, 1994.
- [19] M. Schroedl and P. Weinmeier, "Sensorless control of reluctance machines at arbitrary operating conditions including standstill," *Power Electronics, IEEE Transactions on*, vol. 9, no. 2, pp. 225–231, 1994.
- [20] T. Matsuo and T. Lipo, "Rotor position detection scheme for synchronous reluctance motor based on current measurements," *Industry Applications, IEEE Transactions on*, vol. 31, no. 4, pp. 860–868, 1995.

- [21] M. Jovanovic, R. Betz, and D. Platt, "Sensorless vector controller for a synchronous reluctance motor," *Industry Applications, IEEE Transactions on*, vol. 34, no. 2, pp. 346–354, 1998.
- [22] A. Consoli, F. Russo, G. Scarcella, and A. Testa, "Low- and zero-speed sensorless control of synchronous reluctance motors," *Industry Applications, IEEE Transactions on*, vol. 35, no. 5, pp. 1050–1057, 1999.
- [23] S.-J. Kang, J.-M. Kim, and S.-K. Sul, "Position sensorless control of synchronous reluctance motor using high frequency current injection," *Energy Conversion, IEEE Transaction on*, vol. 14, no. 4, pp. 1271–1275, 1999.
- [24] A. Consoli, C. Cavallaro, G. Scarcella, and A. Testa, "Sensorless torque control of syncrel motor drives," *Power Electronics, IEEE Transactions on*, vol. 15, no. 1, pp. 28–35, 2000.
- [25] M.-T. Lin and T.-H. Liu, "Sensorless synchronous reluctance drive with standstill starting," *Aerospace and Electronic Systems, IEEE Transactions on*, vol. 36, no. 4, pp. 1232–1241, 2000.
- [26] A. Vagati, M. Pastorelli, F. Scapino, and G. Franceschini, "Impact of cross saturation in synchronous reluctance motors of the transverse-laminated type," *Industry Applications, IEEE Transactions on*, vol. 36, no. 4, pp. 1039–1046, 2000.
- [27] E. Capecchi, P. Guglielmi, M. Pastorelli, and A. Vagati, "Position-sensorless control of the transverse-laminated synchronous reluctance motor," *Industry Applications, IEEE Transactions on*, vol. 37, no. 6, pp. 1768–1776, 2001.
- [28] T. Senjyu, T. Shingaki, and K. Uezato, "Sensorless vector control of synchronous reluctance motors with disturbance torque observer," *Industrial Electronics, IEEE Transactions on*, vol. 48, no. 2, pp. 402–407, 2001.
- [29] C.-G. Chen, T.-H. Liu, M.-T. Lin, and C.-A. Tai, "Position control of a sensorless synchronous reluctance motor," *Industrial Electronics, IEEE Transactions on*, vol. 51, no. 1, pp. 15–25, 2004.
- [30] S. Ichikawa, M. Tomita, S. Doki, and S. Okuma, "Sensorless control of synchronous reluctance motors based on extended emf models considering magnetic saturation with online parameter identification," *Industry Applications, IEEE Transactions on*, vol. 42, no. 5, pp. 1264–1274, 2006.
- [31] A. Consoli, G. Scarcella, G. Scelba, A. Testa, and D. Triolo, "Sensorless rotor position estimation in synchronous reluctance motors exploiting a flux deviation approach," *Industry Applications, IEEE Transactions on*, vol. 43, no. 5, pp. 1266–1273, 2007.

- [32] H. de Kock, M. Kamper, O. Ferreira, and R. Kennel, "Position sensorless control of the reluctance synchronous machine considering high frequency inductances," in *Power Electronics and Drive Systems, 2007. PEDS'07*, 2007.
- [33] S. Sibande, M. Kamper, R. Wang, and E. Rakgati, "Optimal design of a pm-assisted rotor of a 110 kw reluctance synchronous machine," in *AFRICON, 2004. 7th AFRICON Conference in Africa*, vol. 2, 2004, pp. 793–797 Vol.2.
- [34] H. de Kock and M. Kamper, "Dynamic control of the permanent magnet-assisted reluctance synchronous machine," *Electric Power Applications, IET*, vol. 1, no. 2, pp. 153–160, 2007.
- [35] P. Guglielmi, M. Pastorelli, G. Pellegrino, and A. Vagati, "Position-sensorless control of permanent-magnet-assisted synchronous reluctance motor," *Industry Applications, IEEE Transactions on*, vol. 40, no. 2, pp. 615–622, 2004.
- [36] P. Guglielmi, M. Pastorelli, and A. Vagati, "Impact of cross-saturation in sensorless control of transverse-laminated synchronous reluctance motors," *Industrial Electronics, IEEE Transactions on*, vol. 53, no. 2, pp. 429–439, 2006.
- [37] J. Fuchsloch, W. Finley, and R. Walter, "The next generation motor," *Industry Applications Magazine, IEEE*, vol. 14, no. 1, pp. 37–43, 2008.
- [38] M. Rahman, L. Zhong, and K. W. Lim, "A direct torque-controlled interior permanent magnet synchronous motor drive incorporating field weakening," *Industry Applications, IEEE Transactions on*, vol. 34, no. 6, pp. 1246–1253, 1998.
- [39] H.-D. Lee, S.-J. Kang, and S.-K. Sul, "Efficiency-optimized direct torque control of synchronous reluctance motor using feedback linearization," *Industrial Electronics, IEEE Transactions on*, vol. 46, no. 1, pp. 192–198, 1999.
- [40] L. Zhong, M. Rahman, W. Hu, K. Lim, and M. Rahman, "A direct torque controller for permanent magnet synchronous motor drives," *Energy Conversion, IEEE Transaction on*, vol. 14, no. 3, pp. 637–642, 1999.
- [41] L. Tang, L. Zhong, M. Rahman, and Y. Hu, "A novel direct torque controlled interior permanent magnet synchronous machine drive with low ripple in flux and torque and fixed switching frequency," *Power Electronics, IEEE Transactions on*, vol. 19, no. 2, pp. 346–354, 2004.
- [42] M. Pacas and J. Weber, "Predictive direct torque control for the pm synchronous machine," *Industrial Electronics, IEEE Transactions on*, vol. 52, no. 5, pp. 1350–1356, 2005.

- [43] K. Gulez, A. Adam, and H. Pastaci, "A novel direct torque control algorithm for ipmsm with minimum harmonics and torque ripples," *Mechatronics, IEEE/ASME Transactions on*, vol. 12, no. 2, pp. 223–227, 2007.
- [44] Z. Xu and M. Rahman, "Direct torque and flux regulation of an ipm synchronous motor drive using variable structure control approach," *Power Electronics, IEEE Transactions on*, vol. 22, no. 6, pp. 2487–2498, 2007.
- [45] S. Morimoto, M. Sanada, and Y. Takeda, "Wide-speed operation of interior permanent magnet synchronous motors with high-performance current regulator," *Industry Applications, IEEE Transactions on*, vol. 30, no. 4, pp. 920–926, 1994.
- [46] S.-K. Chung, H.-S. Kim, C.-G. Kim, and M.-J. Youn, "A new instantaneous torque control of pm synchronous motor for high-performance direct-drive applications," *Power Electronics, IEEE Transactions on*, vol. 13, no. 3, pp. 388–400, 1998.
- [47] F.-J. Lin and R.-J. Wai, "A hybrid computed torque controller using fuzzy neural network for motor-quick-return servo mechanism," *Mechatronics, IEEE/ASME Transactions on*, vol. 6, no. 1, pp. 75–89, 2001.
- [48] R. Monajemy and R. Krishnan, "Control and dynamics of constant-power-loss-based operation of permanent-magnet synchronous motor drive system," *Industrial Electronics, IEEE Transactions on*, vol. 48, no. 4, pp. 839–844, 2001.
- [49] M. Bech, T. Frederiksen, and P. Sandholdt, "Accurate torque control of saturated interior permanent magnet synchronous motors in the field-weakening region," in *Industry Applications Conference, 2005. Fourtieth IAS Annual Meeting. Conference Record of the 2005*, vol. 4, 2005, pp. 2526–2532 Vol. 4.
- [50] C.-T. Pan and S.-M. Sue, "A linear maximum torque per ampere control for ipmsm drives over full-speed range," *Energy Conversion, IEEE Transaction on*, vol. 20, no. 2, pp. 359–366, 2005.
- [51] Y.-R. Mohamed, "A newly designed instantaneous-torque control of direct-drive pmsm servo actuator with improved torque estimation and control characteristics," *Industrial Electronics, IEEE Transactions on*, vol. 54, no. 5, pp. 2864–2873, 2007.
- [52] R. Morales-Caporal and M. Pacas, "A predictive torque control for the synchronous reluctance machine taking into account the magnetic cross saturation," *Industrial Electronics, IEEE Transactions on*, vol. 54, no. 2, pp. 1161–1167, 2007.
- [53] H. de Kock, "Dynamic control of the permanent magnet assisted reluctance synchronous machine with constant current angle," Master's thesis, University of Stellenbosch, 2006.

- [54] H. de Kock and M. Kamper, "Energy efficient current control of the permanent magnet assisted reluctance synchronous machine," in *Southern African Universities Power Engineering Conference (SAUPEC)*, 2006.
- [55] H. de Kock, M. Kamper, and R. Kennel, "Anisotropy comparison of reluctance and pm synchronous machines for low speed position sensorless applications," in *13th International Conference on Power Electronics and Motion Control (EPE-PEMC)*, 2008.
- [56] H. de Kock, A. Rix, and M. Kamper, "Optimal torque control of interior permanent magnet synchronous machines in the full speed range," in *Proceedings of the 2008 International Conference on Electrical Machines (ICEM)*, 2008.
- [57] H. de Kock and R. Kennel, "Kompensation der lastabhangigkeit von industriellen servoantrieben mit geberloser regelung," in *VDE/VDI-Fachtagung - Elektrisch-mechanische Antriebssysteme*, 2008.
- [58] A. J. Rix, M. J. Kamper, and R.-J. Wang, "Design and performance evaluation of concentrated coil permanent magnet machines for in-wheel drives," in *Electric Machines & Drives Conference, 2007. IEMDC '07. IEEE International*, M. J. Kamper, Ed., vol. 1, 2007, pp. 770–775.
- [59] P. Szczupak, "Rapid prototyping system for control of inverters and electrical drives," Ph.D. dissertation, University of Wuppertal, Germany, 2008.
- [60] OE, "2008 media release document, pictures and video," October 2008. [Online]. Available: [www.optimalenergy.co.za](http://www.optimalenergy.co.za)
- [61] P. Vas, *Vector Control of AC Machines*, I. 0-19-859370-8, Ed. Clarendon Press Oxford, 1990.
- [62] J. F. Gieras, R. Wang, and M. J. Kamper, *Axial Flux Permanent Magnet Brushless Machines*, I. 978-1-4020-6993-2, Ed. The Springer, 2008.
- [63] M. Gyimesi and D. Ostergaard, "Inductance computation by incremental finite element analysis," *Magnetics, IEEE Transactions on*, vol. 35, no. 3, pp. 1119–1122, 1999.
- [64] J. Hu, L. Xu, and J. Liu, "Eddy current effects on rotor position estimation for sensorless control of pm synchronous machine," in *Industry Applications Conference, 2006. 41st IAS Annual Meeting. Conference Record of the 2006 IEEE*, L. Xu, Ed., vol. 4, 2006, pp. 2034–2039.
- [65] H. van der Broeck, H.-C. Skudelny, and G. Stanke, "Analysis and realization of a pulsewidth modulator based on voltage space vectors," *Industry Applications, IEEE Transactions on*, vol. 24, no. 1, pp. 142–150, 1988.

- [66] D. Leggate and R. Kerkman, "Pulse based dead time compensator for pwm voltage inverters," in *Industrial Electronics, Control, and Instrumentation, 1995., Proceedings of the 1995 IEEE IECON 21st International Conference on*, 1995.
- [67] V. Kaura and V. Blasko, "A new method to extend linearity of a sinusoidal pwm in the overmodulation region," *Industry Applications, IEEE Transactions on*, vol. 32, no. 5, pp. 1115–1121, 1996.
- [68] V. Blasko, "Analysis of a hybrid pwm based on modified space-vector and triangle-comparison methods," *Industry Applications, IEEE Transactions on*, vol. 33, no. 3, pp. 756–764, 1997.
- [69] D.-W. Chung, J.-S. Kim, and S.-K. Sul, "Unified voltage modulation technique for real-time three-phase power conversion," *Industry Applications, IEEE Transactions on*, vol. 34, no. 2, pp. 374–380, 1998.
- [70] J.-O. Krah and J. Holtz, "High-performance current regulation and efficient pwm implementation for low-inductance servo motors," *Industry Applications, IEEE Transactions on*, vol. 35, no. 5, pp. 1039–1049, 1999.
- [71] J.-H. Youm and B.-H. Kwon, "An effective software implementation of the space-vector modulation," *Industrial Electronics, IEEE Transactions on*, vol. 46, no. 4, pp. 866–868, 1999.
- [72] B.-H. Bae and S.-K. Sul, "A novel dynamic overmodulation strategy for fast torque control of high-saliency-ratio ac motor," *Industry Applications, IEEE Transactions on*, vol. 41, no. 4, pp. 1013–1019, 2005.
- [73] H. Schmirgel and J.-O. Krah, "Compensation of nonlinearities in the igtb power stage of servo amplifiers through feed forward control in the current loop," in *PCIM, PCIM, Ed.*, 2005, pp. 94–99.
- [74] G. Wang, D. Xu, and Y. Yu, "A novel strategy of dead-time compensation for pwm voltage-source inverter," in *Applied Power Electronics Conference and Exposition, 2008. APEC 2008. Twenty-Third Annual IEEE*, 2008.
- [75] M. Jovanovic and R. Betz, "Optimal torque controller for synchronous reluctance motors," *Energy Conversion, IEEE Transaction on*, vol. 14, no. 4, pp. 1088–1093, 1999.
- [76] Y. A.-R. I. Mohamed, "A hybrid-type variable-structure instantaneous torque control with a robust adaptive torque observer for a high-performance direct-drive pmsm," *Industrial Electronics, IEEE Transactions on*, vol. 54, no. 5, pp. 2491–2499, 2007.



- [77] Z. Xu and M. Rahman, "An adaptive sliding stator flux observer for a direct-torque-controlled ipm synchronous motor drive," *Industrial Electronics, IEEE Transactions on*, vol. 54, no. 5, pp. 2398–2406, 2007.
- [78] R. Sepe and J. Lang, "Real-time observer-based (adaptive) control of a permanent-magnet synchronous motor without mechanical sensors," *Industry Applications, IEEE Transactions on*, vol. 28, no. 6, pp. 1345–1352, 1992.
- [79] J. S. Kim and S. K. Sul, "New approach for high performance pmsm drives without rotational position sensors," in *Applied Power Electronics Conference and Exposition, 1995. APEC '95. Conference Proceedings 1995., Tenth Annual*, no. 0, 1995, pp. 381–386 vol.1.
- [80] J.-S. Kim and S.-K. Sul, "High performance pmsm drives without rotational position sensors using reduced order observer," in *Industry Applications Conference, 1995. Thirtieth IAS Annual Meeting, IAS '95., Conference Record of the 1995 IEEE*, vol. 1, 1995, pp. 75–82 vol.1.
- [81] M. Degner and R. Lorenz, "Using multiple saliencies for the estimation of flux, position, and velocity in ac machines," *Industry Applications, IEEE Transactions on*, vol. 34, no. 5, pp. 1097–1104, 1998.
- [82] A. Consoli, G. Scarcella, and A. Testa, "Industry application of zero-speed sensorless control techniques for pm synchronous motors," *Industry Applications, IEEE Transactions on*, vol. 37, no. 2, pp. 513–521, 2001.
- [83] J.-H. Jang, S.-K. Sul, J.-I. Ha, K. Ide, and M. Sawamura, "Sensorless drive of smpm motor by high frequency signal injection," in *Applied Power Electronics Conference and Exposition, 2002. APEC 2002. Seventeenth Annual IEEE*, vol. 1, 2002, pp. 279–285 vol.1.
- [84] M. Linke, R. Kennel, and J. Holtz, "Sensorless position control of permanent magnet synchronous machines without limitation at zero speed," in *IECON 02 [Industrial Electronics Society, IEEE 2002 28th Annual Conference of the]*, R. Kennel, Ed., vol. 1, 2002, pp. 674–679 vol.1.
- [85] J. Shen, Z. Zhu, and D. Howe, "Improved speed estimation in sensorless pm brushless ac drives," *Industry Applications, IEEE Transactions on*, vol. 38, no. 4, pp. 1072–1080, 2002.
- [86] J. Faiz and S. Mohseni-Zonoozi, "A novel technique for estimation and control of stator flux of a salient-pole pmsm in dtc method based on mtpf," *Industrial Electronics, IEEE Transactions on*, vol. 50, no. 2, pp. 262–271, 2003.

- [87] J.-H. Jang, S.-K. Sul, J.-I. Ha, M. Ohto, and K. Ide, "Analysis of permanent magnet machine for sensorless control based on high frequency signal injection," in *Industry Applications Conference, 2003. 38th IAS Annual Meeting. Conference Record of the*, vol. 1, 2003, pp. 592–598 vol.1.
- [88] J.-H. Jang, S.-K. Sul, and Y.-C. Son, "Current measurement issues in sensorless control algorithm using high frequency signal injection method," in *Industry Applications Conference, 2003. 38th IAS Annual Meeting. Conference Record of the*, vol. 2, 2003, pp. 1134–1141 vol.2.
- [89] J.-H. Jang, J.-I. Ha, M. Ohto, K. Ide, and S.-K. Sul, "Analysis of permanent-magnet machine for sensorless control based on high-frequency signal injection," *Industry Applications, IEEE Transactions on*, vol. 40, no. 6, pp. 1595–1604, 2004.
- [90] J. Shen, Z. Zhu, and D. Howe, "Sensorless flux-weakening control of permanent-magnet brushless machines using third harmonic back emf," *Industry Applications, IEEE Transactions on*, vol. 40, no. 6, pp. 1629–1636, 2004.
- [91] C. De Angelo, G. Bossio, J. Solsona, G. Garcia, and M. Valla, "A rotor position and speed observer for permanent-magnet motors with nonsinusoidal emf waveform," *Industrial Electronics, IEEE Transactions on*, vol. 52, no. 3, pp. 807–813, 2005.
- [92] Q. Jiang, C. Bi, and S. Lin, "Sensorless control of permanent magnet spindle motors used in hard disk drives," in *Electrical Machines and Systems, 2005. ICEMS 2005. Proceedings of the Eighth International Conference on*, vol. 1, 2005, pp. 177–182 Vol. 1.
- [93] Y. Zhang, J. Gu, Z. Wu, and J. Ying, "Investigation of high frequency injection method for surface-mounted pmsm sensor-less drive," in *Electrical Machines and Systems, 2005. ICEMS 2005. Proceedings of the Eighth International Conference on*, vol. 1, 2005, pp. 306–309 Vol. 1.
- [94] P. Acarnley and J. Watson, "Review of position-sensorless operation of brushless permanent-magnet machines," *Industrial Electronics, IEEE Transactions on*, vol. 53, no. 2, pp. 352–362, 2006.
- [95] G. Bisheimer, M. Sonnaillon, C. De Angelo, J. Solsona, and G. Garcia, "Permanent magnet motor control in full speed range without mechanical sensors," in *Power Electronics and Motion Control Conference, 2006. EPE-PEMC 2006. 12th International*, 2006, pp. 349–354.
- [96] C. De Angelo, G. Bossio, J. Solsona, G. Garcia, and M. Valla, "Mechanical sensorless speed control of permanent-magnet ac motors driving an unknown load," *Industrial Electronics, IEEE Transactions on*, vol. 53, no. 2, pp. 406–414, 2006.

- [97] S. Morimoto, M. Sanada, and Y. Takeda, "Mechanical sensorless drives of ipmsm with online parameter identification," *Industry Applications, IEEE Transactions on*, vol. 42, no. 5, pp. 1241–1248, 2006.
- [98] J.-K. Seok, J.-K. Lee, and D.-C. Lee, "Sensorless speed control of nonsalient permanent-magnet synchronous motor using rotor-position-tracking pi controller," *Industrial Electronics, IEEE Transactions on*, vol. 53, no. 2, pp. 399–405, 2006.
- [99] J. Shen and S. Iwasaki, "Sensorless control of ultrahigh-speed pm brushless motor using pll and third harmonic back emf," *Industrial Electronics, IEEE Transactions on*, vol. 53, no. 2, pp. 421–428, 2006.
- [100] C. Silva, G. Asher, and M. Sumner, "Hybrid rotor position observer for wide speed-range sensorless pm motor drives including zero speed," *Industrial Electronics, IEEE Transactions on*, vol. 53, no. 2, pp. 373–378, 2006.
- [101] O. Wallmark and L. Harnefors, "Sensorless control of salient pmsm drives in the transition region," *Industrial Electronics, IEEE Transactions on*, vol. 53, no. 4, pp. 1179–1187, 2006.
- [102] N. Bianchi and S. Bolognani, "Influence of rotor geometry of an ipm motor on sensorless control feasibility," *Industry Applications, IEEE Transactions on*, vol. 43, no. 1, pp. 87–96, 2007.
- [103] C.-H. Choi and J.-K. Seok, "Compensation of zero-current clamping effects in high-frequency-signal-injection-based sensorless pm motor drives," *Industry Applications, IEEE Transactions on*, vol. 43, no. 5, pp. 1258–1265, 2007.
- [104] H. Hida, Y. Tomigashi, and K. Kishimoto, "Novel sensorless control for pm synchronous motors based on maximum torque control frame," in *Power Electronics and Applications, 2007 European Conference on*, Y. Tomigashi, Ed., 2007, pp. 1–10.
- [105] T. Matzen and P. Rasmussen, "Modelling magnetic saturation effects in ipmsms for use in sensorless saliency based methods," in *Power Electronics and Applications, 2007 European Conference on*, P. Rasmussen, Ed., 2007, pp. 1–8.
- [106] S. Taniguchi, S. Wakao, K. Kondo, and T. Yoneyama, "Position sensorless control of permanent magnet synchronous motor at low speed range using harmonic voltage injection," in *Power Electronics and Applications, 2007 European Conference on*, S. Wakao, Ed., 2007, pp. 1–7.
- [107] K. Wang, J. Shen, and S. Z. Dong, "Sensorless control and initial position estimation of permanent magnet flux switching motor," in *Electrical Machines and Systems, 2007. ICEMS. International Conference on*, 2007, pp. 487–491.

- [108] S. Wu, Y. Li, and X. Miao, "Comparison of signal injection methods for sensorless control of pmsm at very low speeds," in *Power Electronics and Applications, 2007 European Conference on*, Y. Li, Ed., 2007, pp. 1–6.
- [109] N. Bianchi, S. Bolognani, J.-H. Jang, and S.-K. Sul, "Advantages of inset pm machines for zero-speed sensorless position detection," *Industry Applications, IEEE Transactions on*, vol. 44, no. 4, pp. 1190–1198, 2008.
- [110] S. Chi and J. Sun, "A novel sliding mode observer with multilevel discontinuous control for position sensorless pmsm drives," in *Applied Power Electronics Conference and Exposition, 2008. APEC 2008. Twenty-Third Annual IEEE*, J. Sun, Ed., 2008, pp. 127–131.
- [111] A. Consoli, G. Scarcella, G. Scelba, A. Testa, and S. De Caro, "Sensorless ipms motor drive control for electric power steering," in *Power Electronics Specialists Conference, 2008. PESC 2008. IEEE*, 2008, pp. 1488–1494.
- [112] S. Gottfried and R. Kennel, "Drift and parameter compensated flux estimator for pmsm with assistance of alternating carrier hf injection - encoderless control in whole speed range," in *Power Electronics and Motion Control Conference, 2008. EPE-PEMC'08. IEEE International*, 2008.
- [113] D. Raca, P. Garcia, D. Reigosa, F. Briz, and R. Lorenz, "A comparative analysis of pulsating vs. rotating vector carrier signal injection-based sensorless control," in *Applied Power Electronics Conference and Exposition, 2008. APEC 2008. Twenty-Third Annual IEEE*, P. Garcia, Ed., 2008, pp. 879–885.
- [114] P. Guglielmi, M. Pastorelli, and A. Vagati, "Cross-saturation effects in ipm motors and related impact on sensorless control," *Industry Applications, IEEE Transactions on*, vol. 42, no. 6, pp. 1516–1522, 2006.
- [115] P. Jansen and R. Lorenz, "Transducerless position and velocity estimation in induction and salient ac machines," *Industry Applications, IEEE Transactions on*, vol. 31, no. 2, pp. 240–247, 1995.
- [116] —, "Transducerless field orientation concepts employing saturation-induced saliencies in induction machines," *Industry Applications, IEEE Transactions on*, vol. 32, no. 6, pp. 1380–1393, 1996.
- [117] L. Harnefors and H.-P. Nee, "A general algorithm for speed and position estimation of ac motors," *Industrial Electronics, IEEE Transactions on*, vol. 47, no. 1, pp. 77–83, 2000.

- [118] J.-S. Yim, S.-K. Sul, H.-J. Ahn, and D.-C. Han, “Sensorless position control of active magnetic bearings based on high frequency signal injection with digital signal processing,” in *Applied Power Electronics Conference and Exposition, 2004. APEC '04. Nineteenth Annual IEEE*, vol. 2, 2004, pp. 1351–1354 vol.2.
- [119] F. De Belie, J. Melkebeek, L. Vandeveldel, R. Boel, K. Geldhof, and T. Vyncke, “A non-linear model for synchronous machines to describe high-frequency signal based position estimators,” in *Electric Machines and Drives, 2005 IEEE International Conference on*, 2005, pp. 696–703.
- [120] F. M. L. L. De Belie, F. M. L. L. De Belie, P. Sergeant, and J. A. A. Melkebeek, “Reducing steady-state current distortions in sensorless control strategies by using adaptive test pulses,” in *Applied Power Electronics Conference and Exposition, 2008. APEC 2008. Twenty-Third Annual IEEE*, P. Sergeant, Ed., 2008, pp. 121–126.
- [121] G. De Donato, G. De Donato, M. C. Harke, F. Giulii Capponi, and R. D. Lorenz, “Sinusoidal surface-mounted pm machine drive using a minimal resolution position encoder,” in *Applied Power Electronics Conference and Exposition, 2008. APEC 2008. Twenty-Third Annual IEEE*, M. C. Harke, Ed., 2008, pp. 104–110.
- [122] L. Xu, X. Xu, T. Lipo, and D. Novotny, “Vector control of a synchronous reluctance motor including saturation and iron loss,” *Industry Applications, IEEE Transactions on*, vol. 27, pp. 997–984, 1991.

# Appendix A

## Trigonometric identities

$$\sin x \sin y = \frac{1}{2} [\cos (x - y) - \cos (x + y)] \quad (\text{A.1})$$

$$\cos x \cos y = \frac{1}{2} [\cos (x - y) + \cos (x + y)] \quad (\text{A.2})$$

$$\sin x \cos y = \frac{1}{2} [\sin (x + y) + \sin (x - y)] \quad (\text{A.3})$$

$$\cos x \sin y = \frac{1}{2} [\sin (x + y) - \sin (x - y)] \quad (\text{A.4})$$

$$\sin(x + y) = \sin x \cos y + \cos x \sin y \quad (\text{A.5})$$

$$\sin(x - y) = \sin x \cos y - \cos x \sin y \quad (\text{A.6})$$

$$\cos(x + y) = \cos x \cos y - \sin x \sin y \quad (\text{A.7})$$

$$\cos(x - y) = \cos x \cos y + \sin x \sin y \quad (\text{A.8})$$


# Appendix B

## File Attachments

These programs are free software: you can redistribute it and/or modify it under the terms of the GNU General Public License as published by the Free Software Foundation, either version 3 of the License, or (at your option) any later version.

These programs are distributed in the hope that it will be useful, but WITHOUT ANY WARRANTY; without even the implied warranty of MERCHANTABILITY or FITNESS FOR A PARTICULAR PURPOSE. See the GNU General Public License for more details. You should have received a copy of the GNU General Public License along with this program. If not, see <http://www.gnu.org/licenses/>.


### B.1 RSM simulation in Matlab Simulink

1. Right click on the paper clip and then "Save Embedded File to Disk..." .
2. Choose a location to save the file **RSM\_simulation.zi**.
3. Go to that location and rename the extension of the downloaded file to zip.
4. Extract the zip file using e.g. Winzip.
5. Run Matlab. Click File, Open... and go to the location of the unzipped data.
6. Open the m-file **setup\_RSM.m**. Run the m-file (click on Run or press F5) and allow Matlab to change the directory.
7. Open the Simulink model **RSM.mdl**
8. Click on the start simulation button.
9. View any signal and change the model as you please.


## B.2 Four quadrant lookup tables generation.

- Follow steps 1 to 5 in section B.1.
- Open the m-file `generate_four_quadrant_LUTs.m` in the subfolder `Generate_LUTs`.
- Run the m-file (click on Run or press F5) and allow Matlab to change the directory.
- The m-file `create_table.m` can be used to create ANSI C code for the LUTs.

## B.3 Torque control lookup tables generation.

- Right click on the paper clip and then "Save Embedded File to Disk..." .
- Choose a location to save the file `torque_control_LUTs.zi`.
- Go to that location and rename the extension of the downloaded file to zip.
- Extract the zip file using e.g. Winzip.
- Run Matlab. Click File, Open... and go to the location of the unzipped data.
- Open the m-file `torque_control_LUTs.m`. Run the m-file (click on Run or press F5) and allow Matlab to change the directory.
- The m-file `create_table.m` can be used to create ANSI C code for the LUTs.

## B.4 RSM control and simulation code for RPS.

- Right click on the paper clip and then "Save Embedded File to Disk..." .
- Choose a location to save the file `RPS_RSM_control.zi`.
- Go to that location and rename the extension of the downloaded file to zip.
- Extract the zip file using e.g. Winzip.
- View the ANSI-files in your favourite editor.